

การนำโครงสร้างผลึกไปใช้ในแบบจำลองการเติบโตของคาร์มา-แทมโบเรนเนีย
และวูลฟ์-วิลเลนโมเลกุลาร์บีมเอพิแทกซี



นายวิฑูรย์ กาญจนภุชงค์

ศูนย์วิทยทรัพยากร
จุฬาลงกรณ์มหาวิทยาลัย

วิทยานิพนธ์นี้เป็นส่วนหนึ่งของการศึกษาตามหลักสูตรปริญญาวิทยาศาสตรมหาบัณฑิต

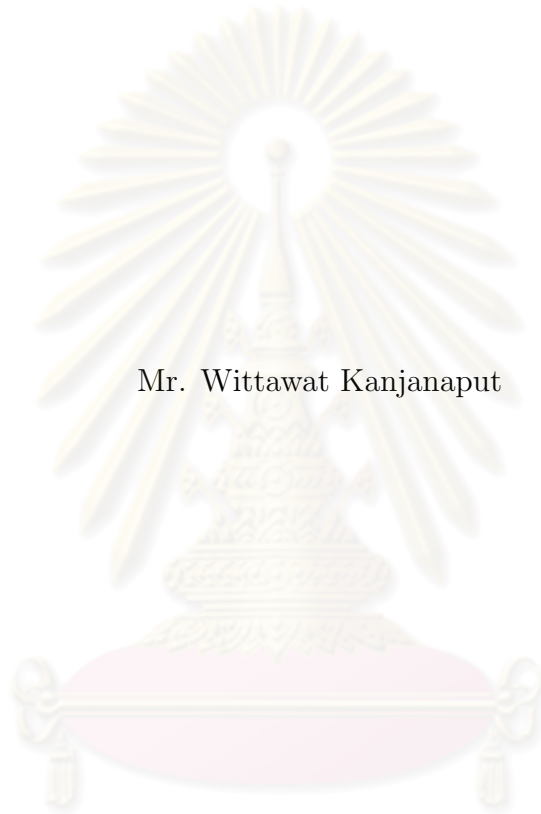
สาขาวิชาฟิสิกส์ ภาควิชาฟิสิกส์

คณะวิทยาศาสตร์ จุฬาลงกรณ์มหาวิทยาลัย

ปีการศึกษา 2552

ลิขสิทธิ์ของจุฬาลงกรณ์มหาวิทยาลัย

IMPLEMENTATION OF CRYSTAL STRUCTURE INTO THE DAS
SARMA–TAMBORENEA AND WOLF–VILLAIN MOLECULAR BEAM
EPITAXY GROWTH MODELS



Mr. Wittawat Kanjanaput

A Thesis Submitted in Partial Fulfillment of the Requirements
for the Degree of Master of Science Program in Physics

Department of Physics

Faculty of Science

Chulalongkorn University

Academic Year 2009

Copyright of Chulalongkorn University

Thesis Title IMPLEMENTATION OF CRYSTAL STRUCTURE INTO
THE DAS SARMA-TAMBORENEA AND WOLF-
VILLAIN MOLECULAR BEAM EPITAXY GROWTH
MODELS


By Mr. Wittawat Kanjanaput

Field of Study Physics

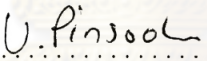
Thesis Advisor Surachate Limkumnerd, Ph.D.

Thesis Co-Advisor Assistant Professor Patcha Chatraphorn, Ph.D.


Accepted by the Faculty of Science, Chulalongkorn University in Partial Ful-
fillment of the Requirements for the Master's Degree


..... Dean of the Faculty of Science
(Professor Supot Hannongbua, Dr.rer.nat.)


THESIS COMMITTEE


..... Chairman
(Associate Professor Udomsilp Pinsook, Ph.D.)


..... Thesis Advisor
(Surachate Limkumnerd, Ph.D.)


..... Thesis Co-Advisor
(Assistant Professor Patcha Chatraphorn, Ph.D.)


..... Examiner
(Assistant Professor Tonphong Kaewkongka, Ph.D.)


..... External Examiner
(Assistant Professor Tanakorn Osochan, Ph.D.)

วิทยุส กาญจนภุชงค์ : การนำโครงสร้างผลึกไปใช้ในแบบจำลองการเติบโตดาดาสซาร์มา-แทมโบเรเนียและวูลฟ์-วิลเลนเลกุลาร์บีมเอพิแทกซี. (IMPLEMENTATION OF CRYSTAL STRUCTURE INTO THE DAS SARMA-TAMBORENEA AND WOLF-VILLAIN MOLECULAR BEAM EPITAXY GROWTH MODEL) อ.ที่ปรึกษาวิทยานิพนธ์หลัก: อ.ดร. สุรเชษฐ์ หลิมกำเนิด, อ.ที่ปรึกษาวิทยานิพนธ์ร่วม : ผศ.ดร. ปัจฉา ฉัตรภรณ์ , 86 หน้า.

เป็นที่ยอมรับกันโดยทั่วไปว่า กำแพงคัลย์แบบ Ehrlich-Schwoebel (ES) เป็นสาเหตุสำคัญของความไม่มีเสถียรภาพขณะเติบโต อันเนื่องจากการพยายามก่อตัวเป็นเนินที่มีโครงสร้างเป็นระเบียบ ซึ่งสามารถสังเกตเห็นได้บนพื้นผิวของฟิล์มบางที่ปลูกโดยวิธีโมเลกุลาร์บีมเอพิแทกซี (เอ็มบีอี) ปัจจุบันมีการเสนอกระบวนการที่ทำให้เกิดเนินขึ้นอีกหนึ่งรูปแบบ เนินจากกระบวนการดังกล่าวนี้เป็นผลจากความคดโค้งของขอบชั้นบันไดรอบ ๆ เนิน ทำให้เกิดการเคลื่อนตัวของอนุภาคเข้าสู่ขอบของชั้นบันได เราได้จำลองการปลูกฟิล์มแบบเอ็มบีอี บนโครงผลึกขนาดใหญ่ในระนาบต่าง ๆ โดยการใส่แบบจำลองที่จำกัดการเคลื่อนที่ชนิดที่ไม่มีช่องว่างภายในเนื้อฟิล์มจำนวนสองแบบจำลอง ซึ่งเสนอโดย Wolf-Villain และ Das Sarma-Tamborenea บนแผ่นรองรับใน 2+1 มิติ ในงานนี้เราเสนอผลของลักษณะโครงสร้างที่ทำให้เกิดกระแสของอนุภาคไหลขึ้นเนินอีกชนิดหนึ่ง กระแสชนิดนี้เกิดขึ้นกับบางลักษณะโครงสร้างผลึกเท่านั้น โดยกระแสลักษณะนี้ยังไม่เคยมีปรากฏในผลงานตีพิมพ์มาก่อน จากผลการจำลองที่ได้ในครั้งนี้ เราสังเกตเห็นการเกิดเนินขึ้นในบางกรณีโดยที่ไม่มีการใส่กำแพงคัลย์แบบ ES เข้าไปในแบบจำลอง และพบว่าเนินที่เกิดขึ้นกับบางโครงสร้างผลึกมีลักษณะเช่นเดียวกับที่สังเกตเห็นในหลาย ๆ การทดลองที่มีการปลูกฟิล์มแบบเอ็มบีอี สำหรับบางโครงสร้างผลึกที่ไม่มีกระแสชนิดนี้เราพบว่าลักษณะพื้นผิวไม่มีการเปลี่ยนแปลงตามขนาด และมีความขรุขระทางสถิติที่สามารถบอกได้ด้วยสมการการเติบโตแบบต่อเนื่องทั่วไป จากผลการทดลองพบว่าโครงสร้างที่เกิดเนินบนพื้นผิวจะมีค่าเอกซ์โพเนนต์ความขรุขระ (roughness exponent) มากกว่า 0.67 นอกจากนี้ เราได้ทำการศึกษาฟังก์ชันความสัมพันธ์ (correlation function) เพื่อยืนยันผลการเกิดเนินบนพื้นผิว จากผลการจำลองพบว่า ฟังก์ชันความสัมพันธ์มีการกวัดแกว่งสอดคล้องกับลักษณะและขนาดของเนินที่เกิดขึ้นบนพื้นผิวของฟิล์ม

ภาควิชา ฟิสิกส์ลายมือชื่อ นิสิต วิทยุส กาญจนภุชงค์.....
 สาขาวิชา ฟิสิกส์ลายมือชื่อ อ.ที่ปรึกษาวิทยานิพนธ์หลัก.....
 ปีการศึกษา 2552ลายมือชื่อ อ.ที่ปรึกษาวิทยานิพนธ์ร่วม.....

5072465423 : MAJOR PHYSICS

KEYWORDS : MBE / MOUND MORPHOLOGY / GROWTH INSTABILITY

WITTAWAT KANJANAPUT : IMPLEMENTATION OF CRYSTAL
STRUCTURE INTO THE DAS SARMA-TAMBORENEA AND WOLF-
VILLAIN MOLECULAR BEAM EPITAXY GROWTH MODELS.

ADVISOR : SURACHATE LIMKUMNERD, Ph.D., CO-ADVISOR :

ASSISTANT PROFESSOR PATCHA CHATRAPHORN, Ph.D., 86 pp.

The energetically driven Ehrlich-Schwoebel (ES) barrier had been generally accepted as the primary cause of the growth instability in the form of quasi-regular mound-like structures observed on the surface of thin film grown via molecular beam epitaxy (MBE) technique. Recently the second mechanism of mound formation was proposed in terms of a topologically induced flux of particles originating from the line tension of the step edges which form the contour lines around a mound. Through large-scale simulations of MBE growth on a variety of crystalline lattice planes using limited mobility, solid-on-solid models introduced by Wolf-Villain and Das Sarma-Tamborenea in 2+1 dimensions, we propose yet another type of topological uphill particle current which is unique to some lattice, and has hitherto been overlooked in the literature. Without ES barrier, our simulations produce spectacular mounds very similar, in some cases, to what have been observed in many recent MBE experiments. On a lattice where these currents cease to exist, the surface appears to be scale-invariant, statistically rough as predicted by the conventional continuum growth equation. We notice unstable mound-like morphologies for the structures with the roughness exponent greater than 0.67. The correlation functions are also studied to confirm the existence of mounds on the film surfaces. We find oscillations of the correlation function which correspond to the presence of mounds on the film surfaces.

Department : Physics Student's Signature *Wittawat Kanjanaput*
Field of Study : Physics Advisor's Signature *Surachate Limkumnerd*
Academic Year : 2009 Co-Advisor's Signature *Patcha Chatraphorn*

Acknowledgements

I am very grateful to Dr. Surachate Limkunnerd, my advisor, for his guidance on my thesis. He always took times from his work to advise and helped me solve my problems in this work. He also introduced me to many computer software. I would like to thank Assist. Prof. Dr. Patcha Chatraphorn, my thesis co-advisor, for her suggestions during this work. I also thank Assist. Prof. Dr. Sojiphong Chatraphorn for his help in using highly efficient computing facilities. His responses to many computer problems are greatly appreciated.

I would like to thank Assoc. Prof. Dr. Udomsilp Pinsook, Assist. Prof. Dr. Tonphong Kaewkongka and Assist. Prof. Dr. Tanakorn Osothchan to taking times from their busy schedules to be on my thesis committee.

I am thankful to the Development and Promotion of Science and Technology Talent Project (DPST) and Thailand Center of Excellence in Physics for supporting my funding.

I also thank all of my friends for their kind support during my study. I wish to thank all of the graduate students in SPRL research group for their useful discussions and suggestions on my work.

Finally, I wish to thank my parents and my sisters, Nakarin Toosri, Junjira Muangtim and Jirapa Naicharoen for all their encouragements and understanding during my study at Chulalongkorn University.

Contents

	Page
Abstract (Thai)	iv
Abstract (English)	v
Acknowledgements	vi
Contents	vii
List of Tables	x
List of Figures	xi
 Chapter	
I Introduction	1
1.1 Introduction	1
1.2 Overview of the thesis	2
II Theories, models and crystal structures	4
2.1 Discrete growth models for MBE	4
2.1.1 Das Sarma–Tamborenea model	5
2.1.2 Wolf–Villain model	6
2.2 Theories of surface growth	6
2.2.1 Interface width and critical exponents	6
2.2.2 Ehrlich–Schwoebel barrier	9
2.2.3 Step-edge diffusion current	10
2.2.4 Height-height correlation function	11

Chapter	Page
2.2.5 Continuum growth equation	13
2.3 Crystal structures	15
2.3.1 Simple Cubic	16
2.3.2 Body-centered cubic	17
2.3.3 Face-centered cubic (001)	17
2.3.4 Face-centered cubic (111)	18
2.3.5 Simple hexagonal	19
2.3.6 Hexagonal closed pack	20
2.3.7 Ideal hexagonal closed pack	20
2.4 Representation of crystal lattices	21
III Simulation results of surface growth	24
3.1 Critical exponents: crystal structures dependent	24
3.1.1 Results of critical exponents	25
3.1.2 Analyzing the critical exponents	26
3.2 Surface morphology and mound formation: crystal structures and diffusion rules dependent	29
3.2.1 Surface morphologies of different crystal structures	30
3.2.2 Correlation functions	33
3.2.3 Mounds and mechanism of mound formation	34
3.2.4 Terrace current and step edge current	35
IV Conclusions	41
References	45

Chapter	Page
Appendices.....	50
Appendix A: The plots of the critical exponents	51
Appendix B: The plots of surface morphologies and the correlation functions	71
Vitae.....	86



ศูนย์วิทยทรัพยากร
จุฬาลงกรณ์มหาวิทยาลัย

List of Tables

Table	Page
2.1 The critical exponents of the DT and WV models in 1+1 and 2+1 dimensions.	15
3.1 The critical exponents of the DT model for all lattice structures, sorted according to α	27
3.2 The critical exponents of the WV model for all lattice structures, sorted according to α	28
3.3 Edges of SH, SC, iHCP, FCC(111) and FCC(001) are shown where the corresponding terrace diffusion (TD) and step-edge diffusion (SED) currents are nonzero, calculated based on WV diffusion rule. Upper terraces are shown in gray. The horizontal direction, indicated by the arrow on the upper left hand corner, designates the [100] direction for SC and FCC(001), [1000] direction for SH and iHCP, and $[1\bar{1}0]$ direction for FCC(111).	39

ศูนย์วิทยทรัพยากร
จุฬาลงกรณ์มหาวิทยาลัย

List of Figures

Figure	Page
2.1 One dimensional Das Sarma–Tamborenea model.	5
2.2 One dimensional Wolf–Villain model.	6
2.3 Interface width as a function of time for three different system sizes.	8
2.4 The data collapse of data points in Figure 2.3	8
2.5 Side view of the Ehrlich–Schwoebel (ES) barrier. Gray circles are the substrate. Red circle is an adatom. Dash line is a potential energy plot of the red atom as a function of lattice positions on the substrate.	10
2.6 The schematic of the step-edge diffusion (SED) current of simple cubic lattice under WV diffusion rule.	11
2.7 The simple cubic crystal structure.	16
2.8 The body-centered cubic crystal structure.	17
2.9 The face-centered cubic crystal structure on the (001) plane.	18
2.10 The face-centered cubic crystal structure on the (111) plane.	18
2.11 The simple hexagonal crystal structure.	19
2.12 The hexagonal closed pack crystal structure.	20
2.13 The ideal hexagonal closed pack crystal structure.	21
2.14 Square lattice chain.	22
2.15 Triangular lattice chain.	23

3.1	Three growth regions: $1 \text{ UL} \leq t_1 \leq t_{\text{sat}}/3$, $t_{\text{sat}}/3 \leq t_2 \leq 2t_{\text{sat}}/3$, $2t_{\text{sat}}/3 \leq t_3 \leq t_{\text{sat}}$, for SC lattice, DT model.	26
3.2	The second derivative of interface width as a function of time for SC lattice, DT model.	27
3.3	The interface width as a function of time of DT model for chains with 250,000 elements.	32
3.4	The interface width as a function of time of WV model for chains with 250,000 elements.	32
3.5	Local probabilistic currents near a step edge along $[1000]$ direction of SH(0001) with a step dent. Shaded circles represent atoms on the lower terrace while light circles depict those on the upper terrace. An atom dropping on any lattice site will move, according to WV rule, to one of sites along the corresponding arrow. An atom will not move if it falls on a site without an arrow. An atom falling on site A, in particular, will be driven towards a kink site B producing a small SED current. This current is however cancelled by another downhill current from C to A. Global net currents are denoted by thick arrows.	36
3.6	Local probabilistic currents near a step edge along $[1200]$ direction of SH(0001). The upper terrace is on the left side while the lower terrace on the right. There is a net uphill terrace current acting along the $[\bar{1}000]$ direction. Noncancelling currents are indicated by thick arrows.	37
3.7	A step edge along the $[100]$ direction separates the lower region (on the bottom of the figure) and the upper region (on the top). Three atomic layers are present with a lighter shade signifies a higher layer. Occupied lattice sites are represented by full circles while dashed circles denote unoccupied ones. Locally atoms tend to move away from the terrace edge.	40

A.1	The interface width as a function of time of SC structure of DT model.	51
A.2	The interface width as a function of time of BCC structure of DT model.	52
A.3	The interface width as a function of time of FCC(001) structure of DT model.	52
A.4	The interface width as a function of time of FCC(111) structure of DT model.	53
A.5	The interface width as a function of time of SH structure of DT model.	53
A.6	The interface width as a function of time of HCP structure of DT model.	54
A.7	The interface width as a function of time of iHCP structure of DT model.	54
A.8	The scaling collapse of the SC structure of DT model.	55
A.9	The scaling collapse of the BCC structure of DT model.	55
A.10	The scaling collapse of the FCC(001) structure of DT model.	56
A.11	The scaling collapse of the FCC(111) structure of DT model.	56
A.12	The scaling collapse of the SH structure of DT model.	57
A.13	The scaling collapse of the HCP structure of DT model.	57
A.14	The scaling collapse of the iHCP structure of DT model.	58
A.15	The interface width as a function of time of SC structure of WV model.	58
A.16	The interface width as a function of time of BCC structure of WV model.	59

A.17 The interface width as a function of time of FCC(001) structure of WV model.	59
A.18 The interface width as a function of time of FCC(111) structure of WV model.	60
A.19 The interface width as a function of time of SH structure of WV model.	60
A.20 The interface width as a function of time of HCP structure of WV model.	61
A.21 The interface width as a function of time of iHCP structure of WV model.	61
A.22 The scaling collapse of the SC structure of WV model.	62
A.23 The scaling collapse of the BCC structure of WV model.	62
A.24 The scaling collapse of the FCC(001) structure of WV model.	63
A.25 The scaling collapse of the FCC(111) structure of WV model.	63
A.26 The scaling collapse of the SH structure of WV model.	64
A.27 The scaling collapse of the HCP structure of WV model.	64
A.28 The scaling collapse of the iHCP structure of WV model.	65
A.29 The roughness and dynamical exponents α and z of SC structure of DT model.	66
A.30 The roughness and dynamical exponents α and z of BCC structure of DT model.	66
A.31 The roughness and dynamical exponents α and z of FCC structure of DT model.	66
A.32 The roughness and dynamical exponents α and z of FCC(111) structure of DT model.	67

A.33 The roughness and dynamical exponents α and z of SH structure of DT model.	67
A.34 The roughness and dynamical exponents α and z of HCP structure of DT model.	67
A.35 The roughness and dynamical exponents α and z of iHCP structure of DT model.	68
A.36 The roughness and dynamical exponents α and z of SC structure of WV model.	68
A.37 The roughness and dynamical exponents α and z of BCC structure of WV model.	68
A.38 The roughness and dynamical exponents α and z of FCC structure of WV model.	69
A.39 The roughness and dynamical exponents α and z of FCC(111) structure of WV model.	69
A.40 The roughness and dynamical exponents α and z of SH structure of WV model.	69
A.41 The roughness and dynamical exponents α and z of HCP structure of WV model.	70
A.42 The roughness and dynamical exponents α and z of iHCP structure of WV model.	70
B.1 Surface morphology of the SC structure of WV model at $t = 10^5$ UL.	71
B.2 Surface morphology of the BCC structure of WV model at $t = 10^5$ UL.	72
B.3 Surface morphology of the FCC(001) structure of WV model at $t = 10^5$ UL.	72
B.4 Surface morphology of the FCC(111) structure of WV model at $t = 10^5$ UL.	73

B.5	Surface morphology of the SH structure of WV model at $t = 10^5$ UL.	73
B.6	Surface morphology of the HCP structure of WV model at $t = 10^5$ UL.	74
B.7	Surface morphology of the iHCP structure of WV model at $t = 10^5$ UL.	74
B.8	Surface morphology of the SC structure of DT model at $t = 10^5$ UL.	75
B.9	Surface morphology of the BCC structure of DT model at $t = 10^5$ UL.	75
B.10	Surface morphology of the FCC(001) structure of DT model at $t = 10^5$ UL.	76
B.11	Surface morphology of the FCC(111) structure of DT model at $t = 10^5$ UL.	76
B.12	Surface morphology of the SH structure of DT model at $t = 10^5$ UL.	77
B.13	Surface morphology of the HCP structure of DT model at $t = 10^5$ UL.	77
B.14	Surface morphology of the iHCP structure of DT model at $t = 10^5$ UL.	78
B.15	The correlation function of the SC structure of WV model at $t = 10^5$ UL.	79
B.16	The correlation function of the BCC structure of WV model at $t = 10^5$ UL.	79
B.17	The correlation function of the FCC(001) structure of WV model at $t = 10^5$ UL.	80
B.18	The correlation function of the FCC(111) structure of WV model at $t = 10^5$ UL.	80
B.19	The correlation function of the SH structure of WV model at $t = 10^5$ UL.	81
B.20	The correlation function of the HCP structure of WV model at $t = 10^5$ UL.	81

B.21 The correlation function of the iHCP structure of WV model at $t = 10^5$ UL.	82
B.22 The correlation function of the SC structure of DT model at $t =$ 10^5 UL.	82
B.23 The correlation function of the BCC structure of DT model at $t =$ 10^5 UL.	83
B.24 The correlation function of the FCC(001) structure of DT model at $t = 10^5$ UL.	83
B.25 The correlation function of the FCC(111) structure of DT model at $t = 10^5$ UL.	84
B.26 The correlation function of the SH structure of DT model at $t =$ 10^5 UL.	84
B.27 The correlation function of the HCP structure of DT model at $t =$ 10^5 UL.	85
B.28 The correlation function of the iHCP structure of DT model at $t = 10^5$ UL.	85

CHAPTER I

Introduction

1.1 Introduction

The growth of crystalline thin films via molecular beam epitaxy (MBE) has attracted several interests experimentally [1, 2] due to ever growing applications in many fields, and theoretically [3, 4, 5] due to its rich surface structures. Incoming flux of atoms deposit onto a substrate in the layer-by-layer fashion generally making the film completely free of defects. Excess energy of the adatoms allows them to diffuse along the surface away from their initial landing positions. These atoms tend to minimize their energy by moving towards sites with high coordination number such as those along island step edges. The process produces an instability in the growth morphology leading to the formation of surface structures.

Over the past decades, there have been numerous experimental evidences of a pyramid-like mound morphology with a well-defined mound shape, and a selective slope [6, 7, 8, 9, 10, 11, 12]. The origin of such a structure has mainly been attributed to the presence of Ehrlich–Schwoebel (ES) barrier [13, 14, 15, 16, 17, 18] which, according to Burton–Cabrera–Frank theory [19, 20], hinders atoms from moving down a terrace resulting in the tendency for them to prefer to flow “uphill.” Several investigators have confirmed mound formation due to ES barrier through their computer simulations [21, 22, 23, 24]. More recently another type of destabilizing ES step-edge current was discovered which causes atoms to flow along a step edge within the same terrace toward a kink site or over a corner site [25, 26]. The kink ES current, unlike the former kind, can only occur on a surface with

spatial dimension higher than one. Until the past decade, it was believed that ES barrier was the sole cause of mound morphology. Chatrathorn *et al.* [27] were able to obtain a mound-like structure without implementing the ES barrier. Unlike the ES mechanism which are energy-assisted, this mounding instability is probabilistic and topological in nature. A net current arises via the unbalanced between atoms diffusing up and down a step edge, hence the name “step-edge diffusion” (SED) current. On a simple cubic lattice, this type of current only occurs around a corner or a kink site which is similar to the kink ES current. The mounding instability through SED current did not emerge spontaneously, and was observed only after the use of the so-called “noise reduction technique” to suppress the deposition and nucleation noise. It is unclear that SED mechanism, initially studied in a simple cubic system, always occurs, and always leads to mounding structure in *all* crystalline lattice structures. Do other topological currents exist in other structurally different crystalline lattices? In this thesis we propose, in addition to ES barrier, a competing mechanism for mound formation as a consequence of probabilistic terrace currents due to the geometry of a film’s crystalline structure.

1.2 Overview of the thesis

We begin, in Chapter 2, by describing the discrete growth models for MBE and theoretical background of surface growth. The Ehrlich–Schwoebel barrier and step-edge diffusion current which are accepted as causes of mound formation on the surface are also explained in Chapter 2. In addition, several crystal structures which are used in our simulation will be shown. We also present the helical boundary conditions essential for constructing representations of various crystal structures. Growth simulations are then performed on each of these structures according to a set of diffusion rules. In Chapter 3, we begin with simulation results of critical exponents of each crystal structure obeying two diffusion rules. The roughness exponent, in particular, implies the existence of mound morphology on a particular crystalline thin film. The second part of Chapter 3 is the results

of surface morphologies. Some of them have mounds on the surface which is confirmed by the height-height correlation function of the film surface. We work out the probabilistic currents of a few crystal structures for an illustrative purpose. These currents are additional causes of mound formation on the film surfaces in our simulation results. Here, we identify a new type of uphill topological current. We discuss, at the end of Chapter 3, the mound formation mechanism in connection with an underlying continuum growth equation, and the summary of our work in Chapter 4.



ศูนย์วิจัยทรัพยากร
จุฬาลงกรณ์มหาวิทยาลัย

CHAPTER II

Theories, models and crystal structures

Molecular beam epitaxy (MBE) is one of the best known methods to fabricate high quality thin films. MBE experiments are, generally, operated in high vacuum or ultra-high vacuum (10^{-10} torr) to reduce unwanted particles in the chamber. The advantage of this technique is the slow deposition rate which allows the film to grow epitaxially (layer-by-layer). In the molecular beam epitaxial growth mechanism, there are three main microscopic processes which are *deposition process*, *surface diffusion process* and *desorption process* [3]. During the first stage of growth an atom from the vapor (beam) deposits on to a substrate, then moves to form bonds with the crystal on a substrate, and sticks. The desorption process, generally, occurs at high temperature when a deposited atom breaks the bonds and leaves the surface. If the substrate temperature is not too high, the desorption rate is very low compared to the deposition rate. We assume that, in our studies, that the desorption process is negligible. After an atom deposits onto surface and adheres to the substrate, it can break the bonds and diffuses on the surface to find an *energetically most favorable position* [3]. This process is named surface diffusion. The length of the diffusion depends on the bonding energy and the temperature of the atom.

2.1 Discrete growth models for MBE

In this section, we will explain surface growth models that are used in our simulations. All model are solid-on-solid which no overhang and void defect in

the film. Despite decades of intense investigations both computationally and analytically, Monte–Carlo simulations of thin-film MBE growth have been limited to various “toy” models; boxes representing atoms are sprinkled down from atop and subsequently relax to their final atomic positions without any voids or overhangs according to a given set of rules. We examine the limit of low substrate temperatures so that deposition atoms can move at most to one of the nearest neighboring sites before coming to rest. We use Das Sarma–Tamborenea (DT) model and Wolf–Villain (WV) model, which are most prominent diffusion rules, in our simulations.

2.1.1 Das Sarma–Tamborenea model

In 1991 Das Sarma and Tamborenea proposed a simple surface growth model named after them [28, 29]. During a growth process, an atom is dropped randomly on an initially flat substrate. The adatom can diffuse immediately to one of its nearest neighbor positions with equal probability to *increase* its coordination number provided that the current number of bond is less than two. Some other conditions the atom does not move. Figure 2.1 gives a schematic diagram of the DT diffusion rules in a simplified 1 + 1 dimensions. An atom falls on one of the shaded regions can diffuse immediately to one of the direction specified by arrow(s) with equal probability.

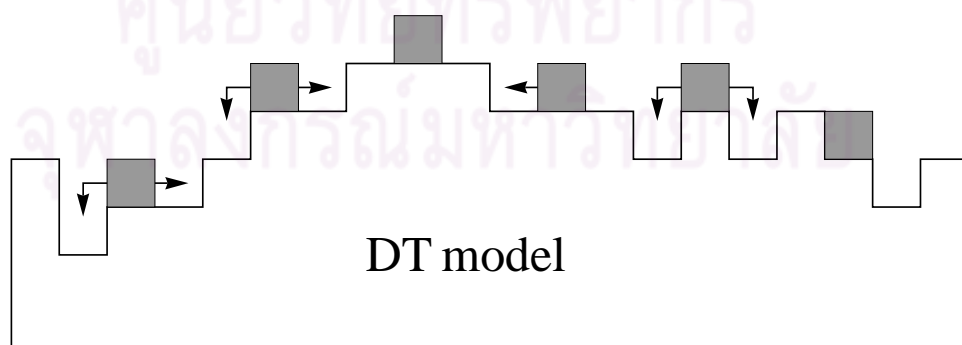


Figure 2.1: One dimensional Das Sarma–Tamborenea model.

2.1.2 Wolf–Villain model

Wolf–Villain model is another surface growth model that we apply to our simulations. This model was proposed by D. E. Wolf and J. Villain [30] in 1990. In this model, an atom is deposited on an substrate. After that, the atom can move to *maximize* its nearest neighbor bonds. Figure 2.2 gives a schematic diagram of the WV diffusion rules in a simplified 1 + 1 dimensions. An atom drops on one of the gray regions and immediately moves to one of the direction specified by arrow(s) with equal probability.

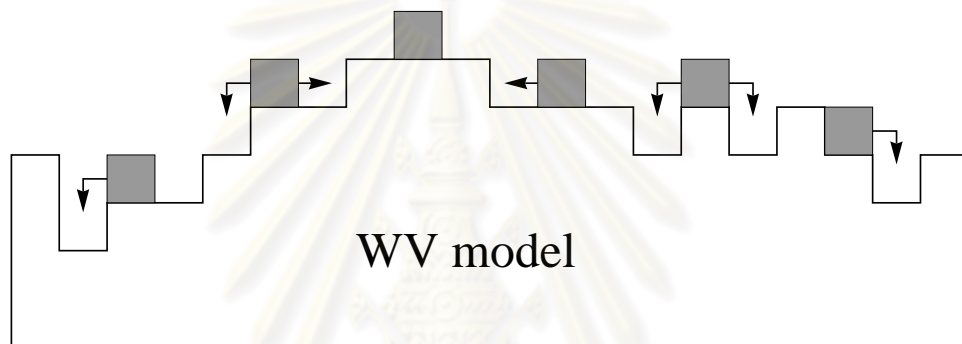


Figure 2.2: One dimensional Wolf–Villain model.

2.2 Theories of surface growth

Generally the aim of our simulations is to understand the kinetic phenomena of surface growth. There are simple methods that are used to analyze and describe the growth mechanism. In this section, we will introduce some of them here.

2.2.1 Interface width and critical exponents

A common quantity that is used to characterize the roughness of the film surface is the interface width. The interface width, the root mean square of the

height fluctuation of the film surface, is defined by

$$W(L, t) \equiv \left[\frac{1}{L^d} \sum_i h(\vec{x}, t) - \langle h(t) \rangle^2 \right]^{1/2}, \quad (2.1)$$

where $h(\vec{x}, t)$ is the atomic height at lattice position \vec{x} and time t , and $\langle h(t) \rangle$ is the average height of all lattice positions on the substrate of dimension d and lateral size L . At an early stage of the growth, the interface width in formal growth models increases with time as a power law

$$W(L, t) \sim t^\beta. \quad (2.2)$$

Here β is *the growth exponent* which represents the evolution of the film surface roughness with time in an early stage. The interface width grows until it reaches a *saturation value* W_{sat} . After this point the interface width does not continually increase with time, but stays at the same value (W_{sat}) forever. The time at which the interface width begins to saturate is called *the saturation time* t_{sat} [3]. The saturation value of the interface width varies with substrate size as a power law,

$$W_{\text{sat}}(L) \sim L^\alpha, \quad (2.3)$$

where α is *the roughness exponent* which indicates the roughness of the saturated interface. From Equations 2.2 and 2.3, the interface width can be written as

$$W(L, t) \sim \begin{cases} t^\beta, & t \ll t_{\text{sat}}, \\ L^\alpha, & t \gg t_{\text{sat}}. \end{cases} \quad (2.4)$$

The saturation time also scales with substrate size with a power law relation

$$t_{\text{sat}} \sim L^z, \quad (2.5)$$

with *the dynamical exponent* z , which gives the information about the dependence of the saturated time and the substrate size. A typical interface width as a function of time is plotted in Figure 2.3. The different curves correspond to different system sizes (L_3 is the largest and L_1 is the smallest).

From Equations (2.2), (2.3), (2.5) imply that $z = \alpha/\beta$, as suggested by the dynamic scaling theory. If we divide the interface width by the saturation width,

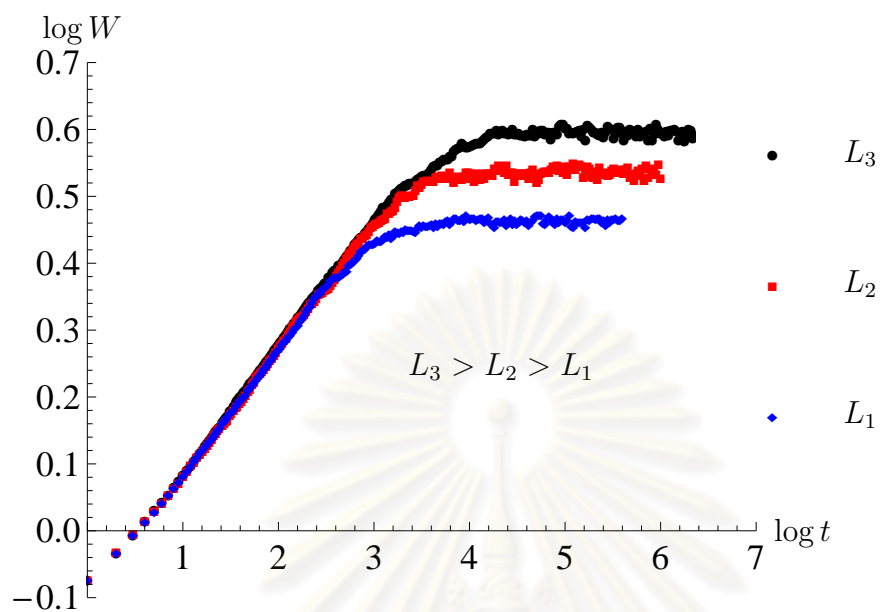


Figure 2.3: Interface width as a function of time for three different system sizes.

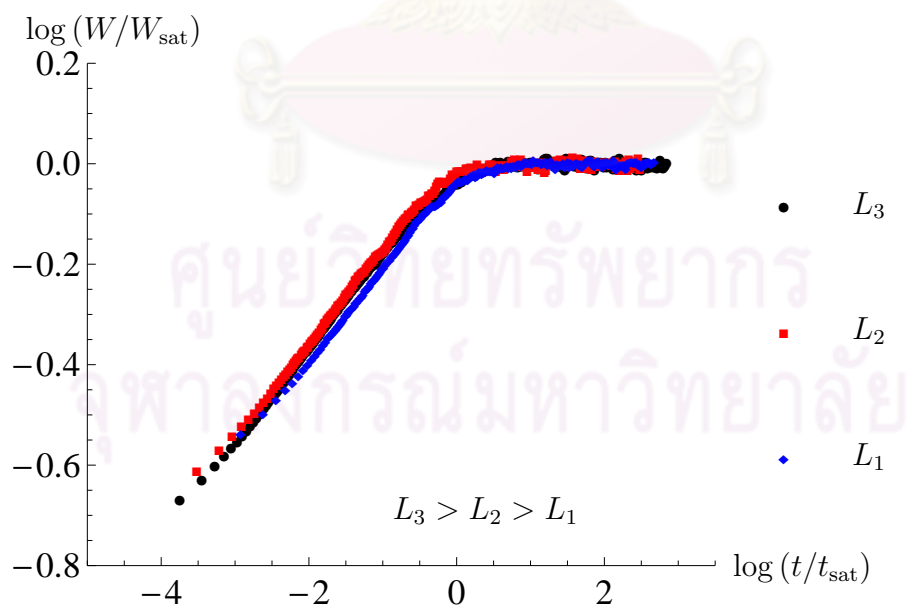


Figure 2.4: The data collapse of data points in Figure 2.3

the interface width will saturate at the same value. Dividing growth time by saturation time will cause the interface width saturate at the same characteristic time. This is a simple method to collapse the data onto a single curve [3]. The data of Figure 2.3 after collapse are shown in Figure 2.4.

In 1+1 dimensions (one spatial dimension + one time), The α, β and z exponents directly associate a given discrete growth model to a universality class. Despite impressive success in 1+1 dimensions, the computational results of several toy models do not conform to the theoretical predictions in 2+1 dimensions. The presence of mound morphology, a missing feature in one spatial dimension, suggests that a given model may belong to a different universality class in a different dimension, thus rendering the universality class concept futile [31, 32, 33].

2.2.2 Ehrlich–Schwoebel barrier

Ehrlich–Schwoebel (ES) barrier [13, 14] is an energetic barrier. The ES barrier prevents an adatom from diffusing over a step edge from the upper to the lower terrace. In figure 2.5, an atom (red circle) is deposited on the substrate (gray circles). At this position the atom can bond with its nearest neighbor atoms (atom A and B). The red atom tries to diffuse to the right side according to the arrow which is more stable than the original position because the atom can bond with three nearest neighbor atoms (atom B, C and D). While the red atom diffuses from the original position to the new position, the atom must pass through an unstable position because the atom has to use its energy to break bond with atom A to diffuse to the right side and has only one bond with atom B. Every atom which can diffuse from the upper terrace to the lower terrace must have enough energy to pass through this energy barrier. An atom which does not have enough energy cannot diffuse to the lower terrace. The deposited atoms are preferential to diffuse in the uphill direction.

This mechanism has been confirmed by Ehrlich and Hudde [13] in 1966. They use field-ion microscopy to observe a motion of a single atom on an atomic

terrace. They found that the atom favors the diffusion back at the edge of the terrace. This mechanism is also proposed by Shcwoebel and Shipsey [14] at the same time.

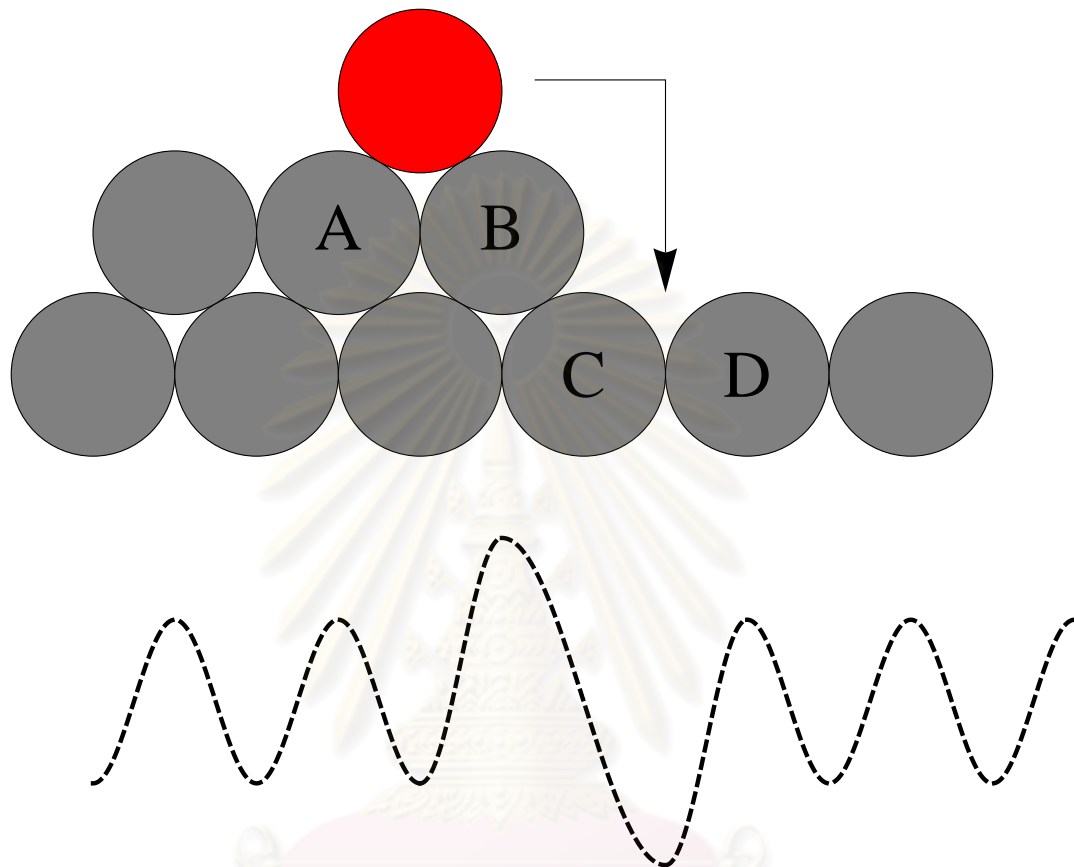


Figure 2.5: Side view of the Ehrlich–Schwoebel (ES) barrier. Gray circles are the substrate. Red circle is an adatom. Dash line is a potential energy plot of the red atom as a function of lattice positions on the substrate.

2.2.3 Step-edge diffusion current

Step-edge diffusion (SED) current is another cause of mound formation on the film surface. The SED is not an energetic potential barrier the same way ES barrier is. The SED current occurs because of the diffusion rule and lattice structure of the material. On a simple cubic lattice, this type of current only occurs around a corner or a kink site, that is, local particle currents are proportional to

the local curvature of the step edge. Figure 2.6 gives a schematic diagram of SED current of simple cubic lattice under WV diffusion rule. The SED current occurs from an atom which is deposited near the edge and flows along the edge to kink site within the same terrace as shown by the white box in figure 2.6. The atom tends to enlarge the upper terrace, hence, gives rise to a mound.

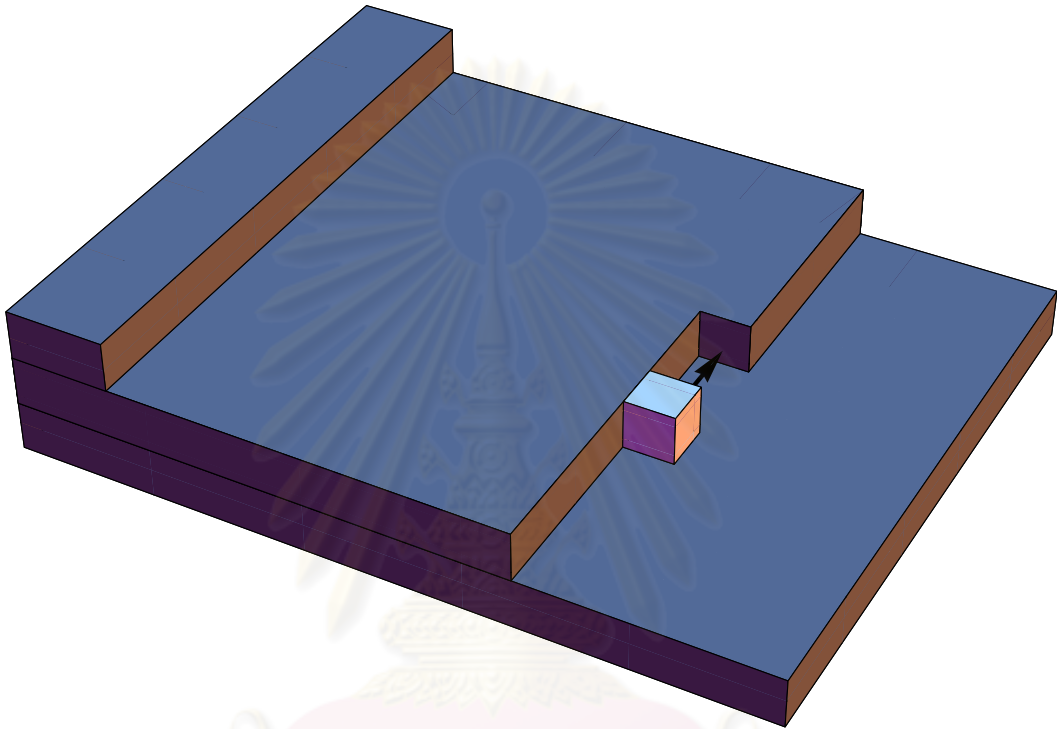


Figure 2.6: The schematic of the step-edge diffusion (SED) current of simple cubic lattice under WV diffusion rule.

2.2.4 Height-height correlation function

A formal method to characterize mounded morphologies of the film surface is the height-height correlation function. We use it to prove the existence of mounds on the surface. The height-height correlation function is defined as

$$C(\vec{r}) = \langle h(\vec{x})h(\vec{x} + \vec{r}) \rangle_{\vec{x}}, \quad (2.6)$$

where $h(\vec{x})$ is the surface height at a lattice position \vec{x} measured with respect to the average height and \vec{r} is the difference between the position vectors of two sites

on the substrate. Here $\langle \dots \rangle_{\vec{x}}$ denotes the average over lattice positions \vec{x} on the substrate. The correlation function in this work is evaluated in two dimensions.

This function, by definition, expresses a relation between two points on the surface. Note that the height, the deviation away from the surface height average, at any positions can be positive, negative or zero. The correlation function has the maximum value at $\vec{r} = 0$ because the product of the same position results in $(h(\vec{x}))^2$ which is always positive. But for another \vec{r} , ($\vec{r} \neq 0$), the product of two heights on the substrate can be positive, negative or zero. The average mound height, in other words, the root-mean-square of the surface height is defined by

$$H = \sqrt{C(\vec{r} = 0)}, \quad (2.7)$$

which is the square root of the correlation function with $\vec{r} = 0$. The correlation at the neighboring positions of $\vec{r} = 0$ is calculated from the average product of every two adjacent sites on the surface. Some of them may be positive negative or zero resulting in the decrease of $C(\vec{r})$. This function continuously decreases with \vec{r} to a minimum value. Let us concentrate on the condition at which $C(\vec{r}) = 0$. The average value of zero in this situation can be separated into two cases. First, the average zero value results from the average of the products of two heights, one of which has zero value. The second is the product of two random heights which can be positive, negative or zero but the average turns out to be zero. The products between two uncorrelated positions on the substrate are, in general, random which results in a zero average. So the average mound radius is $|\vec{r}|$ at the first zero crossing of $C(\vec{r})$. When the magnitude of \vec{r} exceeds the average mound radius, the function begins to be negative. The two positions ($h(\vec{x})$ and $h(\vec{x} + \vec{r})$) in this situation are, on average, negatively correlated. The correlation function gives the minimum value when $|\vec{r}|$ is roughly the distance from a mound center to a trough.

If the surface contains regularly mounded patterns, the correlation goes up again for $|\vec{r}|$ greater than the average mound size. The correlation function in this case will oscillate with a period of about twice the mound radius. This is

because, in this case, mounds on the surface repeat every twice the mound radius. We will observe the oscillation of $C(\vec{r})$ as a function of \vec{r} . In contrast to mounded morphologies, if $C(\vec{r})$ continuously decreases with \vec{r} to zero, this signifies that the film surface is kinetically rough without mound morphology.

2.2.5 Continuum growth equation

The generic non-equilibrium surface growth where voids and defects are prevalent has been generally accepted as belonging to the Kardar–Parisi–Zhang (KPZ) universality class [34], originated in the study of Eden cluster growth [35] and diffusion-limited aggregation [36, 37], with the dominant growth direction pointing along the surface normal, giving rise to a term proportional to $\sim (\vec{\nabla}h)^2$.

The study of kinetic surface roughening of non-equilibrium growth models of the solid-on-solid type remains a subject under much scrutiny [3, 4]. The continuum growth equation can be constructed by using symmetry principles. The general form of the growth equation [3] for conserved growth model is

$$\frac{\partial h(\vec{x}, t)}{\partial t} = G(h, \vec{x}, t) + \eta(\vec{x}, t), \quad (2.8)$$

where $G(h, \vec{x}, t)$ is a general function which depends on the surface height $h(\vec{x}, t)$, position \vec{x} and time t . $\eta(\vec{x}, t)$ is the Gaussian noise where $\langle \eta(\vec{x}, t) \rangle = 0$, and

$$\langle \eta(\vec{x}, t) \eta(\vec{x}', t') \rangle = 2D \delta(\vec{x} - \vec{x}') \delta(t - t').$$

Based on symmetry principles, it can be shown that the growth equation, up to the fourth order, has the form

$$\frac{\partial h}{\partial t} = \nu_2 \nabla^2 h - \nu_4 \nabla^4 h + \lambda_{13} \vec{\nabla} \cdot (\vec{\nabla} h)^3 + \lambda_{22} \nabla^2 (\vec{\nabla} h)^2 + \eta. \quad (2.9)$$

We want to know the scaling properties in the *asymptotic limits*, i.e., at large time ($t \rightarrow \infty$) and large distance ($x \rightarrow \infty$). In these limits the higher order terms are less important compared to the lower order terms. The most relevant term in

Equation 2.9 is $\nabla^2 h$, the Edward–Wilkinson (EW) term [38], which leads to the EW universality class with continuum growth equation:

$$\frac{\partial h}{\partial t} = \nu_2 \nabla^2 h + \eta. \quad (2.10)$$

In 1 + 1 dimensions of WV and EW model, where adatom moves to the nearest neighbor with the minimal local height, both belong to EW universality class with $\alpha = 1/2, \beta = 1/4, z = 2$. The WV model in 2 + 1 dimensions is predicted to produce logarithmically smooth surface with $\alpha = \beta = 0$ (log), while the dynamical exponent still obeys power law scaling with $z = 2$.

Solid-on-solid growth models, replicating MBE growth, offer much richer behaviors especially when the spatial dimension is higher than one. It has been known that a slight change in a diffusion rule results in an alteration of the universality class. In 1+1 dimensions, DT model belongs to MBE class with $\alpha = 1, \beta = 1/3, z = 3$ [32] despite closer morphological rule to WV than is EW model [3]. The coefficient $\nu_2 = 0$ for DT model by symmetry, and the term proportional to $\vec{\nabla} \cdot (\vec{\nabla} h)^3$ is often neglected (by setting λ_{13} to zero) because it generates the $\nu_2 \nabla^2 h$ term upon renormalization. Physically speaking this term (with $\lambda_{13} > 0$) gives a dissipative effect similar to the $\nu_2 \nabla^2 h$ term, but at a shorter length scale.

Provided the validity of Equation (2.9) with the coefficients having the same sign as in 1+1 dimensions, the DT exponents in 2+1 dimensions are found to be $\alpha = 2/3, \beta = 1/5, \text{ and } z = 10/3$ [3]. A large-scale simulation on a SC substrate by Das Sarma *et al.*, however, gives a contradictory result [32]. They reported that the DT model behaved as if it were in the EW universality class which suggests that ν_2 in Equation (2.9) is no longer zero in this dimension. They also observed mound formation in the WV simulations, instead of logarithmically flat surface, with $\alpha = 1, \beta = 1/4, \text{ and } z = 4$ after making use of the noise reduction technique. This implies that WV model is *not* in the EW universality class in 2+1 dimensions. Moreover, the mounds tend to be of roughly equal size—an apparent deviation from being scale invariant.

Recently Haselwandter *et al.* [39, 40] have shown that the unstable growth

Table 2.1: The critical exponents of the DT and WV models in 1+1 and 2+1 dimensions.

Model	Equation	$d = 1 + 1$	$d = 2 + 1$
DT	$\frac{\partial h}{\partial t} = -\nu_4 \nabla^4 h + \lambda_{22} \nabla^2 (\vec{\nabla} h)^2 + \eta$	$\alpha = 1$	$\alpha = 2/3$
		$\beta = 1/3$	$\beta = 1/5$
		$z = 3$	$z = 10/3$
WV	$\frac{\partial h}{\partial t} = \nu_2 \nabla^2 h + \eta$	$\alpha = 1/2$	$\alpha = 1$
		$\beta = 1/4$	$\beta = 1/3$
		$z = 2$	$z = 4$

observed in WV model could be explained using renormalization group approach. They derived Equation (2.9) from a master equation describing the increment of height at each lattice site according to the nearest-neighbor sites. By carefully choosing the regularization parameter upon taking a continuum limit, they were able to obtain the values of the coefficients ν_2 , ν_4 , λ_{13} and λ_{22} . Under repeated RG transformations, these values flow differently in $d = 1 + 1$ and $2 + 1$ dimensions. In particular the negativity of λ_{13} leads to the change in the sign of the diffusion coefficient ν_2 which eventually leads to the growth instability in the form of an array of islands of lateral size $\sim 2\pi\sqrt{2|\nu_4/\nu_2|}$. While their analysis gives a satisfactory account of the origin of mounds, their formulation is still appealed to an atypical regularization procedure with some dimensional dependency, and is not so conveniently extensible to analyze a more complicated lattice. In particular it is unclear whether the mechanism that gives rise to the growth instability is the property of the substrate dimension or of lattice geometry.

2.3 Crystal structures

In many prior computer simulations of thin films, deposited atoms are modeled as a falling blocks. The crystal structures are limited to simple cubic lattice.

In this work we simulate the growth of 6 crystal structures on 7 planes: simple cubic, body-centered cubic, face-centered cubic on (001) and (111) planes, simple hexagonal, hexagonal closed pack, and ideal hexagonal closed pack. The structures whose substrate plane is not listed are understood to be on the (001) plane. The detail of each crystal structure and plane will be presented in this section.

2.3.1 Simple Cubic

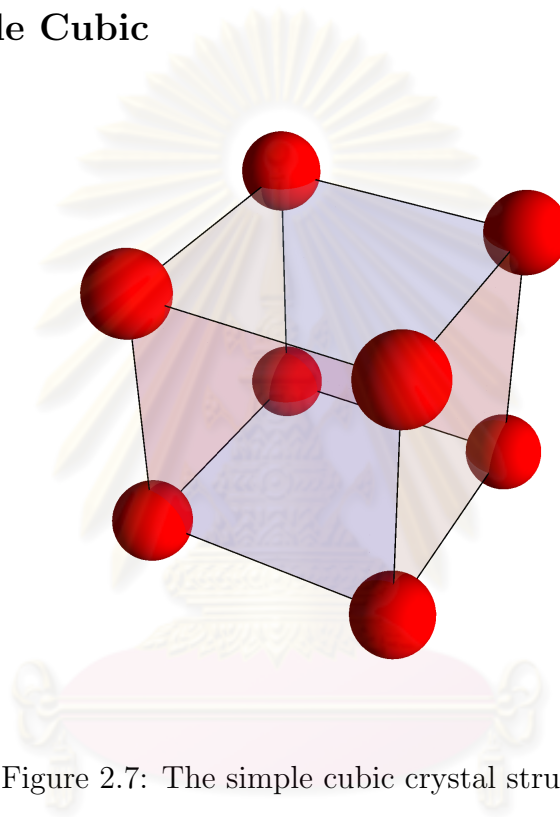


Figure 2.7: The simple cubic crystal structure.

Thin film growth using simple cubic (SC) crystal structure, the simplest structure, has been generally simulated to investigate the mechanism of a growth process. This structure has only one atom and one layer per unit cell as is shown in Figure 2.7. Each atom has the maximum number nearest neighbors of up to six atoms with one atom at the lower and the upper layers and four atoms at the same layer. This structure has fourfold rotational symmetry which means that rotation by an angle of $\pi/2$ with respect to a particular atom does not change the lattice. Most simulation results of molecular beam epitaxy are performed with the simple cubic structure so we can confirm the correction of our algorithms by comparing the simulation results of ours using this crystal structure.

2.3.2 Body-centered cubic

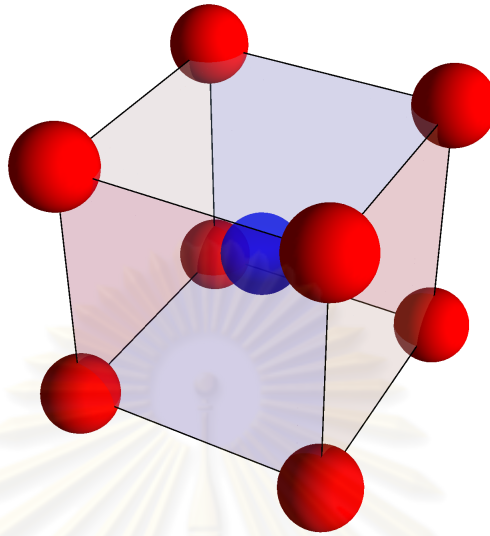


Figure 2.8: The body-centered cubic crystal structure.

Body-centered cubic (BCC) crystal structure, which is shown in Figure 2.8, has two atoms and two layers per unit cell, i.e., the coordinates of the atoms in the vertical direction repeat themselves every two layers. Each atom can bond with four nearest neighbors at the lower layer and the upper layer. Many materials such as Mo, Na, W, Ta are body-centered cubic. This structure has fourfold rotational symmetry.

2.3.3 Face-centered cubic (001)

Face-centered cubic crystal (FCC(001)) structure has four atoms per unit cell with two different layers. Figure 2.9 represents the FCC(001) structure, the red atoms and the blue atoms locate at each corners and faces of the cube respectively. Each atom has the maximum nearest neighbors of up to twelve atoms with four atoms at the lower, the upper and the same layers. The face-centered cubic structure has fourfold rotational symmetry. The structure of many materials such as Cu, Ag, Pt, Au, Rh are face-centered cubic.

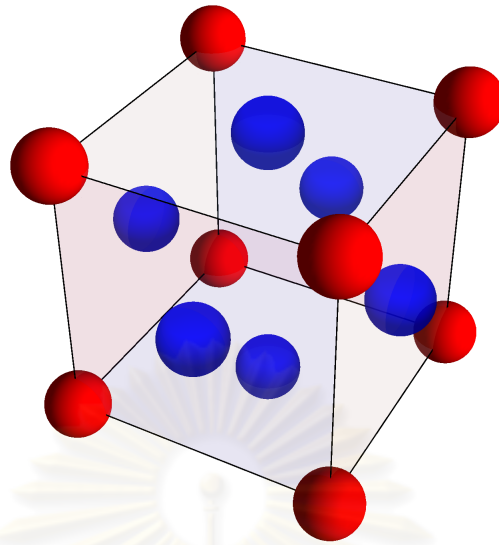


Figure 2.9: The face-centered cubic crystal structure on the (001) plane.

2.3.4 Face-centered cubic (111)

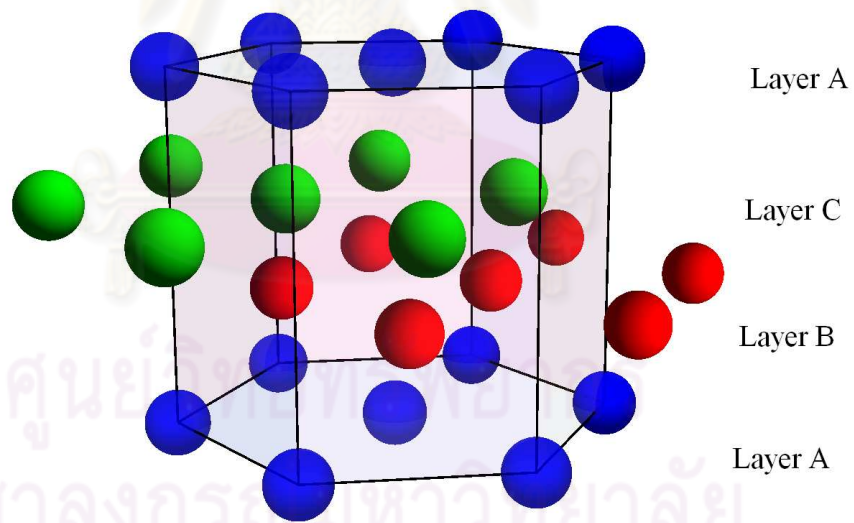


Figure 2.10: The face-centered cubic crystal structure on the (111) plane.

The (111) plane of the face-centered cubic (FCC(111)) structure is quite

different from its (001) plane as shown in Figure 2.10. This plane of the FCC has nine atoms per unit cell. The atomic layers of the FCC(111) are stacked in an ABCABC... fashion, that is the fourth layer lies over the first layer, the fifth layer lies over the second layer, and so on. Each atom has a maximum nearest neighbors of twelve atoms with three atoms at the lower and the upper layers and six atoms at the same layer. The lattice constants of the FCC(111) correspond to the ratio $c/a = \sqrt{6}$. The FCC (111) structure has threefold rotational symmetry.

2.3.5 Simple hexagonal

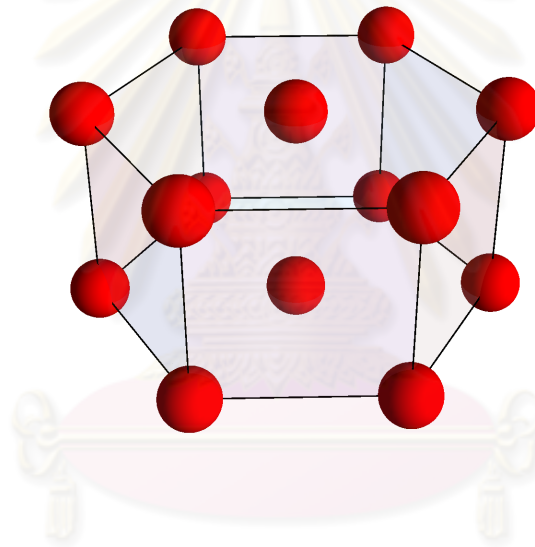


Figure 2.11: The simple hexagonal crystal structure.

A simple hexagonal (SH) crystal structure has three atoms per unit cell and one atomic layer per unit cell, i.e., the locations of the atoms in the vertical direction repeat themselves every atomic layer similar to those in Figure 2.11. Each atom has the maximum nearest neighbors of eight atoms, one atom at the lower and the upper layers and six atoms at the same layer. The lattice constants of the simple hexagonal structure are $a = c$. The simple hexagonal structure has sixfold rotational symmetry.

2.3.6 Hexagonal closed pack

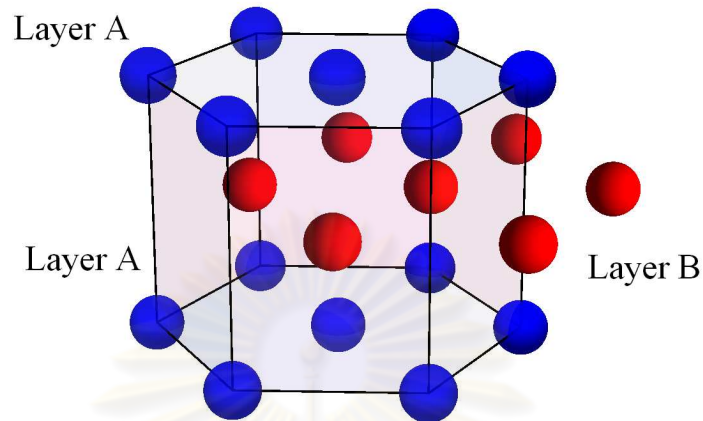


Figure 2.12: The hexagonal closed pack crystal structure.

Hexagonal closed pack (HCP) crystal structure has six atoms per unit cell. Each layer of atoms is stacked in an ABAB... style as is shown in Figure 2.12. The lattice constants ratio $c/a < \sqrt{8/3}$ so that each atom has six nearest neighbor positions with three of them at the lower layer and another at the upper layer. The materials such as Zn, Ti, Cd are HCP. This crystal structure has threefold rotational symmetry.

2.3.7 Ideal hexagonal closed pack

Ideal hexagonal closed pack (iHCP) crystal structure is very similar to the HCP structure (see in Figure 2.13) with six atoms per unit cell and the atoms are stacked in an ABAB... fashion. But the lattice constants ratio of the iHCP $c/a = \sqrt{8/3}$ which results in an increase the number of its nearest neighbor by six positions within the same layer. The crystal symmetry of the iHCP is also threefold rotational symmetry.

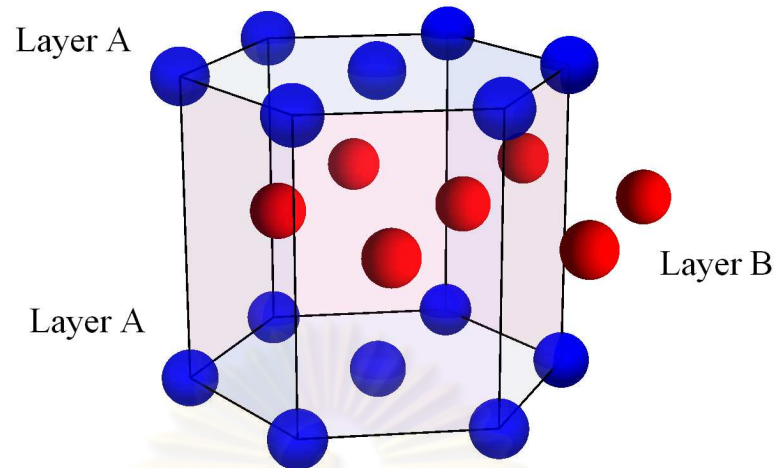


Figure 2.13: The ideal hexagonal closed pack crystal structure.

2.4 Representation of crystal lattices

Conventionally most modelling works are performed on two-dimensional rectangular lattices making them only applicable to simple cubic materials. The periodic boundary condition is completely adequate for this lattice. However, for very complicated lattices such as FCC(111) or iHCP the periodic boundary condition does not a good choice due to insufficient speed in simulations.

To overcome complications in representing any crystalline structures, we adopt the helical boundary conditions [41] which represents any two-dimensional lattice using a one-dimensional chain. This representation of lattice can reduce a multiplication to to find each memory location of a computer which is labelled with a single number. As an example, a site on an $M \times N$ rectangular lattice with coordinates (i, j) is located at the $(iN + j)^{\text{th}}$ element of the chain of length MN (counting from zero). In the square lattice, its four nearest neighbors at $(i \pm 1, j)$ and $(i, j \pm 1)$ are mapped to element number $(i \pm 1) \bmod MN$ and $(i \pm N) \bmod MN$ respectively. Other structures can be constructed in a similar manner. The main advantage of the use of helical boundary conditions over the conventional

ones lies in the flexibility in representing any n -dimensional structure using one-dimensional chain of an arbitrary length (not restricted, e.g., to integer \times integer in the case of simple cubic crystal) resulting in the simplicity of the simulation code.

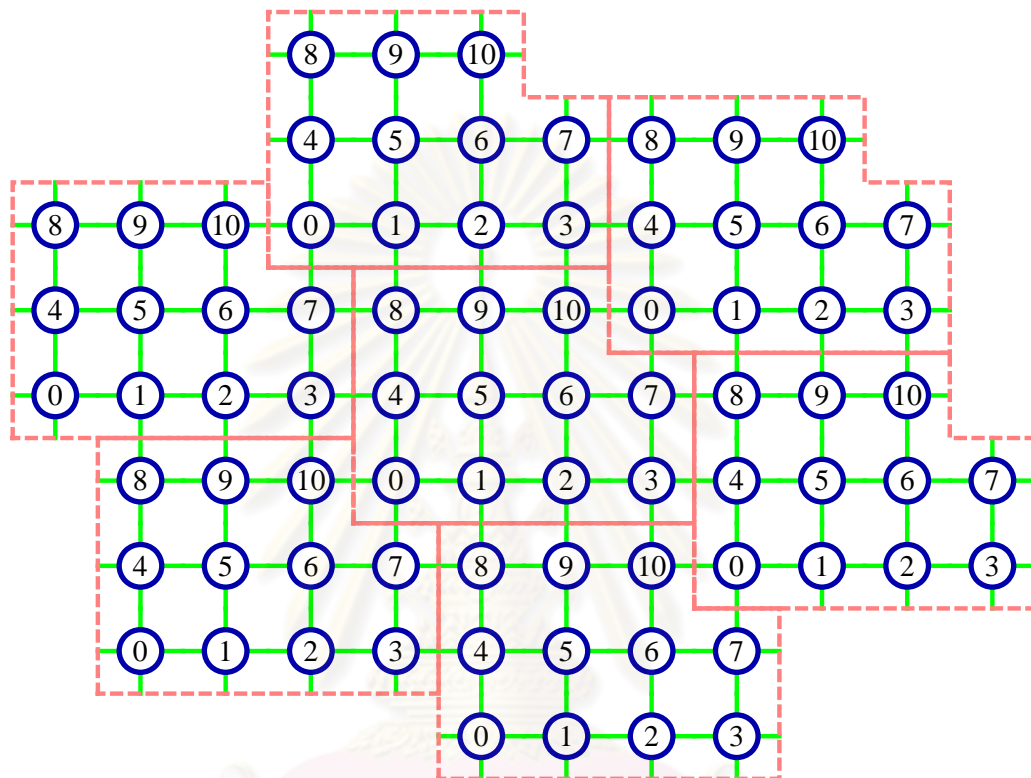


Figure 2.14: Square lattice chain.

Figure 2.14 shows an example of square lattice with a chain of 11 sites with the width of 4 sites. The nearest neighbors of site i are $(i \pm 1) \bmod 11$ and $(i \pm 4) \bmod 11$. Note that the chain can be adjusted so that each row contains all the chain elements.

The triangular lattices with helical boundary condition is shown in Figure 2.15 with lattice site of 11 elements and width of 4 elements. We can represent the triangular lattice in the same way as the square lattice. All six nearest neighbors of site i in this case are located at $(i \pm 1) \bmod 11$, $(i \pm 4) \bmod 11$ and $(i \pm (4 + 1)) \bmod 11$.

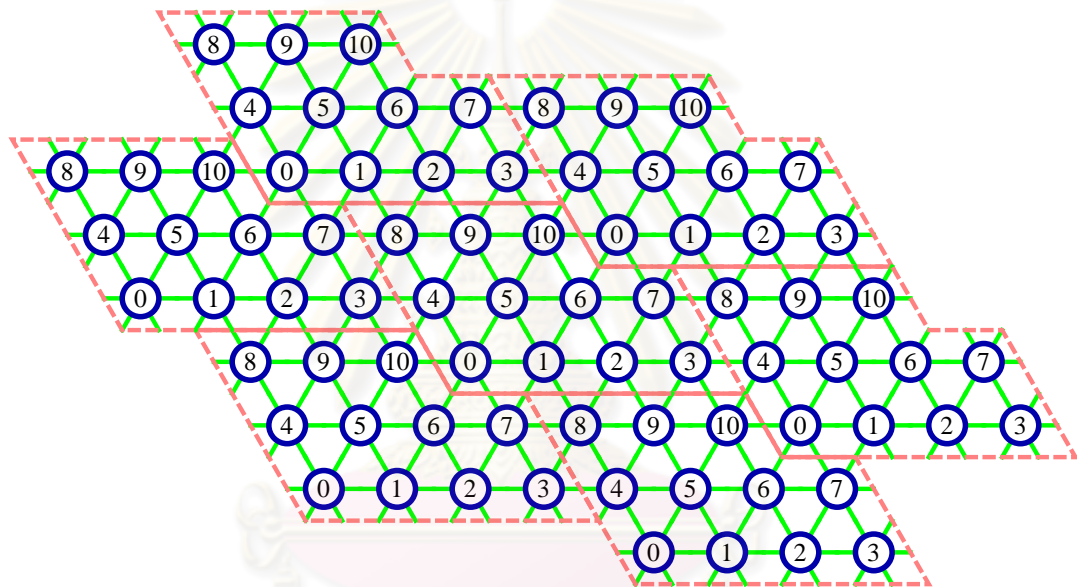


Figure 2.15: Triangular lattice chain.

ศูนย์วิจัยทรัพยากร
จุฬาลงกรณ์มหาวิทยาลัย

CHAPTER III

Simulation results of surface growth

In this chapter, we show the results of the critical exponents and surface morphologies of each crystal structures simulated under both DT and WV models. In all simulations we assume that atoms on the substrate and the film are of the same type so that the film's crystal orientation is the same as that of the substrate and no stress of any kind is produced along the interface. Unlike other conventional simulations where time is measured in units of monolayers, here it is measured in unit-cell layers (UL) since each structure viewed from a different plane may contain a different number of atomic layers. Section 3.1.1 details the calculations of the critical exponents of each crystal structure obeying DT and WV diffusion rules. Data are analyzed and reported in Section 3.1.2. The results of surface morphologies and the descriptions are present in Section 3.2.

3.1 Critical exponents: crystal structures dependent

To investigate both critical exponents and surface morphologies of the select crystal lattices, we perform extensive simulations on chains with 100 to 250,000 elements. Due to the difference in the number of atoms in a unit cell, these numbers translate to, e.g., the substrate of size 10×10 to 500×500 in the case of SC and SH, and roughly 7×7 to 353×353 cells in the case of BCC, HCP and iHCP. In all substrate sizes, the simulations are performed until they reach the

time step beyond the point where the surface roughness W saturates. This value ranges from 10^4 UL for 100 elements, up to 10^7 UL for 250,000 elements.

3.1.1 Results of critical exponents

To find the critical exponents, we need to know saturation time and saturation width of each substrate size and the slopes of interface width as a function of time at an early stage on a log-log scale. From the plots of interface width as a function of time which are shown in Figure A.1 to Figure A.21, we want a systematic method to find the saturation time of each substrate size of each crystal structure. Here we have chosen to use the minimum point of the second derivative of each curve to designate the saturation time t_{sat} . This method gives quite an accurate value of saturation time especially for large substrate size. The dynamical exponent z is computed from the slope of $\log(t_{\text{sat}})$ against the log of lateral substrate size L .

The plot between $W(L, t)$ versus t of every crystal structure both DT and WV model are shown in Appendix A from Figure A.1 to Figure A.21. Each curve is the result of the average of over 100 different configurations for 12800 elements, up to 5000 different configurations for 100 elements. From Equation 2.4, the system size should not have much effect on the value of the slope of these graphs. Because of size effect of the growth exponent β in different timescales, the value of β changes slightly. For each substrate size, we subdivide growth time into three regions: $1 \text{ UL} \leq t_1 \leq t_{\text{sat}}/3$, $t_{\text{sat}}/3 \leq t_2 \leq 2t_{\text{sat}}/3$, and $2t_{\text{sat}}/3 \leq t_3 \leq t_{\text{sat}}$, where t_{sat} denotes the saturation time for that particular substrate size as shown in Figure 3.1. The value of β is calculated from the average between β during t_1 and t_2 . The value of β during timescale t_3 is disregarded because, according to Equation (2.4), β is defined during the early times. The representative value of β for a given crystal structure is obtained from the asymptotic value of the plot between $\beta(L)$ versus $1/L$, the curve can be extrapolated to find the y intercept where $1/L = 0$ or $L \rightarrow \infty$. This method was used in (1+1) dimensional DT

model [42, 43].

The saturation width for a particular substrate size can be calculated from the average value of interface width at the steady state region. To find the roughness exponent α , we compute the slope of $\log(W_{\text{sat}})$ against the log of lateral substrate size L . Plot of $\log(W_{\text{sat}})$ and $\log(t_{\text{sat}})$ against the log of lateral substrate size L are shown in Appendix A from Figure A.29 to Figure A.42. Results of all critical exponents for DT and WV models are summarized in Table 3.1 and 3.2 respectively.

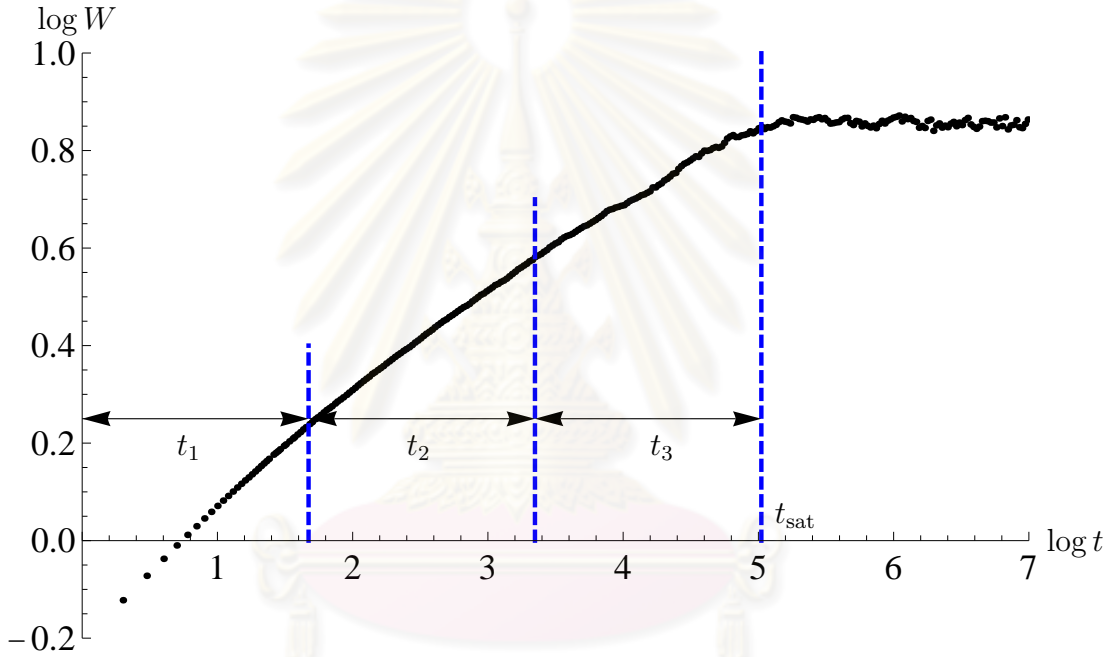


Figure 3.1: Three growth regions: $1 \text{ UL} \leq t_1 \leq t_{\text{sat}}/3$, $t_{\text{sat}}/3 \leq t_2 \leq 2t_{\text{sat}}/3$, $2t_{\text{sat}}/3 \leq t_3 \leq t_{\text{sat}}$, for SC lattice, DT model.

3.1.2 Analyzing the critical exponents

From the results in Table 3.1 and 3.2, we find that the hyper-scaling relation $z = \alpha/\beta$ is *not* generally respected within the simulation accuracy in both models when α is either too high or too low (such as HCP). Albeit some small variations, the values of the growth exponent β agree with the predicted value ($\beta = 1/5$) from

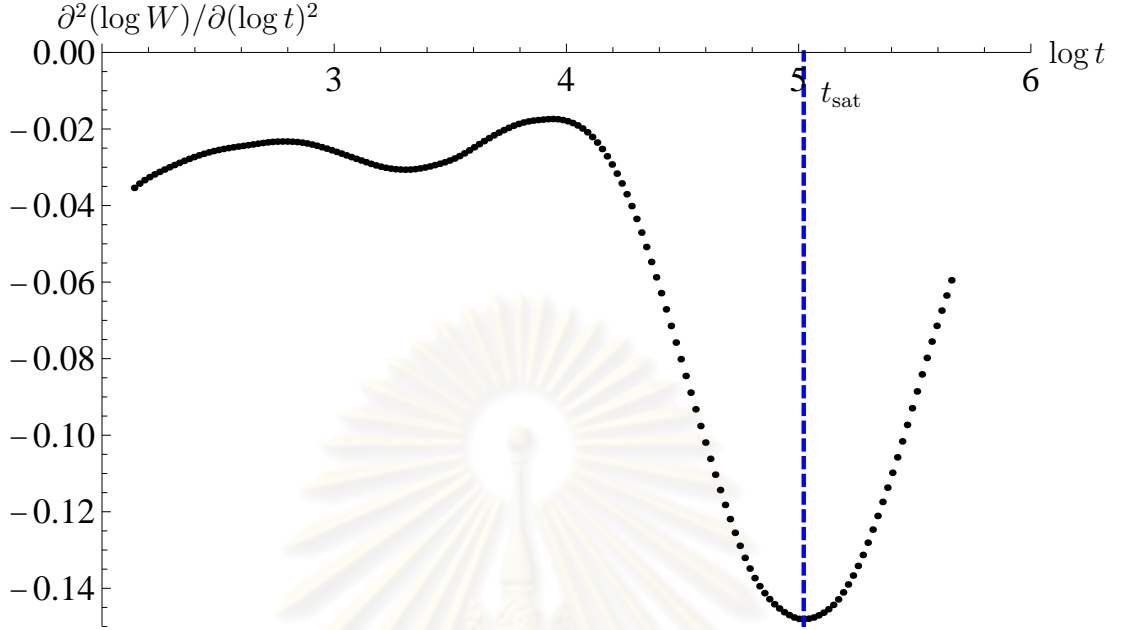


Figure 3.2: The second derivative of interface width as a function of time for SC lattice, DT model.

Table 3.1: The critical exponents of the DT model for all lattice structures, sorted according to α .

Das Sarma–Tamborenea model				
structure	α	β	z	mound
FCC(111)	0.76 ± 0.04	0.20 ± 0.03	3.3 ± 0.2	yes(?)
SH	0.66 ± 0.01	0.21 ± 0.05	3.1 ± 0.1	no
iHCP	0.65 ± 0.01	0.22 ± 0.04	3.2 ± 0.1	no
FCC(001)	0.63 ± 0.02	0.23 ± 0.05	3.2 ± 0.1	no
SC	0.62 ± 0.02	0.22 ± 0.04	3.1 ± 0.1	no
BCC	0.57 ± 0.02	0.24 ± 0.05	3.1 ± 0.2	no
HCP	0.52 ± 0.02	0.24 ± 0.04	2.8 ± 0.2	no

Table 3.2: The critical exponents of the WV model for all lattice structures, sorted according to α .

Wolf–Villain model				
structure	α	β	z	mound
SH	1.12 ± 0.01	0.25 ± 0.03	3.9 ± 0.3	yes
SC	0.94 ± 0.02	0.23 ± 0.02	3.6 ± 0.1	yes
iHCP	0.86 ± 0.02	0.23 ± 0.02	3.5 ± 0.3	yes
FCC(111)	0.83 ± 0.02	0.20 ± 0.04	3.6 ± 0.3	yes
FCC(001)	0.57 ± 0.03	0.19 ± 0.01	3.0 ± 0.2	no
BCC	0.42 ± 0.03	0.20 ± 0.01	1.9 ± 0.2	no
HCP	0.37 ± 0.03	0.20 ± 0.01	2.2 ± 0.2	no

the continuum equation in the case of DT model across all lattice structures. The roughness exponent α and the dynamical exponent z appear to be slightly less than those from the continuum predictions (except for α of FCC(111)). The exponents in the WV case, however, do not seem to conform to the theoretical prediction especially the dynamical exponent ($z = 2$) which ranges from approximately 2 to 4.

The above discrepancy is removed by noticing the last column of Table 3.2 which indicates the existence of mound-like morphologies on each substrate. In the case of BCC and HCP surfaces under WV diffusion rule, the surface front appears to be kinetically rough without any growth instability. We find a complete agreement between the values of the dynamical exponent from the simulations and that from the prediction of the continuum growth equation ($z = 2$). (FCC(001) presents an exceptional case. We shall defer its discussion until Chapter 4.) Upon a closer examination of the last column of Table 3.1 and 3.2, we notice unstable mound-like morphologies for those structures with $\alpha > 0.67$ regardless of the diffusion model. (The reason for the question mark in the case of FCC(111) under DT model shall become evident at the end of Section 3.2.) The separation

between mound and kinetically rough surfaces at a certain value of the roughness exponent has been previously observed in the experiment [44]. The fact that the critical roughness exponent α_c having value greater than 0.67 is consistent with the absence of mound morphology from the simulations of any stable, linear or nonlinear continuum growth equations of up to fourth order without ES barrier; the largest value of α in two spatial dimensions belongs to the MBE universality class with $\alpha = 2/3$.

It should be noted that a “rough” surface indicates a large value of $W(L, t)$. Since we quantify “roughness” according to Equation (2.1), ordered structures such as mounds or pyramids, tend to be “rougher” than scale-invariant, kinetically rough surfaces because the mound regions tend to be much higher, and the troughs of the hills much lower, than the average film height $\langle h(t) \rangle$. It is likely that a large value of the roughness exponent ($\alpha \approx 1$) would indicate mound morphology on a surface. When $\alpha = 1$, one obtains mounds with slope selection, *i.e.*, mounds scale the same way as the lateral substrate dimension. For $\alpha > 1$ ($\alpha < 1$), mounds tend to grow (shrink) in size with a larger substrate. Surfaces that contain visible mounds, therefore, have a large value of α , in contrast to kinetically rough surfaces of small α which appears flat upon taking the thermodynamic limit ($L \rightarrow \infty$).

3.2 Surface morphology and mound formation: crystal structures and diffusion rules dependent

In this section we present our results of surface morphologies of both WV and DT models. Each morphology results from simulation on a chain with 250,000 elements at 10^5 UL. All of the surface morphology pictures are shown in Appendix B Figure B.1 to Figure B.14.

3.2.1 Surface morphologies of different crystal structures

In our simulations, we see mounds forming since an early stage of the growth naturally without any additional efforts for all structures with $\alpha > 0.67$. As time progresses, small mounds shift and coalesce into bigger ones, similar to what was reported from the WV results using the noise reduction technique [27, 32]. The coarsening behavior with mounds of similar sizes during growth implies that the growth front is not scale invariant. The merging of mounds ends at t_{sat} where the correlation length $\xi(t_{\text{sat}})$ is comparable to system's size, and only one mound (and one trough) remains. It is interesting to note that the growth and coarsening of mounds is not stationary; while a large mound subsumes smaller ones in order to grow, its tip does not stand still but shifts sideways in a series of disappearance and reemergence of a peak.

Figure B.1, B.4, B.5 and B.7 show the surface morphologies prior to saturation times using WV model on chains with 250,000 elements of SC, FCC(111), SH and iHCP respectively. These models favor mounds because atoms tend to flow toward kink sites which are most likely to have the highest coordination numbers. DT model, on the other hand, is more inclined to generate a rough surface because adatoms generally stick to their original landings which already have high coordination numbers. Even within the same models, mounds do not assume the same form. Mounds found on SH and FCC(111) simulations exhibit strong geometrical shape. In particular, FCC(111) simulations show a striking ensemble of triangular pyramids similar to many kinetic Monte Carlo (kMC) simulation results at low temperatures [45, 46]. Surfaces of SC and iHCP, on the other hand, only display semi-regular hillocks which do not reflect the underlining lattice structure. Three other lattice structures, namely FCC(001), BCC, and HCP, do not develop visible mounds within WV model.

We do not see the development of mounds in most of our DT simulations on the same set of lattices—with a notable exception of FCC(111) as shown in Figure B.11. While the surfaces of other crystalline structures appear to be

statistically rough, the surface of FCC(111) show round, hemispherical mound morphologies, visually very similar to what was observed in DT model with ES barrier [27] or in high-temperature kMC simulations [23] on simple cubic lattice. The second highest value of α among all lattices simulated using DT model is SH structure. Figure B.12 shows the surface of SH prior to saturation without any apparent mound morphology. The surface of other lattices with a smaller value of α exhibits a statistically rough interface as traditionally expected from a standard DT simulation. On a closer examination, however, we find that the development of mounds on FCC(111) surface using DT model is quite different from the ones using WV model. Mounds, in this case, do not arise from island formations and coarsening of smaller mounds into larger ones. Initially the surface appears to be statistically rough. As time progresses, the regions which are later to become mounds, develop small cracks around them. The cracks then deepen, forming narrow troughs which gradually enlarge, splitting the original surface into many mounds. The perception of mound growth is in fact the deepening and broadening of the troughs. Finally at late times, small mounds start to merge by the progressive disappearance of troughs which separate them. We suspect that in this stage, the correlation length $\xi(t)$ dictates the size of each mound (which is comparable to the substrate size as the saturation time is reached).

Figure 3.3 and 3.4. show the $\log W$ as a function of $\log t$ for chains with 250,000 elements of DT and WV model respectively. We can see from the curve of FCC(111) structure obeying DT model that, the slope of this curve changes rapidly at t approximately equal to 10^5 UL ($\log t \approx 5$). This is the point in time that surface begins to crack which results in rapid increase of the slope. For other structures of DT model at the same region of time, the interface width tends to saturate at a particular time which corresponds to kinetically rough surfaces. However, interface width at any time step under WV diffusion rule of SC, FCC(111), SH and iHCP, which exist mounds on the surfaces, does not increase rapidly as is the case in FCC(111) under DT model.

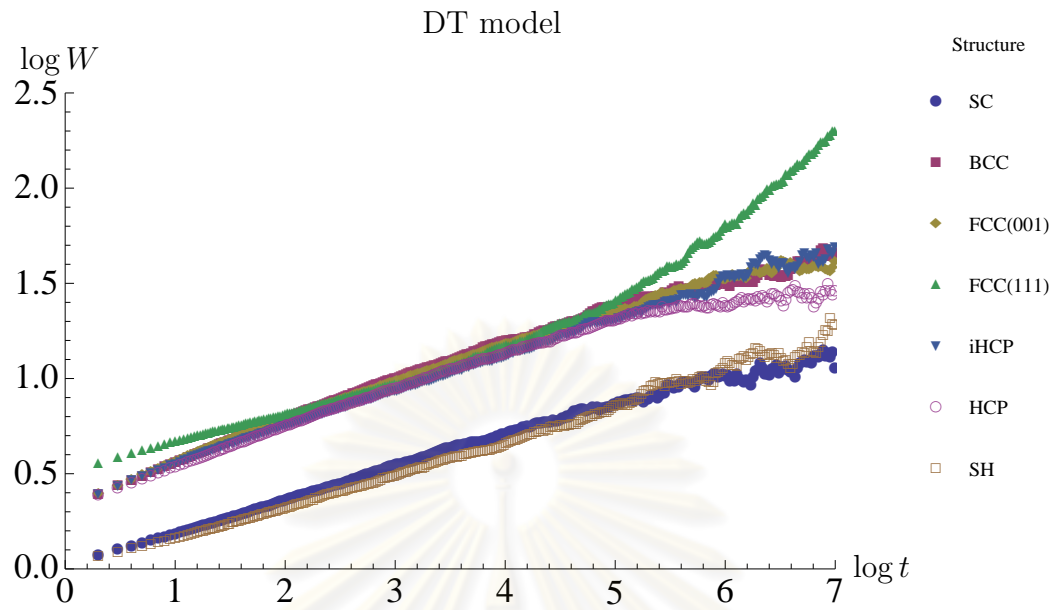


Figure 3.3: The interface width as a function of time of DT model for chains with 250,000 elements.

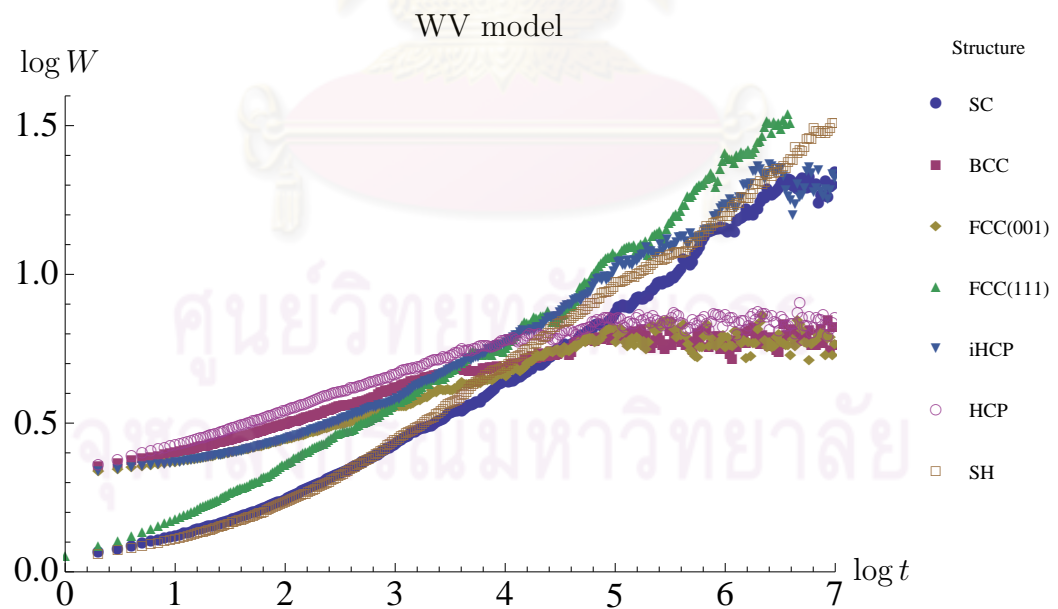


Figure 3.4: The interface width as a function of time of WV model for chains with 250,000 elements.

3.2.2 Correlation functions

In this section, we discuss the properties of the surface morphologies by using the height-height correlation functions. The graphs of the correlation function of each crystal structure of WV and DT models are shown in Figure B.15 to Figure B.28. All of them show the correlation functions $C(\vec{r})$ as a function of $\vec{r} = (x, y)$ at $t = 10^5$ UL. We clip the center of the graphs where the correlation functions grow up to the maximum value (the red region), to suppress the height in order to see the oscillations of the functions. The positions where the correlation functions are positive (negative) are painted in red (blue) color. Black lines indicate zero of the correlation functions. Each graph is a result of an average over ten runs. It should be noted that the existence of mounds on the surface results in the oscillations of the correlation functions. All of them have reflection symmetries with respect to x and y axes.

Figure B.15 to Figure B.21 represent the correlation functions $C(\vec{r})$ of WV model corresponding to the surface morphologies of Figure B.1 to Figure B.7. We can see that the correlation functions of the SC, FCC(111), SH and iHCP oscillate with \vec{r} indicating mounded patterns on the surfaces. Let us concentrate on the correlation functions of FCC(111) and SH structures which display clear oscillations. The number of peaks (valleys) of the SH in the case of SH (Figure B.19) is greater than that in FCC(111) (Figure B.18) which implies that the number of mounds (troughs) on the surface of SH in Figure B.19 is also greater than that of FCC(111) in Figure B.4. The sizes of the oscillations in FCC(111) and SH structures are greater than that in SC and iHCP structures which means that the SC and iHCP lattices have less regularity of size and shape of mounds than FCC(111) and SH structures do. The correlation function of the BCC, FCC(001) and HCP structures of WV model, on the other hand, do not oscillate with \vec{r} as shown in Figure B.16, B.17 and B.20 respectively. This confirms the kinetically rough growth process without mound formation on the surfaces in Figure B.2, B.3 and B.6.

The correlation functions of the structures obeying DT growth model are shown in Figure B.22 to Figure B.28. For SC and SH structures, we can see small oscillations of the correlation in some directions. We, however, do not see any mound patterns on the surfaces of SC and SH structures in Figure B.8 and Figure B.12. We believe that the oscillation of the function in this situation occurs from too much noise on the surfaces.

For the FCC(111) structure, the correlation function $C(\vec{r})$ oscillates with \vec{r} which indicates the existence of mounds on the surface. We focus on the FCC(111) structure of DT and WV models. By comparing the FCC(111) structure from WV model with the FCC(111) from DT model, we find that the amplitude of the correlation function of the FCC(111) obeying DT model is generally greater than that of WV model. This is because the average mound height of the FCC(111) from DT model greater than that from WV model. We can see from Figure B.11 that the surface in this figure has very deep and narrow troughs compared with that of WV model. This implies that the average mound height (height of mounds and troughs) of DT model is greater than that of WV model.

The correlation functions of the remaining structures of DT model which are BCC, FCC(001), HCP and iHCP are very noisy as seen in Figure B.23, B.24, B.27 and B.28. We suspect that the oscillations of the correlation functions in these stage occur due to too much noise on the surfaces during growth process and the number of the ensemble averages is inadequate.

3.2.3 Mounds and mechanism of mound formation

It was well established that Ehrlich–Schwoebel (ES) barrier, which prevents an atom on a terrace to hop down, could explain the formation of mound-like structures observed in many MBE growth experiments [12, 47, 48]. Since then several authors [27, 49] have proposed a topologically induced probabilistic current known as step-edge diffusion (SED) current as an additional cause of mound formation. SED current arises from the greater likelihood for an atom to move

along the edge of a terrace toward a kink site. Their analysis, however, was based on the simple cubic structure. It is very unlikely that SED current is the only type of probabilistic, topological current in existence. An array of other geometrically more complicated crystalline structures could give rise to a new class of current.

3.2.4 Terrace current and step edge current

To understand the mechanism of mound formation in both models, one should examine the area nearby a terrace edge which separates two flat regions. One commonly accepted explanation as to why an island nucleation leads to the formation of a large mound-like structure is due to the flow of atoms, on average, towards the mound region resulting in the net “uphill” current [20, 50, 5, 51, 52]. Without appealing to the use of ES barrier, we consider a topologically induced uphill current in the spirit of SED current. As anticipated, we find that all of the lattice structures that develop mounds appear to have SED current. To our surprise however, the conventional SED current is almost always cancelled by local downhill current. We also discover that SH and FCC possess yet another type of geometrically induced current. Unlike SED current which flows *along* an edge of a terrace towards a kink site, the new current flows in the perpendicular direction towards the edge. We believe that the reason why this “terrace diffusion” (TD) current has never been observed is because in SC, where most simulations [49, 25] are based on, an equal and opposite current flows downhill. The uphill and downhill currents thus, on average, cancel each other leaving only SED current. It is worth mentioning that TD current is analogous to the edge ES current, whereas SED current is to kink ES current. The difference is that the edge ES current may occur on a one dimensional substrate, while TD current is only present on some crystalline lattices in two spatial dimensions.

To illustrate the difference between SED and TD, consider a step terrace lying along the [1000] direction of a SH(001) substrate as shown in Figure 3.5. Atoms on the upper terrace are denoted by empty circles while those on the

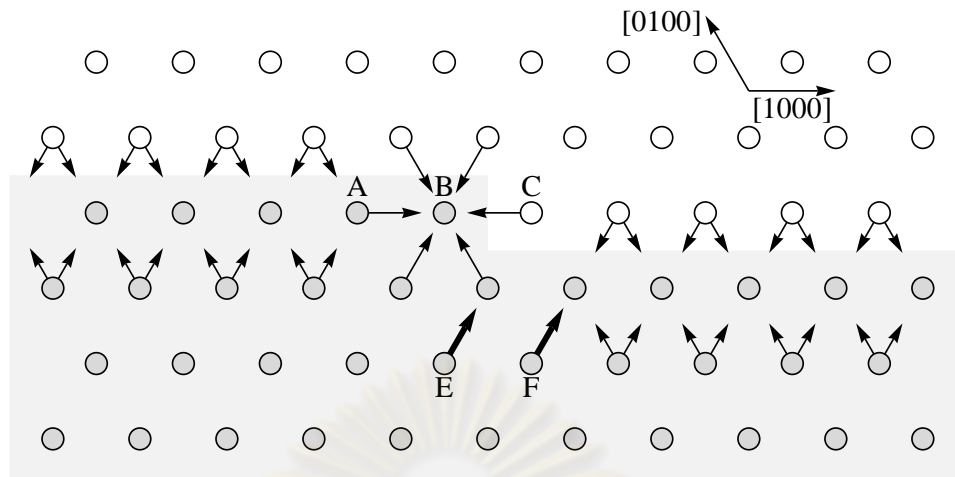


Figure 3.5: Local probabilistic currents near a step edge along $[1000]$ direction of $SH(0001)$ with a step dent. Shaded circles represent atoms on the lower terrace while light circles depict those on the upper terrace. An atom dropping on any lattice site will move, according to WV rule, to one of sites along the corresponding arrow. An atom will not move if it falls on a site without an arrow. An atom falling on site A, in particular, will be driven towards a kink site B producing a small SED current. This current is however cancelled by another downhill current from C to A. Global net currents are denoted by thick arrows.

lower terrace are represented by shaded circles. According to WV model, a newly deposited atom which falls far from the edge of the terrace will not move. The one that falls within the proximity of the edge will advance along the direction(s) as shown by the arrow(s) in order to maximize its bondings. A site with two or more arrows indicates that there is an equal probability for an atom dropping on it to move in one of the allowed directions. Along the flat region away from the kink, atoms tend to move uphill as much as they move downhill resulting in a net zero flux. Near the kink site, we find that an uphill flux tends to occur more often. Note in particular that if an atom falls onto position A which situates on the edge, it will be attracted toward the kink position B creating a small SED current. Since WV diffusion rule only allows an atom to move to one of the nearest neighbors, the SED current only extends a distance of one atomic position. On average, however,

a particle *does not* tend to move uphill as a result of this current because there is another current flowing downhill in the opposite direction (from C to B) with the same strength. Nevertheless there is a net current in the uphill direction near the corner of the terrace edge at position E and F. It is not a SED current in the traditional sense since the direction of the flow is not along the edge but at an angle towards the corner. For the lack of a better word, we shall still refer to it as step-edge diffusion current because the current still appears in the neighborhood of a kink site and has a component parallel to a terrace edge.

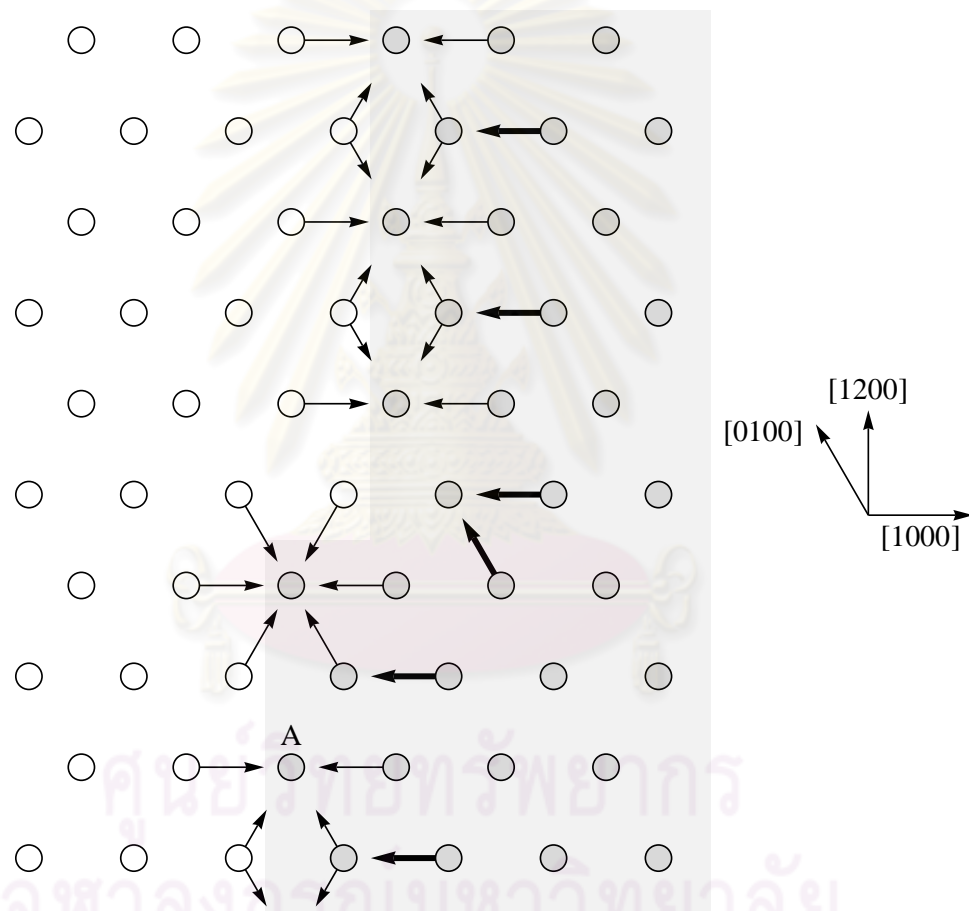


Figure 3.6: Local probabilistic currents near a step edge along $[1200]$ direction of SH(0001). The upper terrace is on the left side while the lower terrace on the right. There is a net uphill terrace current acting along the $[\bar{1}000]$ direction. Noncancelling currents are indicated by thick arrows.

The situation is even more perplexing for a step terrace along another high-

symmetry direction, the $[1200]$ direction, as shown in Fig. 3.6. Notice that an atom falling onto position A next to the kink site does not move toward the site. No (traditional) SED current exists along this direction. We, however, find a net a noncancelling flux of currents (thick arrows) flowing perpendicular to the terrace edge in the uphill direction. This flux would serve to extend the base of the terrace in a future time step. (We shall discuss, in Chapter 4, a notable exception of FCC(001) where a non-zero current does not lead to the formation of mounds.) To our knowledge, this type of topological current has never been reported in the literature. Near the corner, there also exists a SED current similar to those in Figure 3.5. Table 3.3 gives a summary of the type of currents along a given direction during the growth on SH, SC, iHCP, FCC(111), and FCC(001) surfaces. The upper terrace resides on the inside of the geometrical figures. It is interesting to note that FCC(111) simulations show very strong triangular pyramidal mounds oriented in the same direction, and never an inverted triangular version. We believe that this is due to the difference between the symmetry of the two types of currents; TD current is only three-fold symmetric while TD current has a six-fold symmetry. The preferred faces are oriented perpendicular to the directions of the TD currents, forming an upright triangular pyramid. The other structures whose surface has irregular mounds, namely SC and iHCP, are devoid of the TD currents. In addition to the edge ES current, TD current should cause an instability forming equilibrium faceting along some vicinal surfaces.

For BCC and HCP, mounds are not observed and neither type of current is present. Consider as an example the current consideration in the case of BCC(001), obeying WV model. Figure 3.7 shows three layers of atoms. Full circles signify occupied lattice sites. If an atom falls on one of these positions, it would have to move along a direction designated by one of the arrows towards an unoccupied site (dashed circle). Not only does a net current not exist, locally it flows perpendicularly *away* from the terrace edge in both directions. Any atom deposits near the edge will likely be pushed away from it which implies that had an island been formed, its territory would not have been extended by this process.

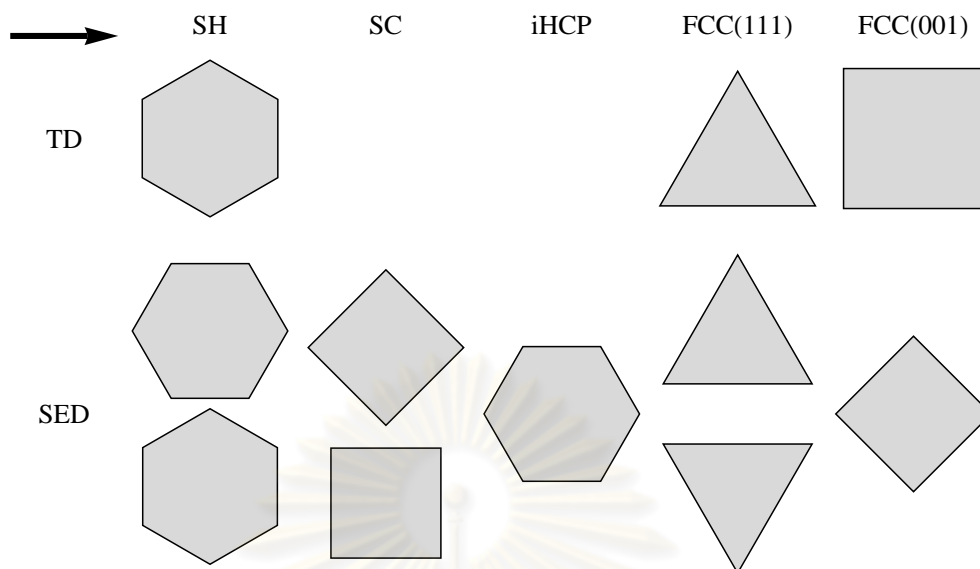


Table 3.3: Edges of SH, SC, iHCP, FCC(111) and FCC(001) are shown where the corresponding terrace diffusion (TD) and step-edge diffusion (SED) currents are nonzero, calculated based on WV diffusion rule. Upper terraces are shown in gray. The horizontal direction, indicated by the arrow on the upper left hand corner, designates the $[100]$ direction for SC and FCC(001), $[1000]$ direction for SH and iHCP, and $[1\bar{1}0]$ direction for FCC(111).

In addition, we also do not find any current flowing along the edge towards a kink site. In fact, if an atom falls exactly at the kink position, it will diffuse away from the kink. This counter-intuitive behavior arises from the fact that, for BCC, lattice sites along a terrace edge have the lowest coordination numbers. Moving towards these sites in the uphill direction from the bottom terrace would therefore cost more energy. A closer inspection shows that atoms at the bottom of the edge already bond with those at the top. An atom which falls on either of these two rows adjacent to the edge can only roll away from the edge. The step edge in this case serves as a topological barrier preventing an atom to cross side. The same situation also happens in a HCP lattice whose surface is also mound-free.

We end this section by giving a brief account of the DT simulation results. As discussed at the end of Section 3.2.1, no island formations are observed on

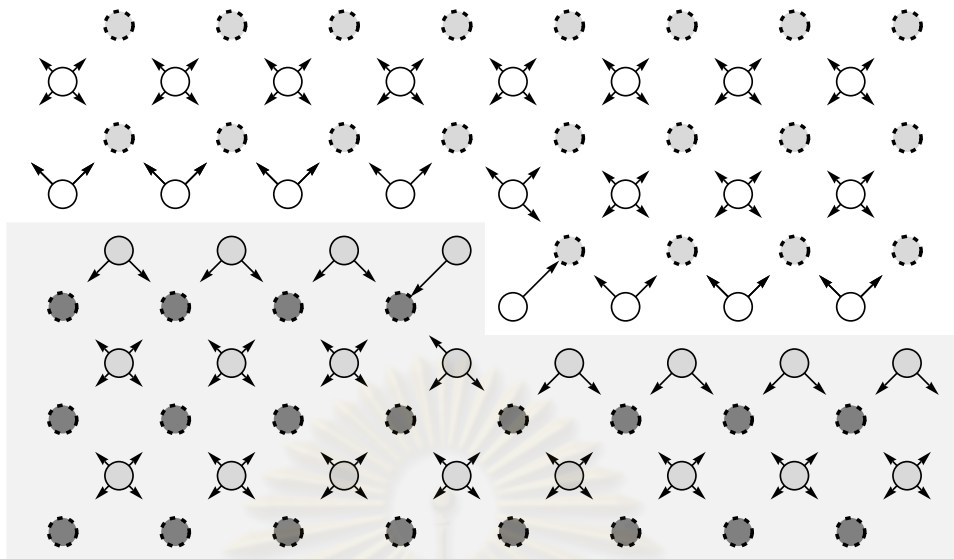


Figure 3.7: A step edge along the $[100]$ direction separates the lower region (on the bottom of the figure) and the upper region (on the top). Three atomic layers are present with a lighter shade signifies a higher layer. Occupied lattice sites are represented by full circles while dashed circles denote unoccupied ones. Locally atoms tend to move away from the terrace edge.

the surface of these lattices, even in the case of FCC(111) where mounds are present. This is consistent with the fact that we do not find any non-zero uphill TD or SED currents on any structure in any direction. Other than FCC(111), all surfaces appear to be kinetically rough with early-time behavior following a power law.

ศูนย์วิทยทรัพยากร
จุฬาลงกรณ์มหาวิทยาลัย

CHAPTER IV

Conclusions

Through large-scale Monte Carlo simulations, we have analyzed MBE growth of thin films on several lattice structures based on WV and DT models in 2+1 dimensions. We discover that at the roughness exponent of around 0.67-0.76, the surface morphology of the film changes from being kinetically rough with power law scaling to quasi-regular mound-like structures. Without ES barrier, we attribute the morphological difference to the appearance of topologically induced, probabilistic particle currents. These currents not only arise from the line tension along the step edges separating several terraces of each mound in the form of SED current, they can also emerge perpendicular to flat straight terrace edges in the uphill direction in the form of TD current. The latter only manifests itself in SH and FCC lattices among several others that we have observed.

It is clear that the evolution of surface morphology depends not only on lattice dimension but also on material's crystal structure. In describing the growth of a lattice structure obeying a particular diffusion rule, the values (and signs) of the parameters (ν_2 , ν_4 , λ_{13} , λ_{22} and D) in the associated continuum growth equation need to be adjusted accordingly. The growth morphology are primarily categorized into two classes: kinetically rough scale-invariant or unstable mounding surface. We find that the separation between these two growth regimes occurs at the roughness exponent α of around 0.66 regardless of the prescribed diffusion rule. Further analytical study is needed to explain the origin of this magic number. For kinetically rough surfaces, the dynamical scaling theory seems to give an accurate description of the behavior of the growth interface using power laws.

On the contrary, for destabilized mounding morphologies, the growth needs to be described in terms of island nucleation and island coarsening. We shall leave the analysis of the dynamics of mound coarsening in limited mobility diffusion models for future work.

Contrary to Ref. [27], we are able to obtain mound morphology without any noise reduction technique. In our simulations we find that mounds are recognizable after its lateral size reaches about 100 atomic units. We do not see mounds comparable in size to theirs. Our supposition is that since we expect the parameters of the corresponding continuum growth equation to be substrate dependent, the uphill diffusion term $-|\nu_2|\nabla^2 h$ may overcome the Mullin-type diffusion term $-|\nu_4|\nabla^4 h$, which tends to suppress small fluctuations, at the length scale given by $l_c \sim \sqrt{|\nu_4/\nu_2|}$. This length scale l_c , in some crystal structure, may be larger than the attempted substrate simulation scale, thus, mounds may never be observed. In addition our mounds are much more irregular than the ones obtained using the noise reduced scheme. Our value of α for SC is very close to one which implies that mounds have a selective slope in agreement with Ref. [32]. We believe that the noise reduction technique, in most cases, serves to amplify the mound shape and is not a necessary scheme to produce mounds.

A few remarks are in order regarding the topological currents. Our observation leads us to believe that the mechanism of mound formation within our framework is due to both the kink SED current and the straight TD current. The latter serves as an extra role in enhancing the faceted structure of mounds on the surface where it exists. It is true that other, more complicated, edge shapes exist which could cause other geometrical currents. In a certain coarse-graining sense, dimples and pits can be generated by one kink/corner step similar to the ones in Figure 3.5, 3.6 and 3.7. We still believe that these currents can be largely categorized into curvature-dependent versus straight terrace edge type of current. In his review article,[20] Krug argued that SED current induces $\vec{J}_{\text{SED}} \sim \vec{\nabla}\kappa(h)$, where κ is the local curvature of $h(\vec{x}, t)$ on the plane of the substrate. This results in $\sim \nabla^4 h$ in Equation (2.9). Physically this term emerges as a result of the line

tension due to the curvature of terrace edge. The TD current, on the other hand, appears even when the radius of curvature is infinite. Given $m \equiv |\hat{n} \cdot \vec{\nabla}h|$ where \hat{n} defines the direction along which the current is active, TD current gives rise to the anti-diffusive flow along the uphill direction $\vec{J}_{\text{TD}} \sim \hat{n} m / (1 + m^2)$ which is approximately $\sim \hat{n} m$ for a small surface slope [3]. Our findings suggest that both \vec{J}_{SED} and \vec{J}_{TD} only act along certain preferred directions according to the underlying lattice structure. (In the case of FCC(111), for example, the TD current may point along one of the following three directions: $[112]$, $[\bar{2}1\bar{1}]$ or $[1\bar{2}\bar{1}]$.)

Our simulations also suggest that, in most structures with surface growth instability, local current tends to flow towards the bottom of a terrace edge both from the upper and lower terraces. (See, e.g., Figure 3.5 and 3.6.) On a kinetically rough surface such as that of BCC and HCP, we observe the local current which flows away from the bottom of a terrace edge, similar to what is seen in Figure 3.7. Although the effect of this current tends to average out on a larger scale, its existence gives rise to the current of the form $\vec{J}_{\text{local}} \sim \pm \hat{n} (\hat{n} \cdot \vec{\nabla})^2 h$. This translates to a new term proportional to $(\hat{n} \cdot \vec{\nabla})^3 h$ in the continuum equation. (On a one dimensional substrate, this is simply $\partial^3 h / \partial x^3$.) This term has been previously neglected based on the rotation and inversion symmetry about the growth direction. Given an anisotropy of each lattice structure, we do not believe that the new term should be discarded from future investigations.

We see a different mound formation process on FCC(111) plane under DT diffusion rule. The traditional picture of island nucleation, followed by particle accretion and mound coarsening may not give an accurate description of the DT structural formation. Without any net uphill currents, we expect a completely different mechanism at work. Visually, mounds on FCC(111) plane do not possess up-down symmetry as the ones obtained using WV diffusion rule. This is, however, typical of DT growth morphology. We therefore still expect the DT terms ($-\nu_4 \nabla^4 h$ and $\lambda_{22} \nabla^2 (\vec{\nabla}h)^2$) to still be effective in the continuum growth equation. In light of the supposed anisotropy term that might be present, a complete understanding demands a more thorough theoretical investigation of the growth equation.

Finally we study the height-height correlation function to confirm the existence of mounds on the surfaces. The correlation function of FCC(111) and SH structures under WV model and FCC(111) under DT model display clear oscillation which agrees with regular mound pattern on the film surfaces. In the cases of SC and iHCP structures obeying WV diffusion rule, the correlation functions also oscillate but a smaller amplitude. This result suggests that, there are mounds on the surfaces with less regular pattern compared to that of FCC(111) and SH structures because the SC and iHCP do not have TD current. Other structures of DT and WV diffusion rules, which contain no mound on their surfaces, will produce a correlation function without oscillation. The surfaces of the BCC and HCP structures under WV model and every structure of DT model (except for FCC(111)) are kinetically rough because these structures have neither SED or TD current on the film surfaces.



ศูนย์วิทยาศาสตร์
จุฬาลงกรณ์มหาวิทยาลัย

References

- [1] Chambers, S. A.. Epitaxial growth and properties of thin film oxides. *Surf. Sci. Repo.* 39 (2000): 105–80.
- [2] Arthur, J. R.. Molecular beam epitaxy. *Surf. Sci.* 500 (2002): 189–217.
- [3] Barabási, A.-L. and Stanley, H. E.. *Fractal Concepts in Surface Growth*. Cambridge University Press: Cambridge, MA. 1995.
- [4] Pimpinelli, A. and Villain, J.. *Physics of Crystal Growth*. Cambridge University Press: Cambridge, UK. 1998.
- [5] Moldovan, D. and Golubović, L.. Interfacial coarsening dynamics in epitaxial growth with slope selection. *Phys. Rev. E* 61 (2000): 6190–214.
- [6] Ernst, H.-J., Fabre, F., Folkerts, R., and Lapujoulade, J.. Observation of a growth instability during low temperature molecular beam epitaxy. *Phys. Rev. Lett.* 72 (1994): 112–5.
- [7] Coluci, V. R., Cotta, M. A., Mendonça, C. A. C., I-Landers, K. M., and de Carvalho, M. M. G.. Surface morphologies in gaas homoepitaxy: Mound formation and evolution. *Phys. Rev. B* 58 (1998): 1947–53.
- [8] Nostrand, J. E. V., Chey, S. J., and Cahill, D. G.. Low-temperature growth morphology of singular and vicinal ge(001). *Phys. Rev. B* 57 (1998): 12536–43.
- [9] Kalff, M., Šmilauer, P., Comsa, G., and Michely, T.. *Surf. Sci.* 426 (1999): L447.
- [10] Finnie, P. and Homma, Y.. Island growth and surface roughness scaling of epitaxial gaas on si observed by in situ scanning electron microscopy. *Phys. Rev. B* 59 (1999): 15240–5.

- [11] Fauster, T., Reuß, C., Shumay, I. L., and Weinelt, M.. Influence of surface morphology on surface states for Cu on Cu(111). *Phys. Rev. B* 61 (2000): 16168–73.
- [12] Néel, N., Maroutian, T., Douillard, L., and Ernst, H.-J.. From meandering to faceting, is step flow growth ever stable?. *Phys. Rev. Lett.* 91 (2003): 226103.
- [13] Ehrlich, G. and Hudda, F. G.. Atomic view of surface self-diffusion: Tungsten on tungsten. *J. Chem. Phys.* 44 (1966): 1039–49.
- [14] Schwoebel, R. L. and Shipsey, E. J.. Step motion on crystal surfaces. *J. Appl. Phys.* 37 (1966): 3682.
- [15] Schwoebel, R. L.. Step motion on crystal surfaces ii. *J. Appl. Phys.* 40 (1969): 614.
- [16] Villain, J.. Continuum models of crystal growth from atomic beams with and without desorption. *J. Phys. I* 1 (1991): 19–42.
- [17] Liu, S. J., Huang, H., and Woo, C. H.. Schwoebel-ehrllich barrier: from two to three dimensions. *Appl. Phys. Lett.* 80 (2002): 3295–7.
- [18] Lagally, M. G. and Zhang, Z.. Thin-film cliffhanger. *Nature* 417 (2002): 907–10.
- [19] Burton, W. K., Cabrera, N., and Frank, F. C.. The growth of crystals and the equilibrium structure of their surfaces. *Phil. Trans. R. Soc. (Lond.) A* 243 (1951): 299.
- [20] Krug, J.. Origins of scale invariance in growth processes. *Advances in Physics* 46 (1997): 139–282.
- [21] Politi, P. and Villain, J.. Ehrlich–schwoebel instability in molecular-beam epitaxy: A minimal model. *Phys. Rev. B* 54 (1996): 5114.

- [22] Camarero, J. et al.. Epitaxial growth of metals with high ehrlich—schwoebel barriers and the effect of surfactants. *Appl. Phys. A* 69 (1999): 553–7.
- [23] Schinzer, S., Köhler, S., and Reents, G.. Ehrlich-schwoebel barrier controlled slope selection in epitaxial growth. *Eur. Phys. J. B* 15 (2000):.
- [24] Liu, Z.-J. and Shen, Y. G.. Temperature effect on surface roughening of thin films. *Surf. Sci.* 595 (2005): 20–9.
- [25] Murty, M. V. R. and Cooper, B. H.. Instability in molecular beam epitaxy due to fast edge diffusion and corner diffusion barriers. *Phys. Rev. Lett.* 83 (1999): 352–5.
- [26] Pierre-Louis, O., D’Orsogna, M. R., and Einstein, T. L.. Edge diffusion during growth: The kink ehrlich-schwoebel effect and resulting instabilities. *Phys. Rev. Lett.* 82 (1999): 3661–4.
- [27] Chatrathorn, P. P., Toroczkai, Z., and Das Sarma, S.. Epitaxial mounding in limited-mobility models of surface growth. *Phys. Rev. B* 64 (2001): 205407.
- [28] Das Sarma, S. and Tamborenea, P. I.. *Phys. Rev. Lett.* 66 (1991): 325.
- [29] Tamborenea, P. I. and Sarma, S. D.. Surface-diffusion-driven kinetic growth on one-dimensional substrates. *Phys Rev E* 48 (1993): 2575.
- [30] Wolf, D. E. and Villain, J.. Growth with surface diffusion. *Europhys. Lett.* 13 (1990): 389–94.
- [31] Chatrathorn, P. P. and Das Sarma, S.. Layer-by-layer epitaxy in limited mobility nonequilibrium models of surface growth. *Phys. Rev. E* 66 (2002): 041601.
- [32] Das Sarma, S., Chatrathorn, P. P., and Toroczkai, Z.. Universality class of discrete solid-on-solid limited mobility nonequilibrium growth models for kinetic surface roughening. *Phys. Rev. E* 65 (2002): 036144.

- [33] Oliveira, T. J. and Aarão Reis, F. D. A.. Finite-size effects in roughness distribution scaling. *Phys. Rev. E* 76 (2007): 061601.
- [34] Kardar, M., Parisi, G., and Zhang, Y.-C.. Dynamics scaling of growing interfaces. *Phys. Rev. Lett.* 56 (1986): 889–92.
- [35] Eden, M.. A two-dimensional growth process. in *Proceedings of the Fourth Berkeley Symposium on Mathematical Statistics and Probability*, edited by Neyman, F.. volume IV. pages 223–39. The University of California at Berkeley. Univ. of Calif. Press. 1961.
- [36] Witten, T. A. and Sander, L. M.. Diffusion-limited aggregation, a kinetic critical phenomenon. *Phys. Rev. Lett.* 47 (1981): 1400–3.
- [37] Bazant, M. Z., Choi, J., and Davidovitch, B.. Dynamics of conformal maps for a class of non-laplacian growth phenomena. *Phys. Rev. Lett.* 91 (2003): 045503.
- [38] Edwards, S. F. and Wilkinson, D. R.. The surface statistics of a granular aggregate. *Proc. Royal Soc. London A* 381 (1982): 17–31.
- [39] Haselwandter, C. A. and Vvedensky, D. D.. Multiscale theory of fluctuating interfaces: Renormalization of atomistic models. *Phys. Rev. Lett.* 98 (2007): 046102.
- [40] Haselwandter, C. A. and Vvedensky, D. D.. Renormalization of stochastic lattice models: Epitaxial surfaces. *Phys. Rev. E* 77 (2008): 061129.
- [41] Newman, M. E. J. and Barkema, G. T.. *Monte Carlo Methods in Statistical Physics*. Clarendon Press: Oxford, UK. 1999.
- [42] Costa, B. S., Euzébio, J. A. R., and Aarão Reis, F. D. A.. Finite-size effects on the growth models of das sarma and tamborenea and wolf and villain. *Physica A* 328 (2003): 193.

- [43] Araújo Reis, F. D. A.. Numerical study of discrete models in the class of the nonlinear molecular beam epitaxy equation. *Phys Rev E* 70 (2004): 031607.
- [44] Lengel, G. et al.. Nonuniversality in mound formation during semiconductor growth. *Phys. Rev. B* 60 (1999): R8469.
- [45] Ovesson, S., Bogicevic, A., and Lundqvist, B. I.. Origin of compact triangular islands in metal-on-metal growth. *Phys. Rev. Lett.* 83 (1999): 2608–11.
- [46] Albe, K. and Müller, M.. Cluster diffusion and island formation on fcc(111) metal surfaces studied by atomic scale computer simulations. *Int. Numer. Math.* 149 (2005): 19–28.
- [47] Zuo, J.-K. and Wendelken, J. F.. Evolution of mound morphology in reversible homoepitaxy on cu(100). *Phys. Rev. Lett.* 78 (1997): 2791–4.
- [48] Yoon, J.-G., Oh, H. K., and Lee, S. J.. Growth characteristics and surface roughening of vapor-deposited mgo thin films. *Phys. Rev. B* 60 (1999): 2839–43.
- [49] Biehl, M., Kinne, M., Kinzel, W., and Schinzer, S.. A simple model of epitaxial growth: the influence of step edge diffusion. *Comput. Phys. Comm.* 121–122 (1999): 347–52.
- [50] Golubović, L.. Interfacial coarsening in epitaxial growth without slope selection. *Phys. Rev. Lett.* 78 (1997): 90–93.
- [51] Politi, P. and Krug, J.. Crystal symmetry, step-edge diffusion, and unstable growth. *Surf. Sci.* 446 (2000): 89–97.
- [52] Krug, J.. Four lectures on the physics of crystal growth. *Physica A* 313 (2002): 47–82.



APPENDICES

ศูนย์วิทยทรัพยากร
จุฬาลงกรณ์มหาวิทยาลัย

Appendix A

The plots of the critical exponents

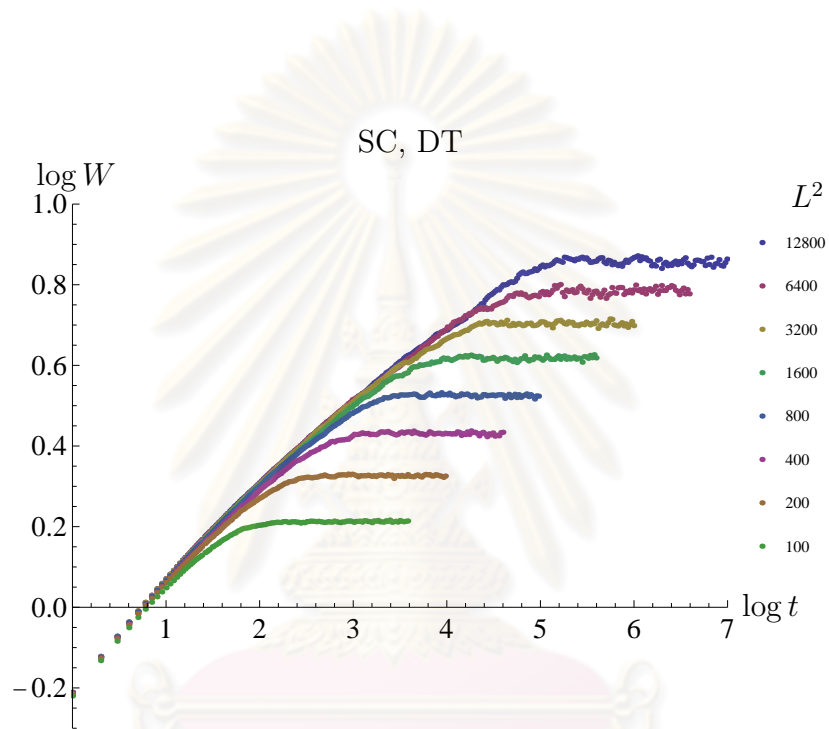


Figure A.1: The interface width as a function of time of SC structure of DT model.

ศูนย์วิทยทรัพยากร
จุฬาลงกรณ์มหาวิทยาลัย

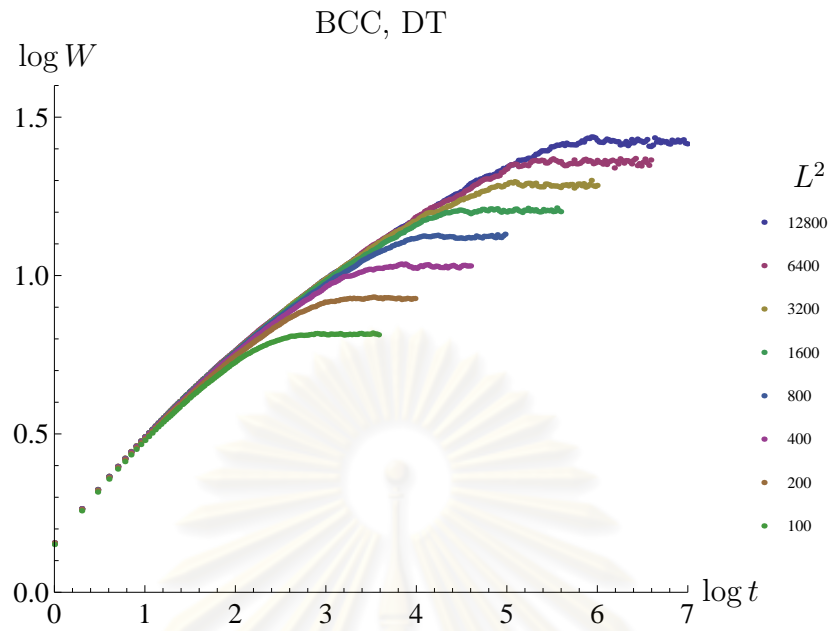


Figure A.2: The interface width as a function of time of BCC structure of DT model.

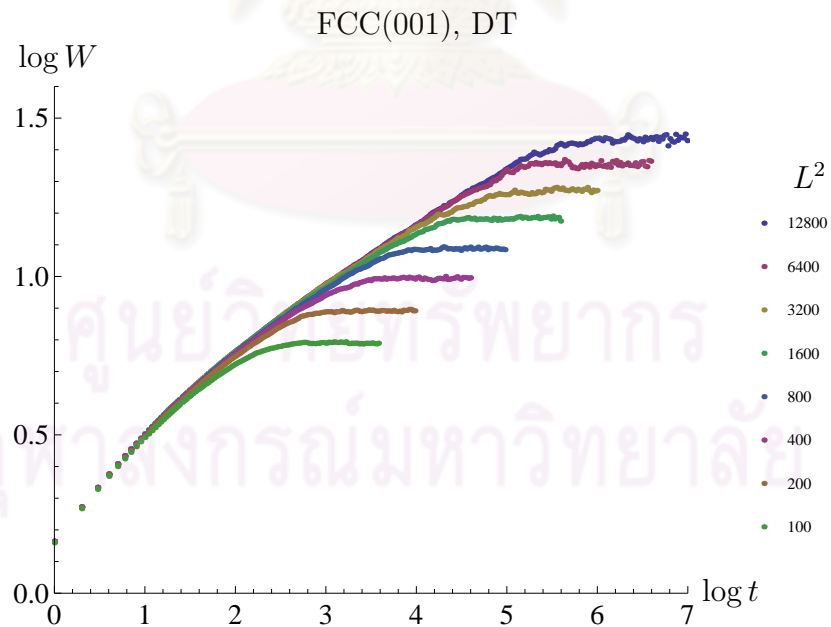


Figure A.3: The interface width as a function of time of FCC(001) structure of DT model.

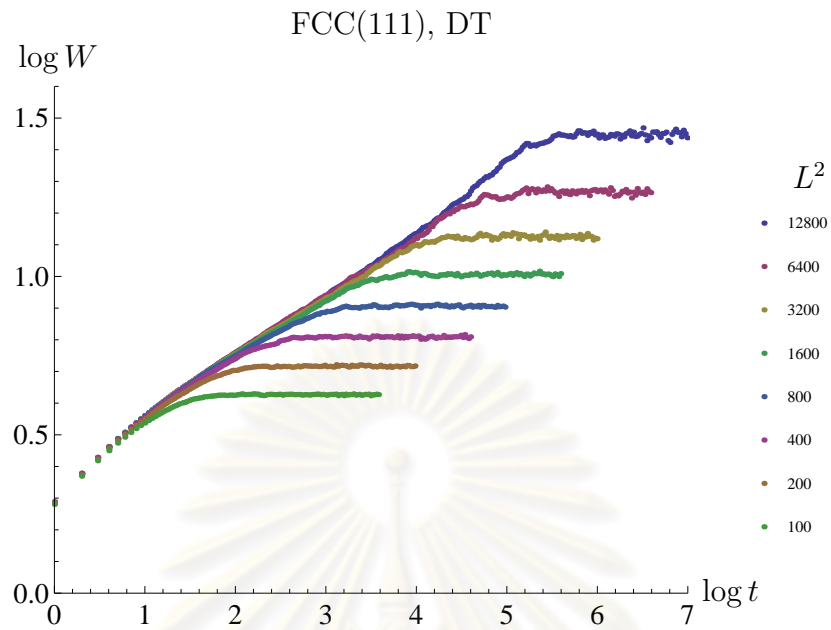


Figure A.4: The interface width as a function of time of FCC(111) structure of DT model.

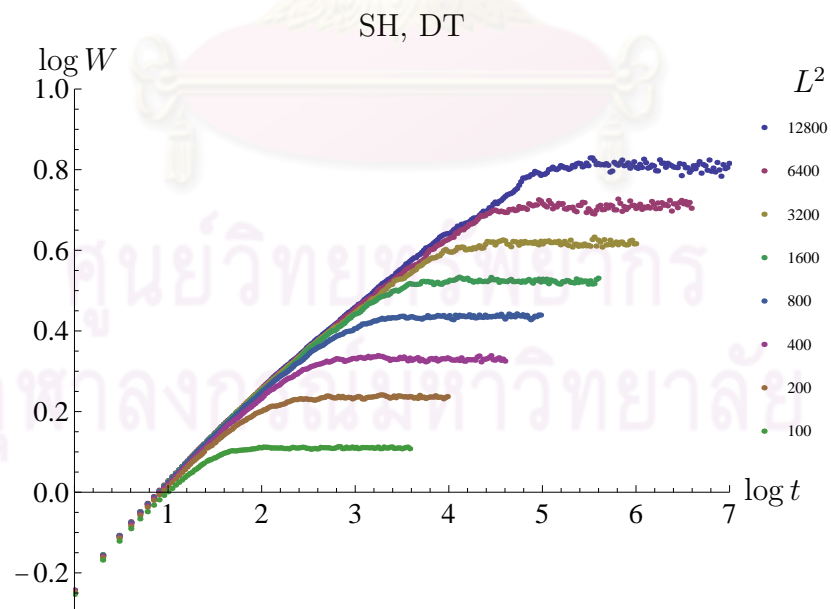


Figure A.5: The interface width as a function of time of SH structure of DT model.

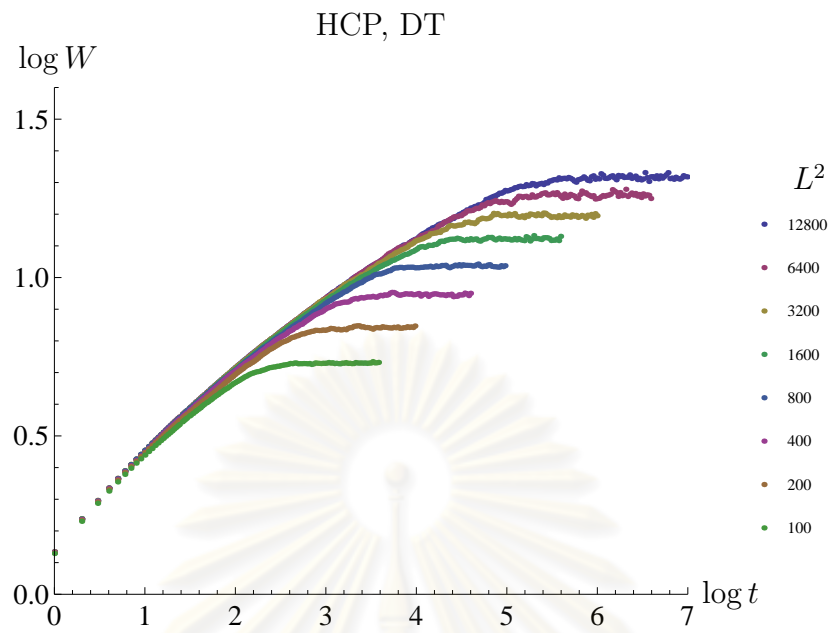


Figure A.6: The interface width as a function of time of HCP structure of DT model.

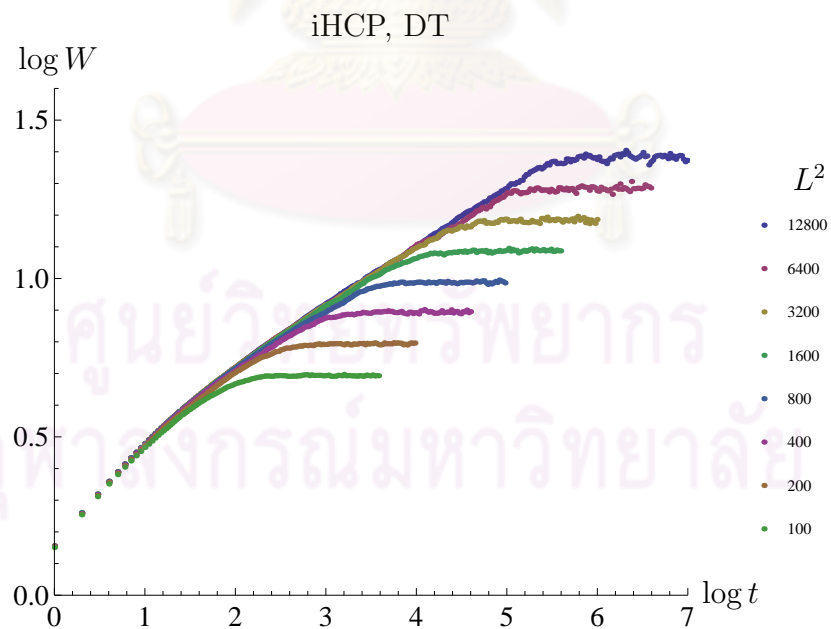


Figure A.7: The interface width as a function of time of iHCP structure of DT model.

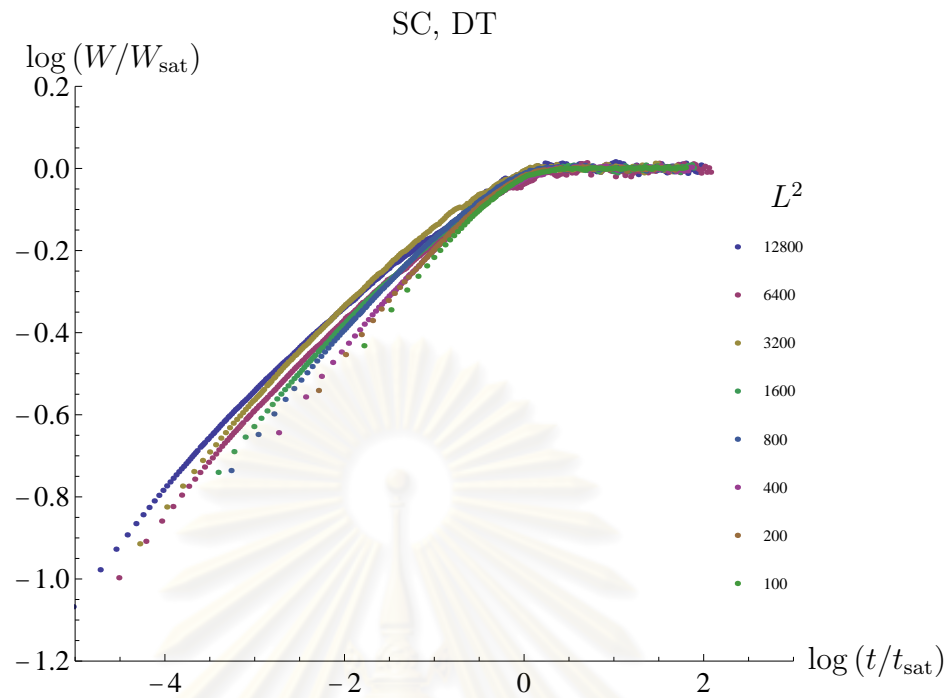


Figure A.8: The scaling collapse of the SC structure of DT model.

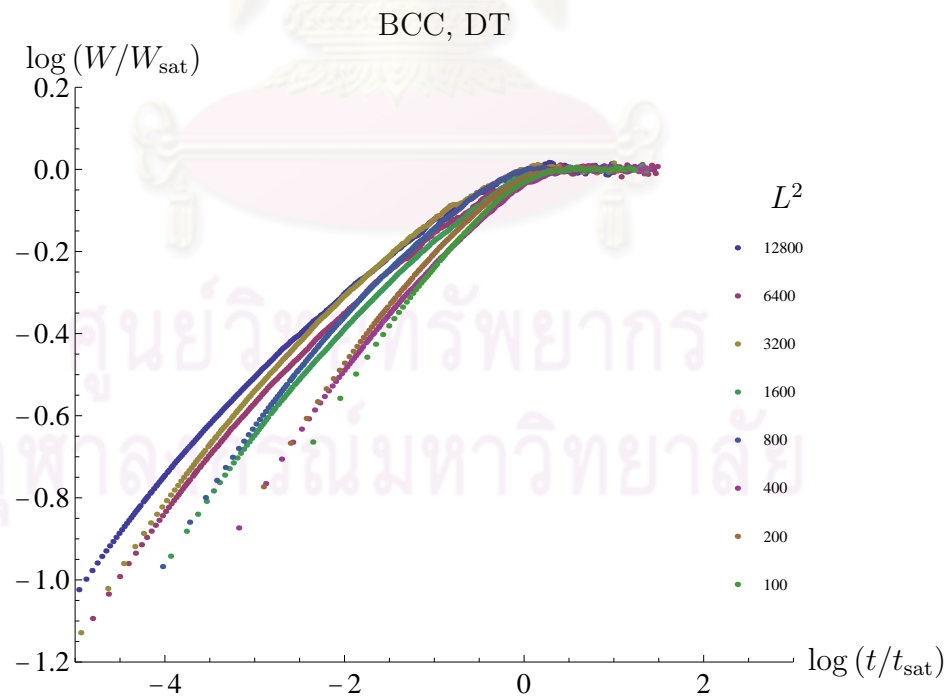


Figure A.9: The scaling collapse of the BCC structure of DT model.

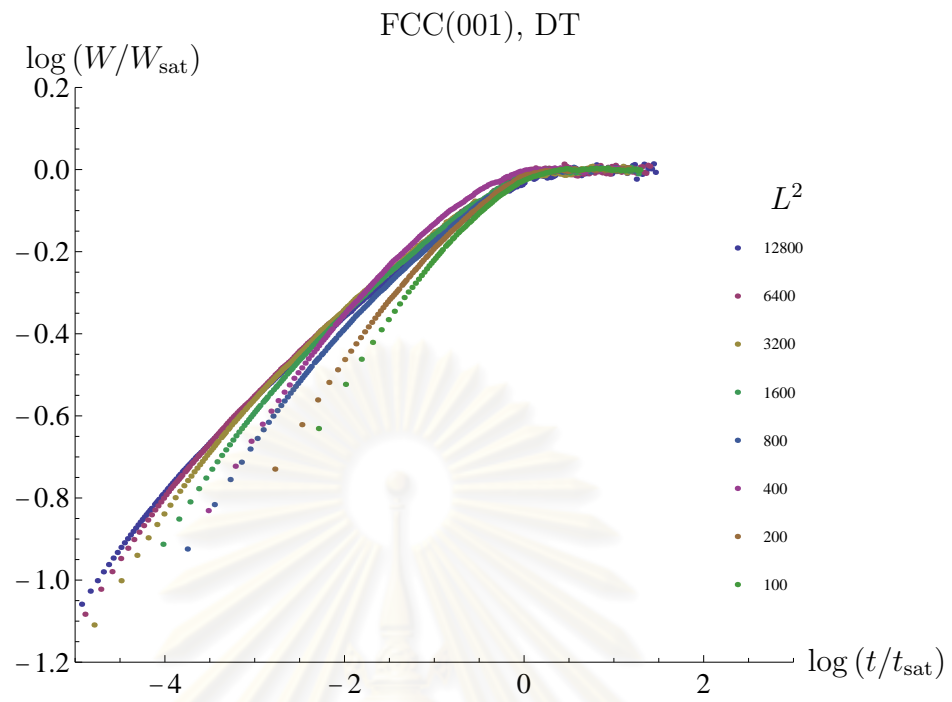


Figure A.10: The scaling collapse of the FCC(001) structure of DT model.

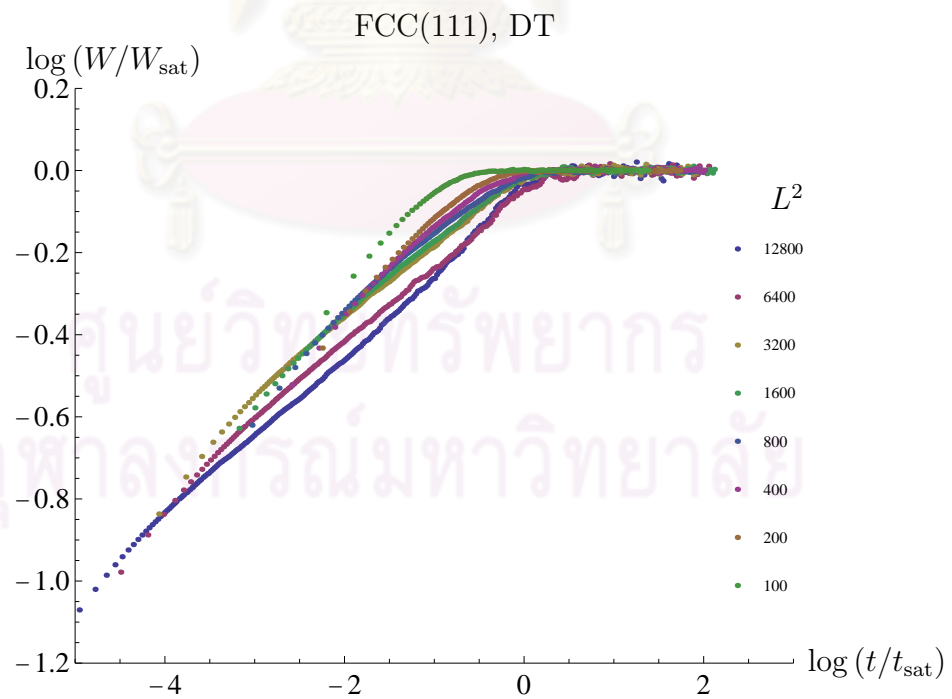


Figure A.11: The scaling collapse of the FCC(111) structure of DT model.

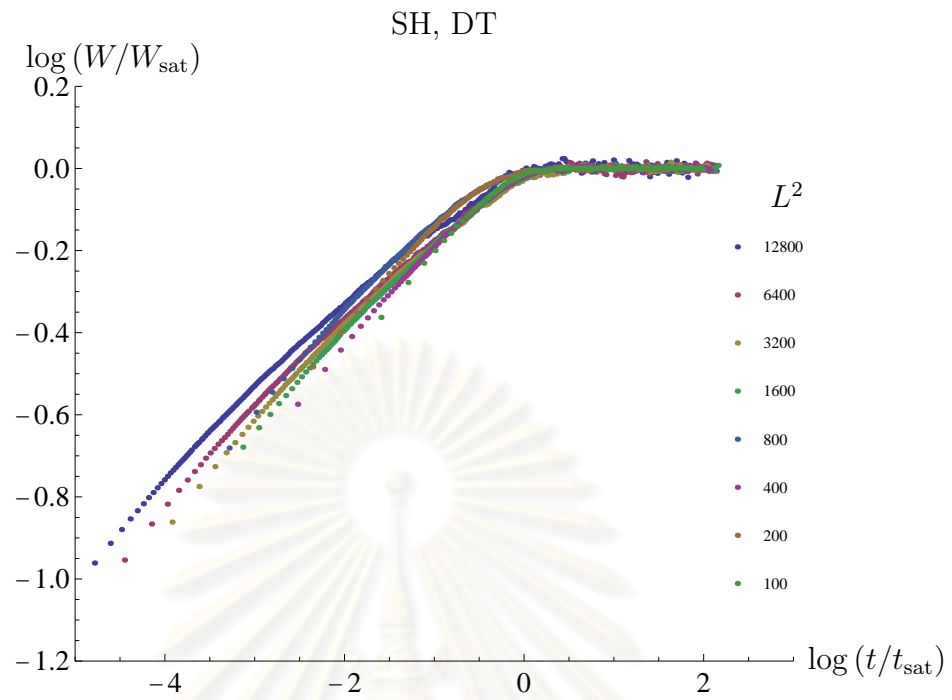


Figure A.12: The scaling collapse of the SH structure of DT model.

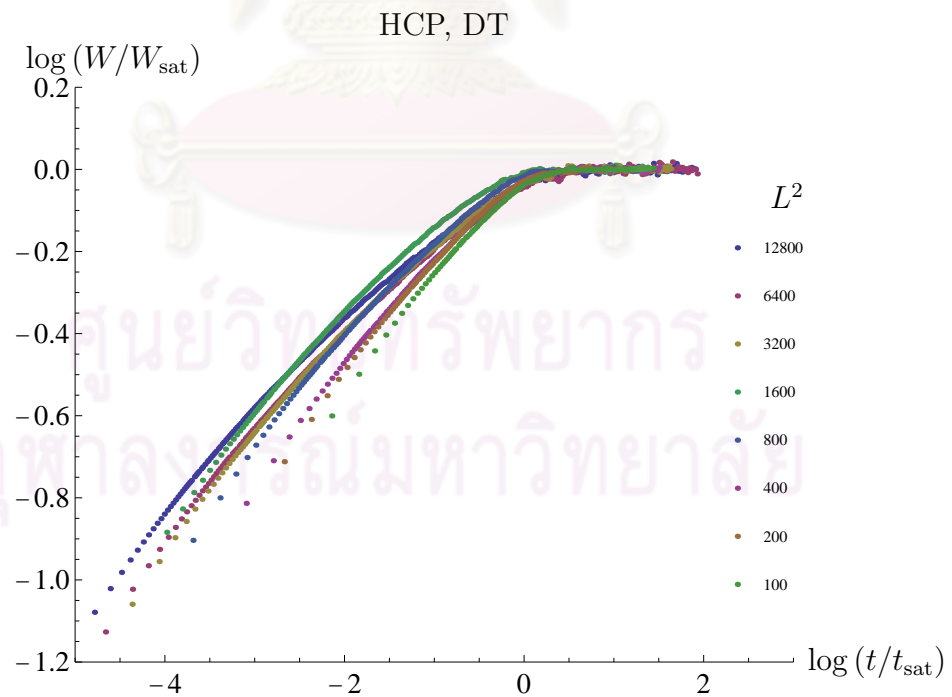


Figure A.13: The scaling collapse of the HCP structure of DT model.

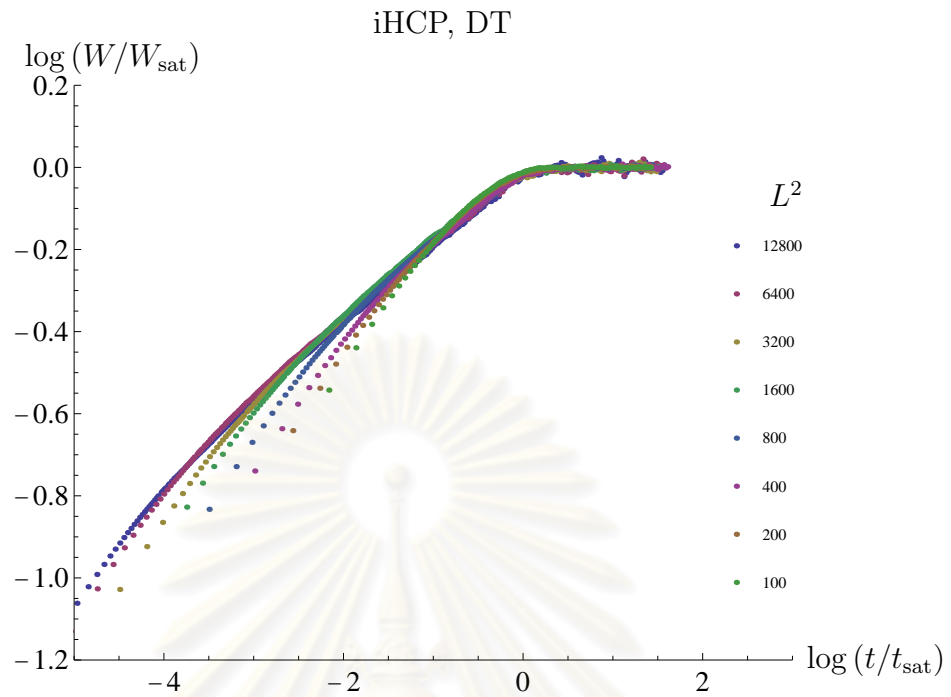


Figure A.14: The scaling collapse of the iHCP structure of DT model.

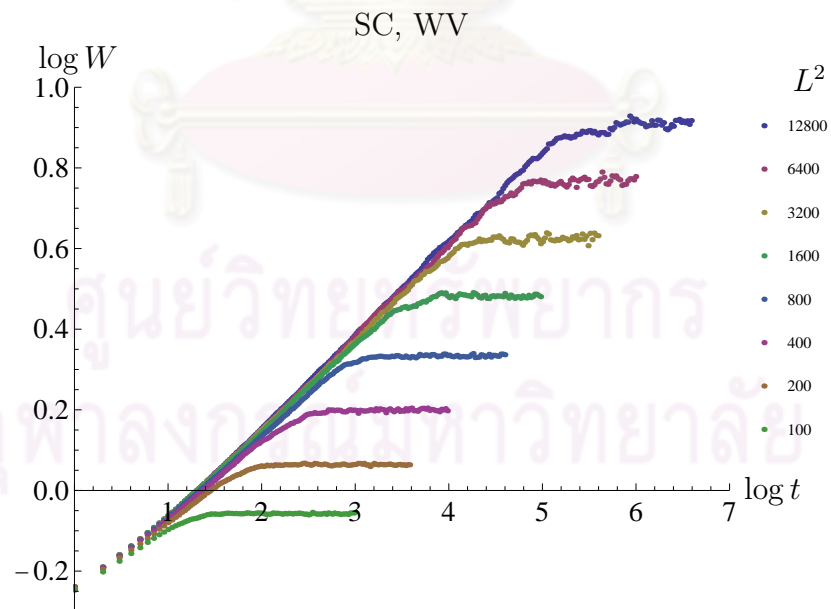


Figure A.15: The interface width as a function of time of SC structure of WV model.

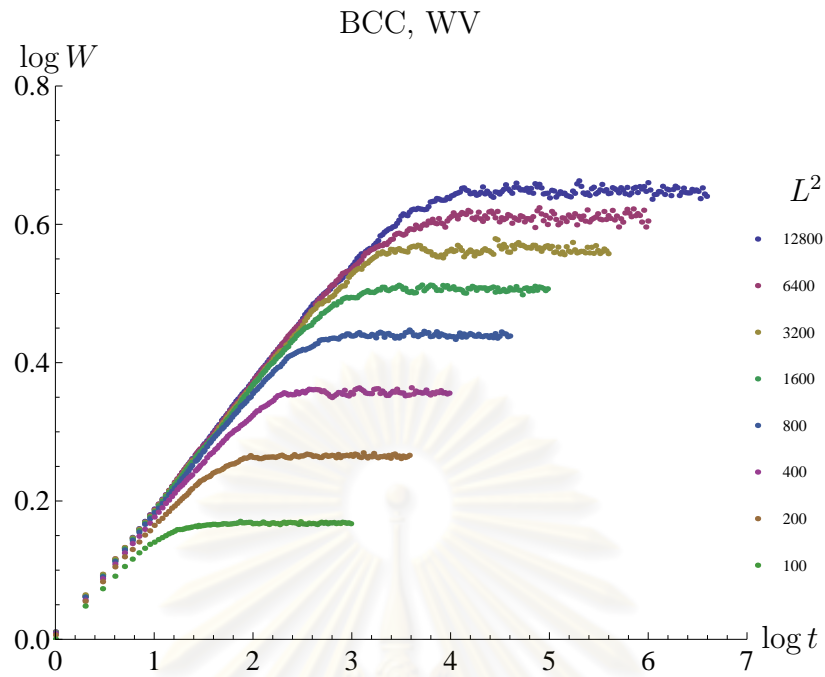


Figure A.16: The interface width as a function of time of BCC structure of WV model.

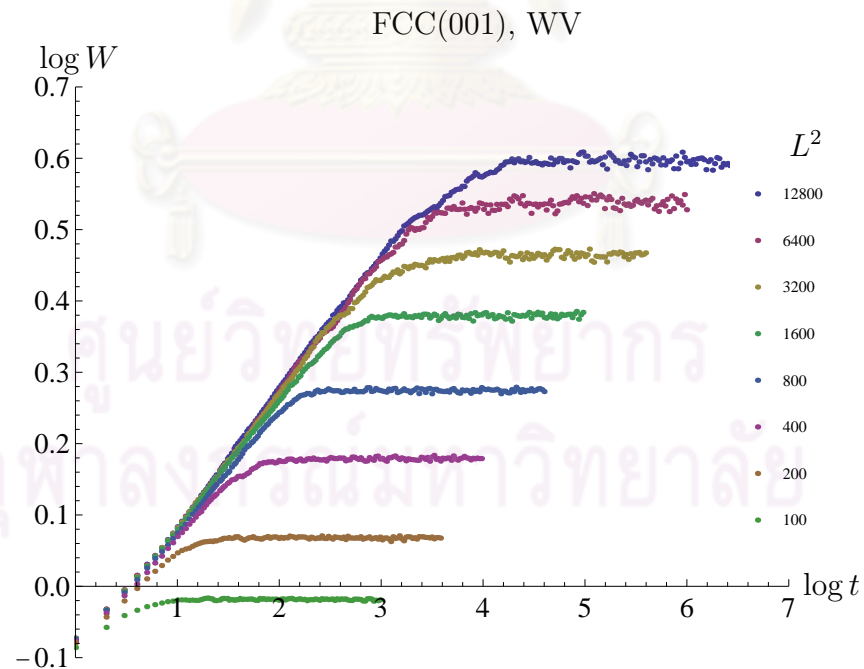


Figure A.17: The interface width as a function of time of FCC(001) structure of WV model.

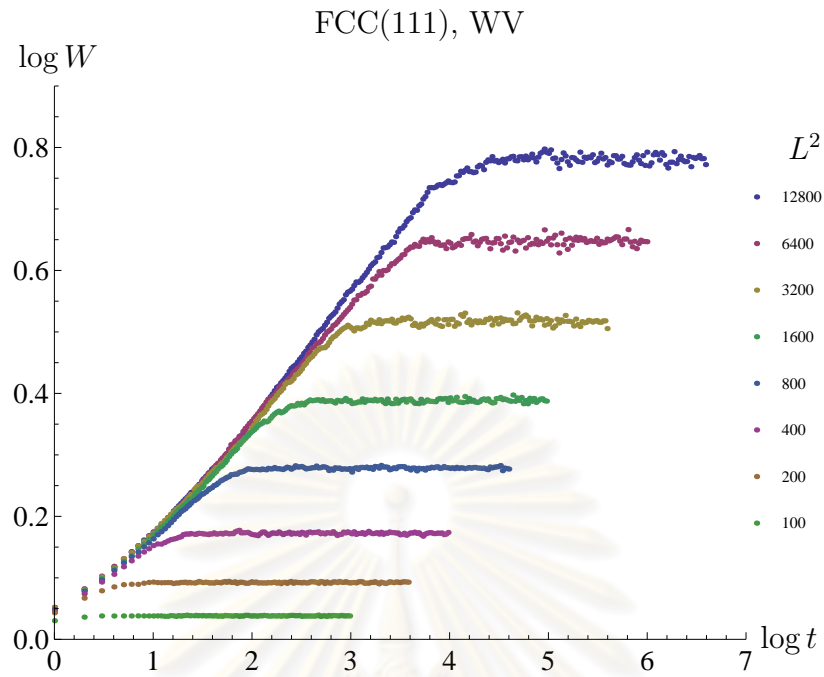


Figure A.18: The interface width as a function of time of FCC(111) structure of WV model.

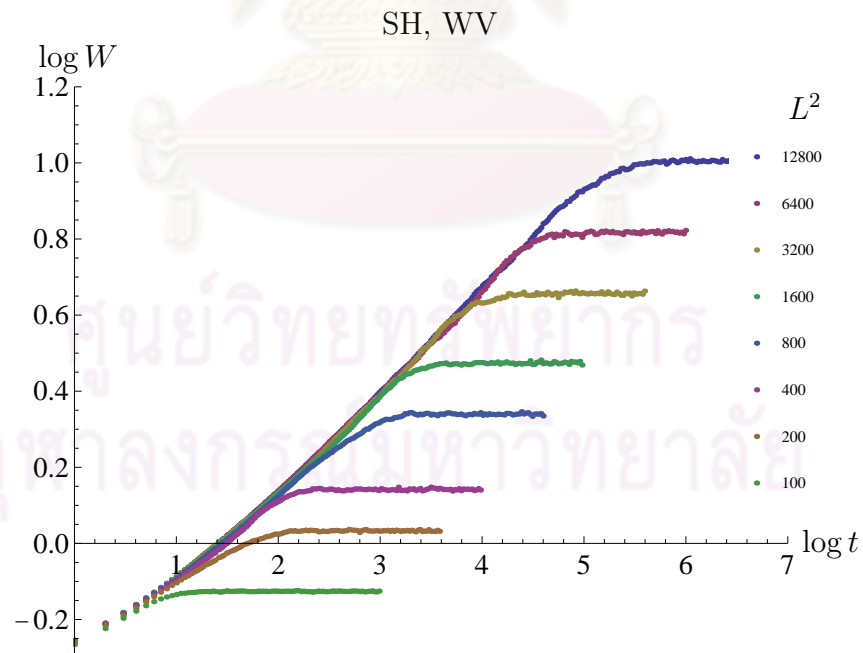


Figure A.19: The interface width as a function of time of SH structure of WV model.

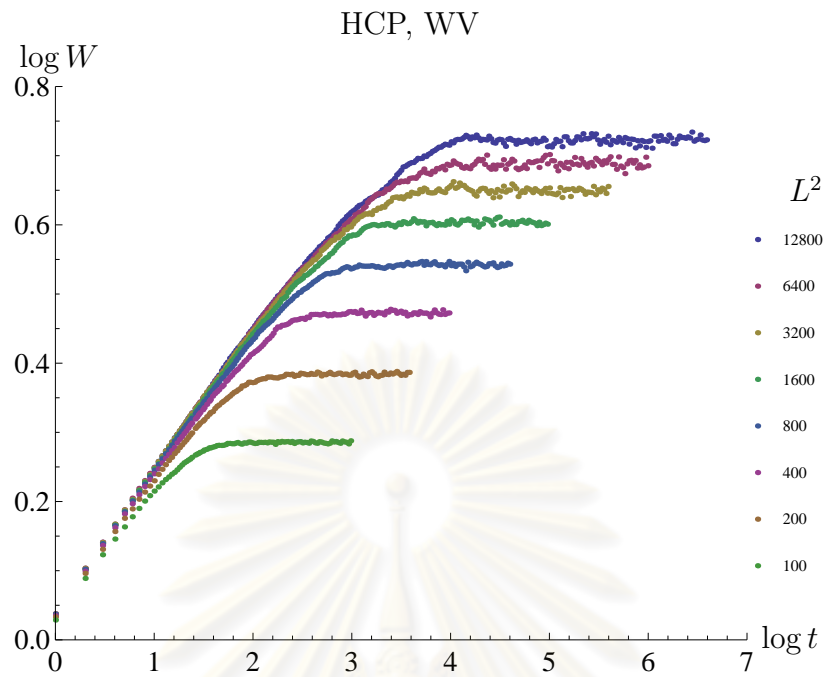


Figure A.20: The interface width as a function of time of HCP structure of WV model.

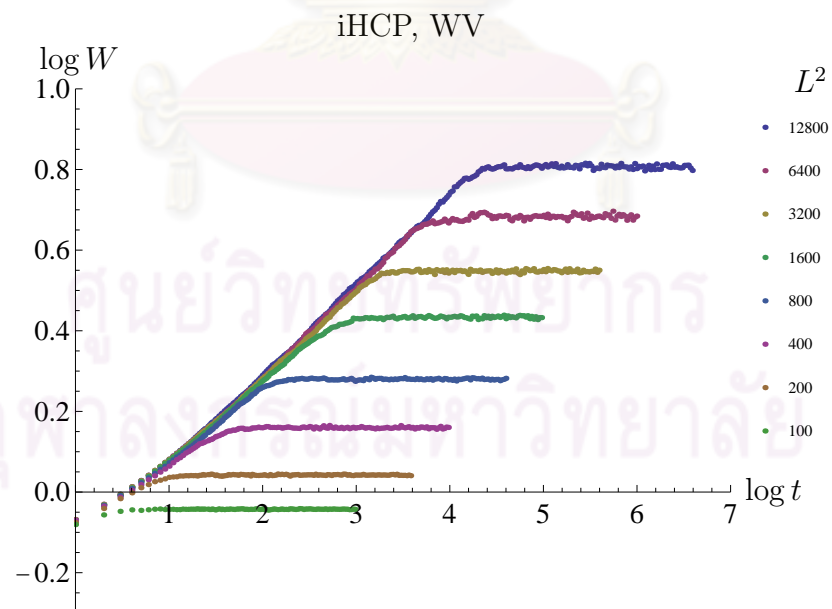


Figure A.21: The interface width as a function of time of iHCP structure of WV model.

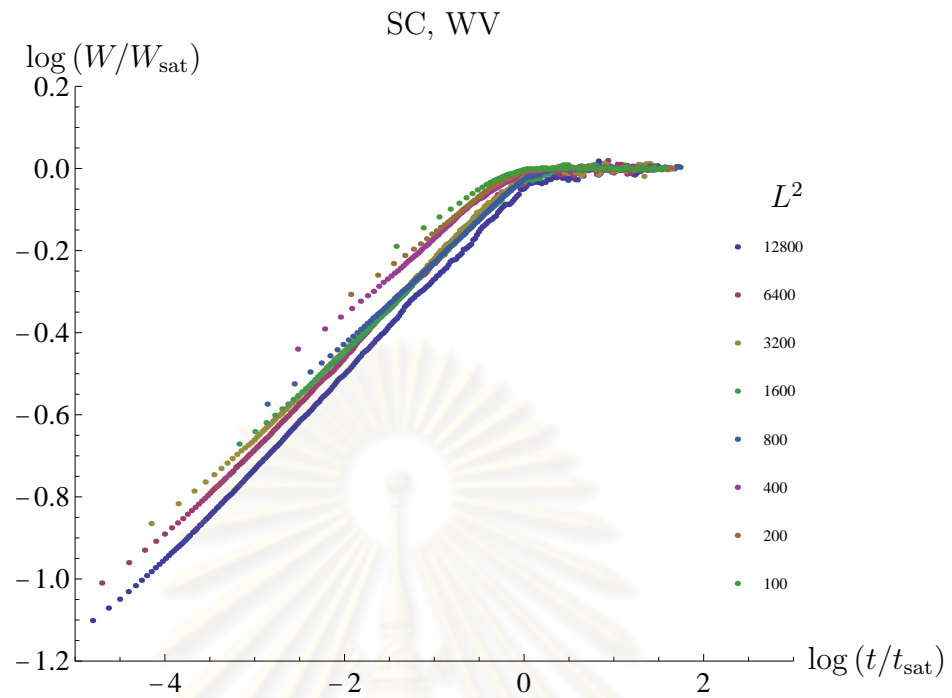


Figure A.22: The scaling collapse of the SC structure of WV model.

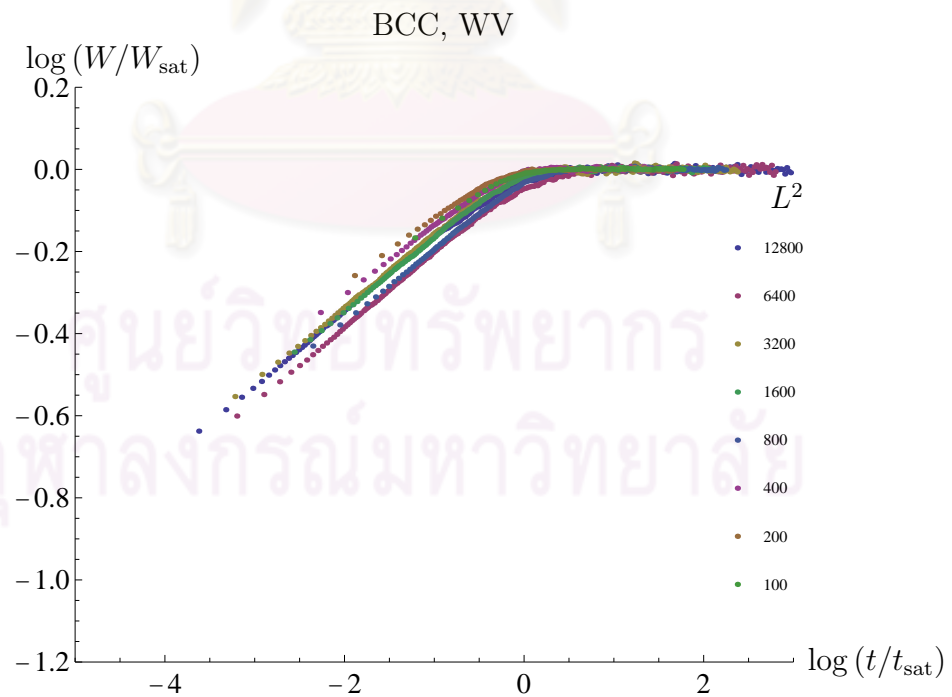


Figure A.23: The scaling collapse of the BCC structure of WV model.

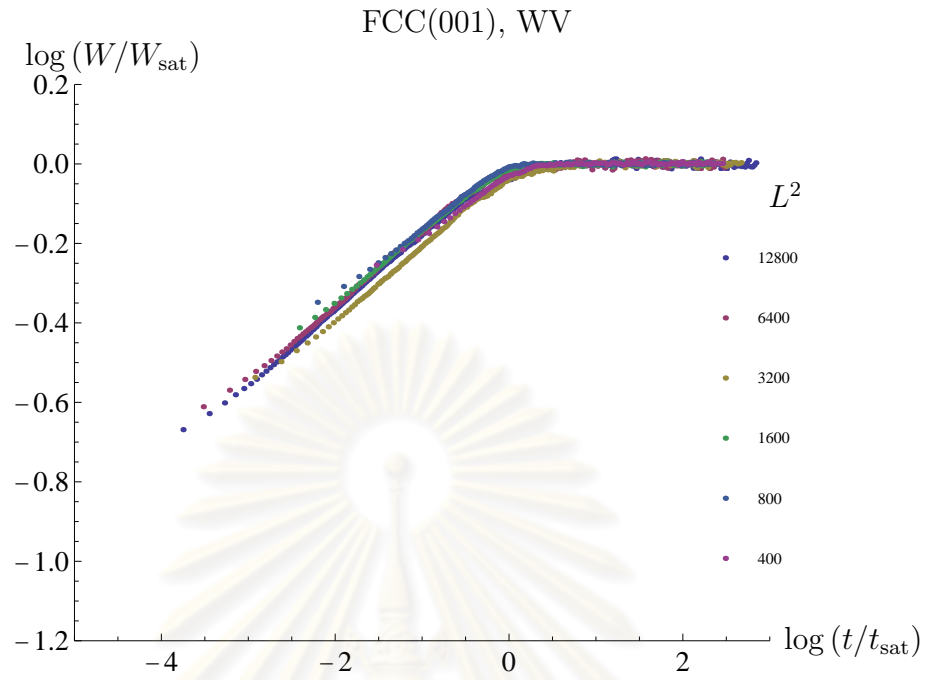


Figure A.24: The scaling collapse of the FCC(001) structure of WV model.

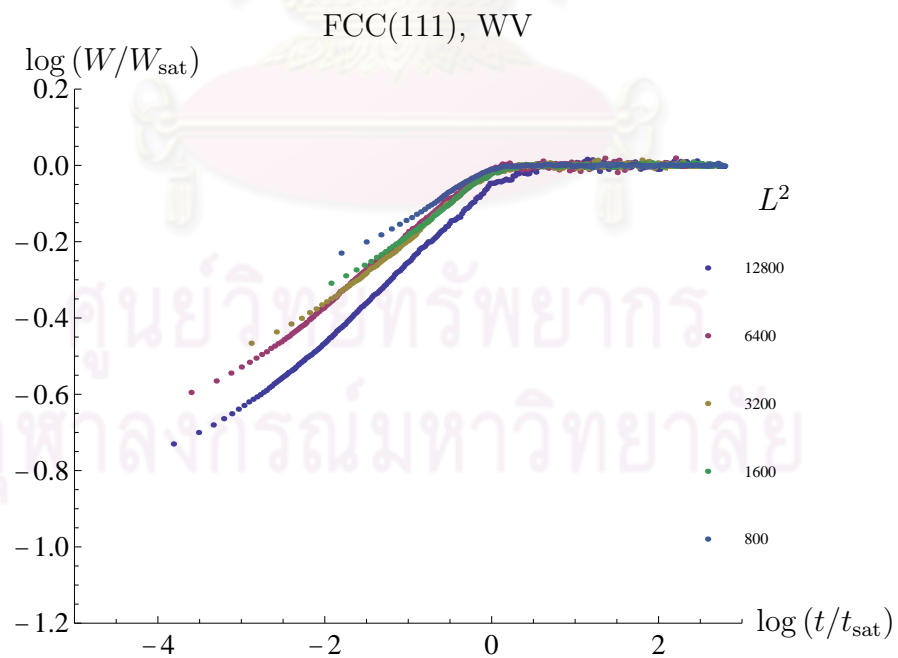


Figure A.25: The scaling collapse of the FCC(111) structure of WV model.

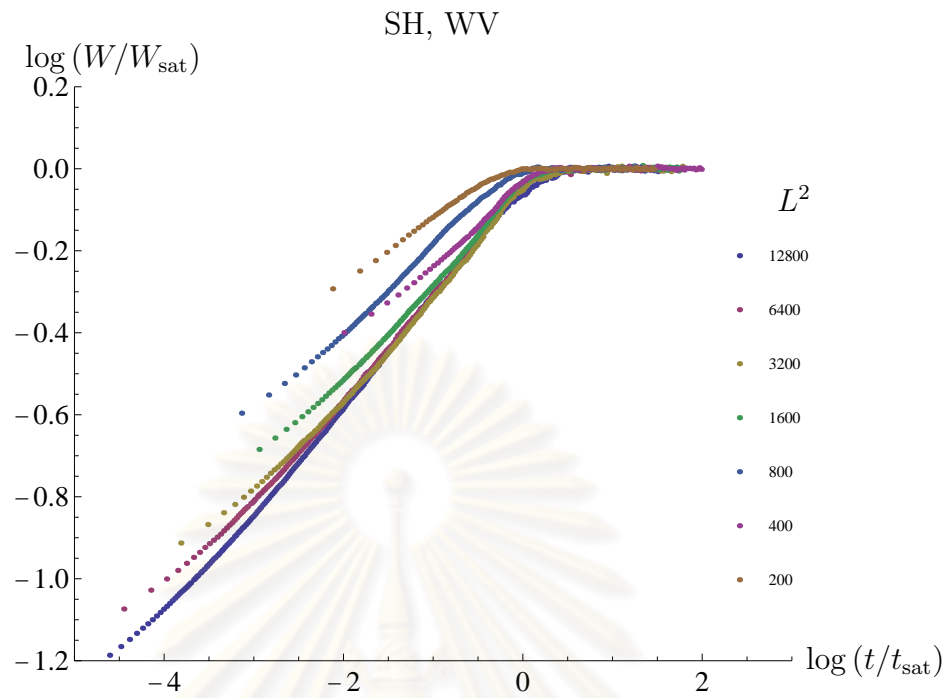


Figure A.26: The scaling collapse of the SH structure of WV model.

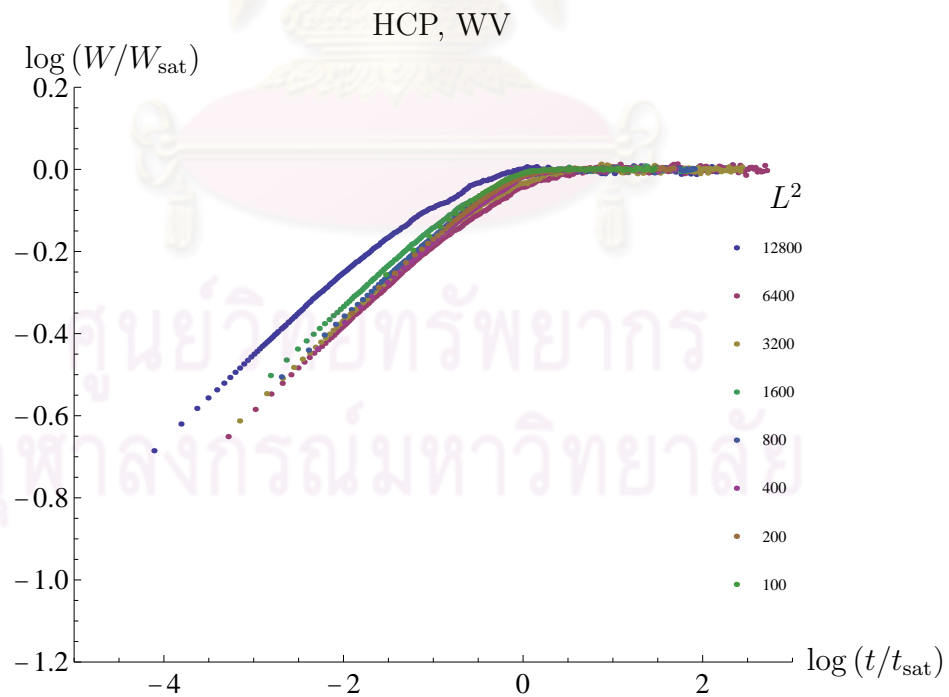


Figure A.27: The scaling collapse of the HCP structure of WV model.

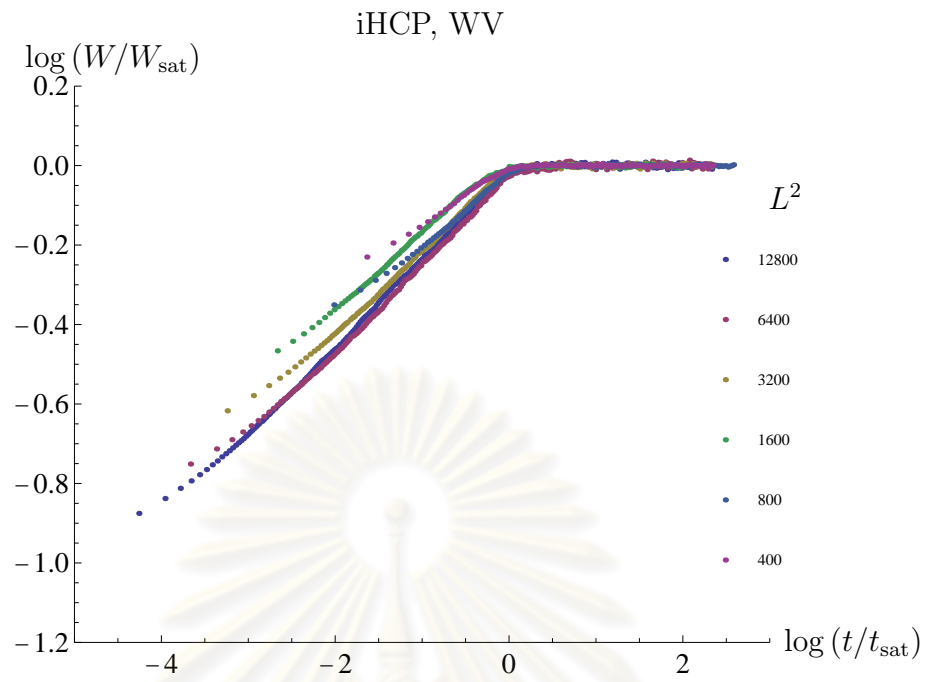


Figure A.28: The scaling collapse of the iHCP structure of WV model.

ศูนย์วิทยทรัพยากร
จุฬาลงกรณ์มหาวิทยาลัย

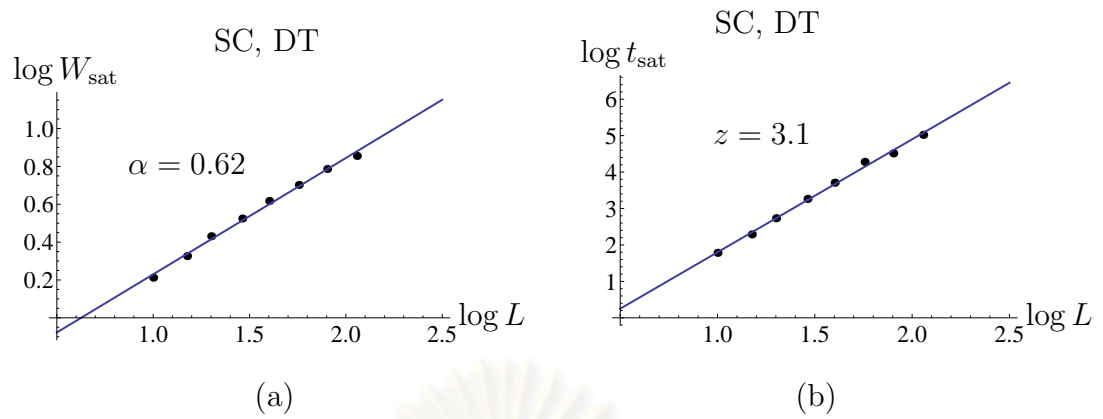


Figure A.29: The roughness and dynamical exponents α and z of SC structure of DT model.

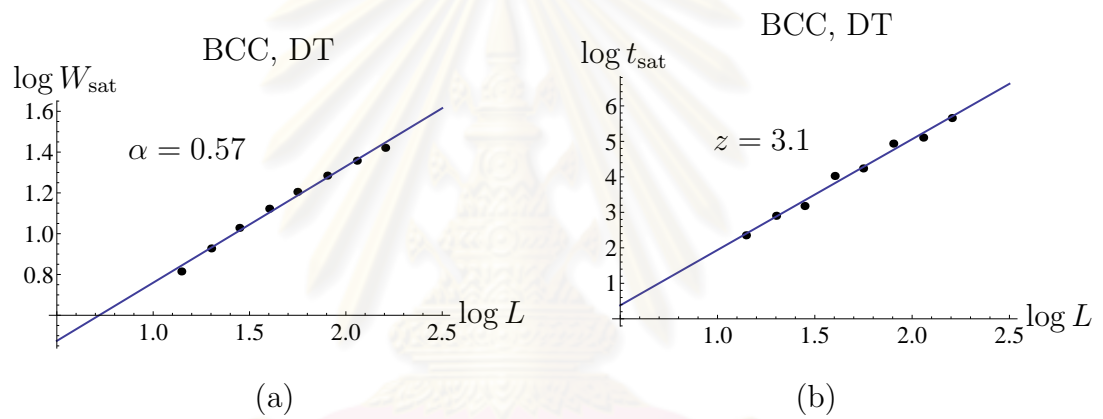


Figure A.30: The roughness and dynamical exponents α and z of BCC structure of DT model.

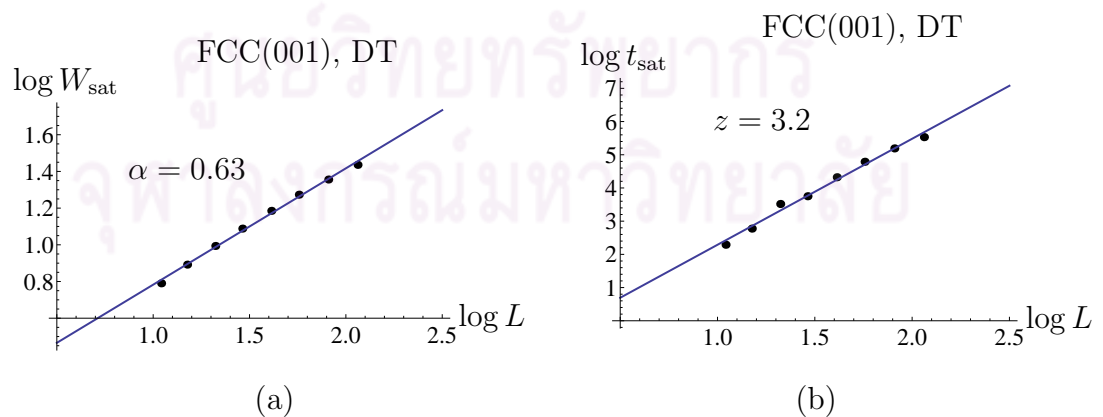


Figure A.31: The roughness and dynamical exponents α and z of FCC structure of DT model.

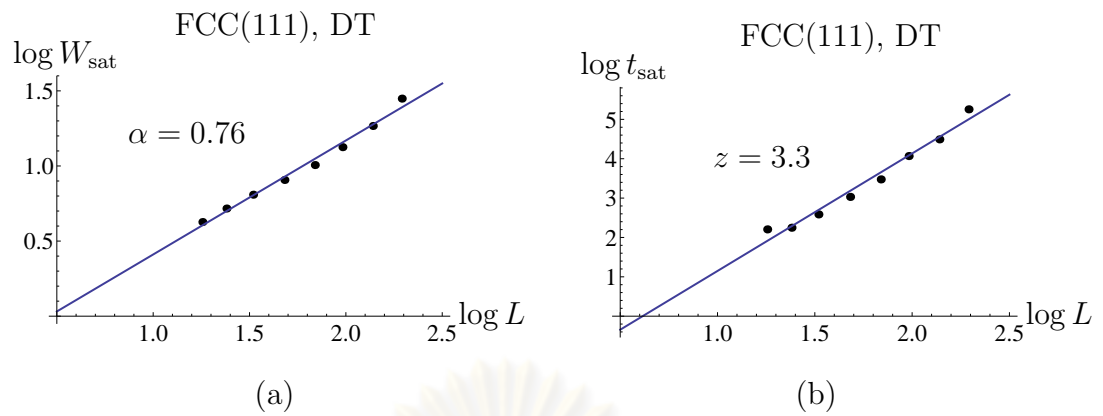


Figure A.32: The roughness and dynamical exponents α and z of FCC(111) structure of DT model.

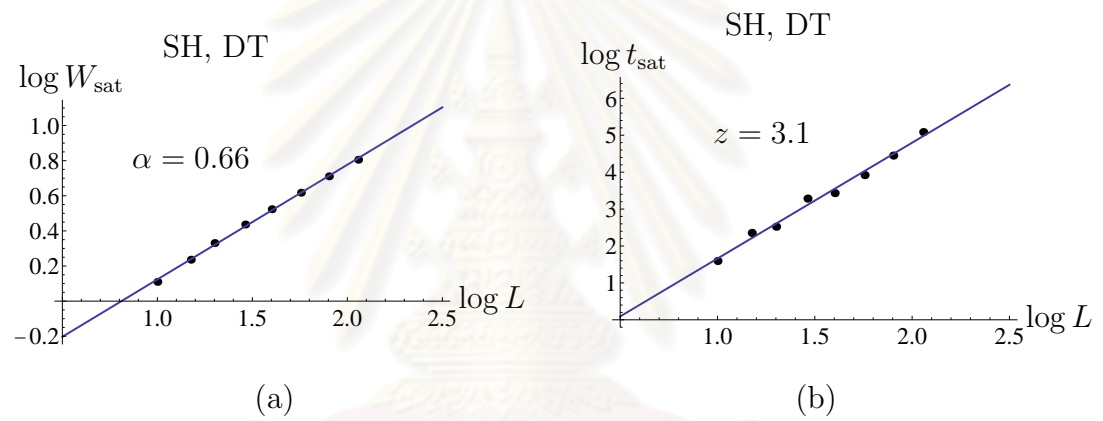


Figure A.33: The roughness and dynamical exponents α and z of SH structure of DT model.

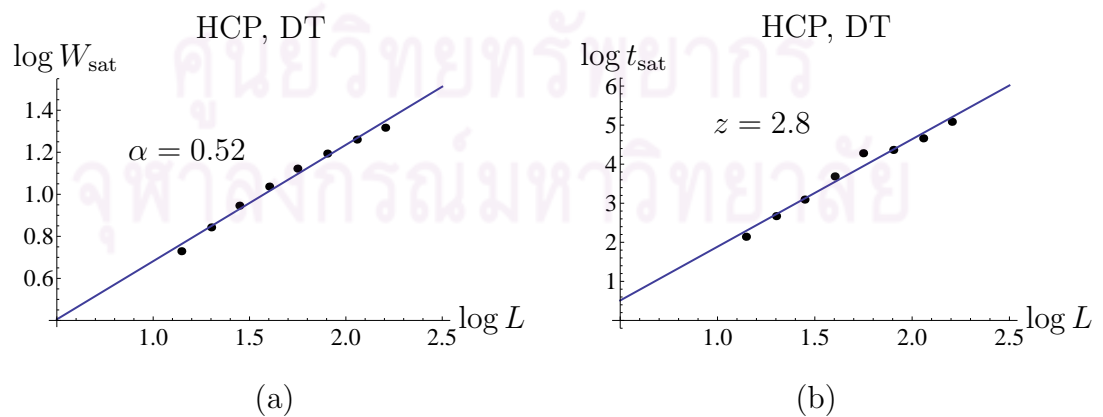


Figure A.34: The roughness and dynamical exponents α and z of HCP structure of DT model.

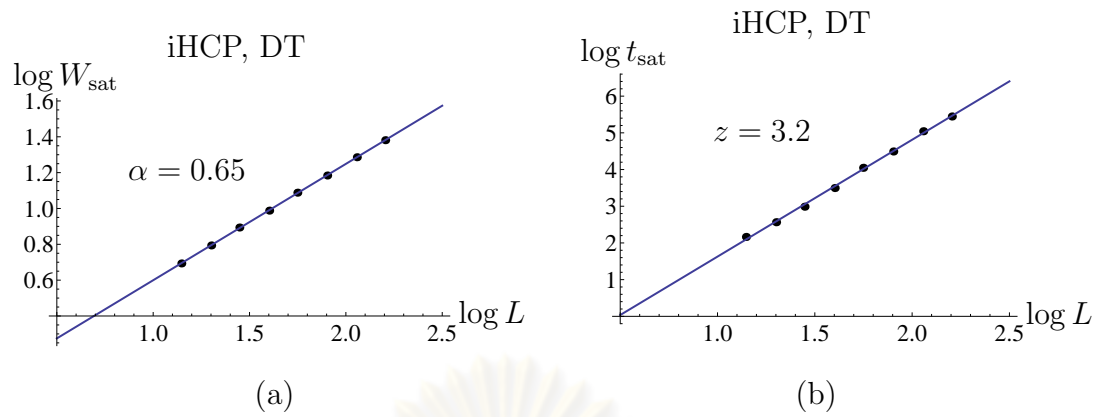


Figure A.35: The roughness and dynamical exponents α and z of iHCP structure of DT model.

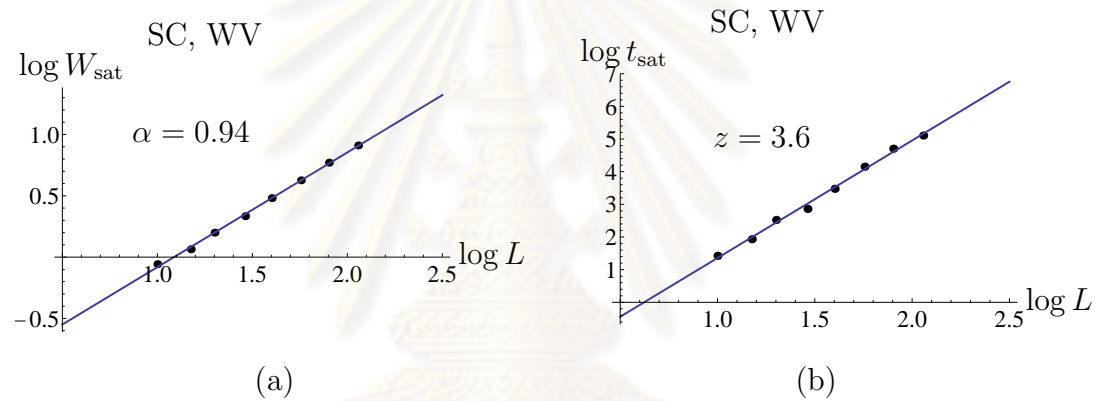


Figure A.36: The roughness and dynamical exponents α and z of SC structure of WV model.

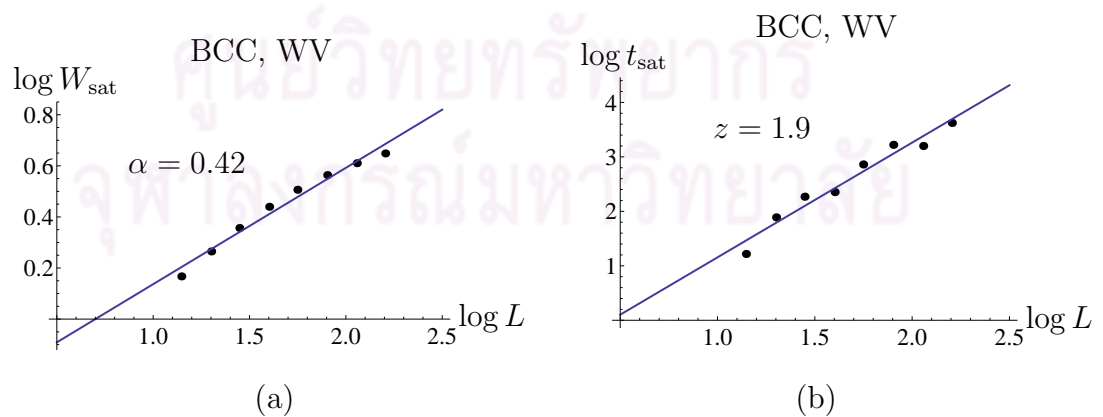


Figure A.37: The roughness and dynamical exponents α and z of BCC structure of WV model.

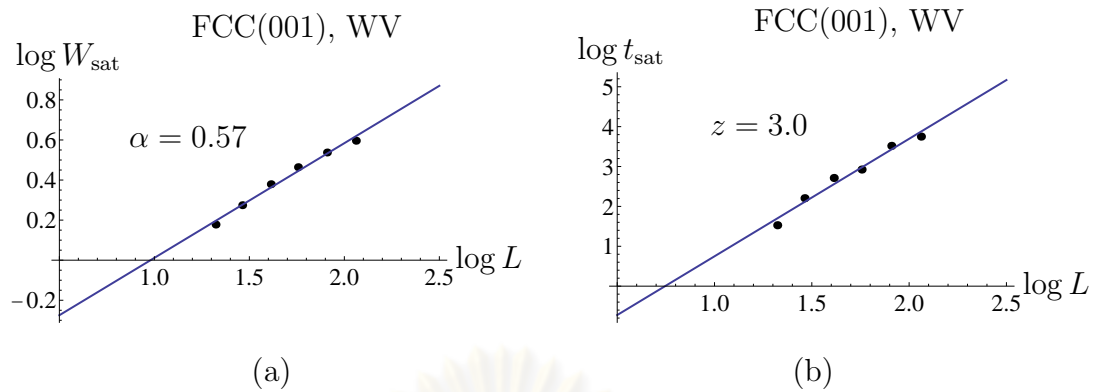


Figure A.38: The roughness and dynamical exponents α and z of FCC structure of WV model.

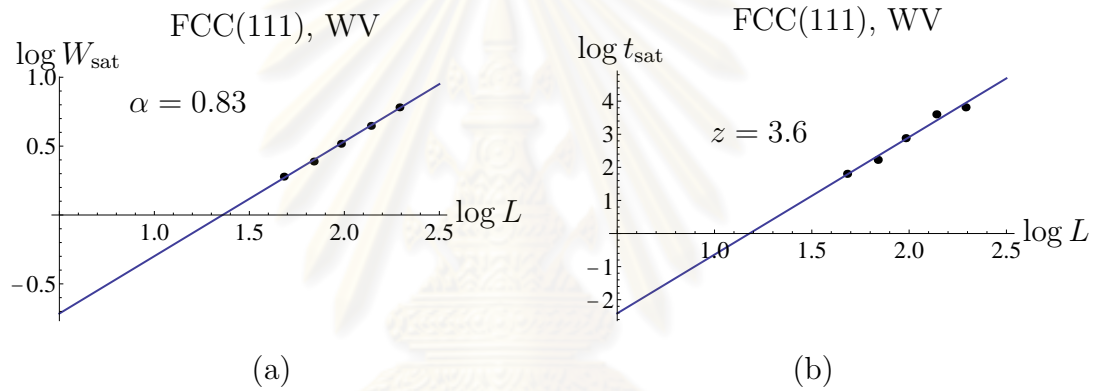


Figure A.39: The roughness and dynamical exponents α and z of FCC(111) structure of WV model.

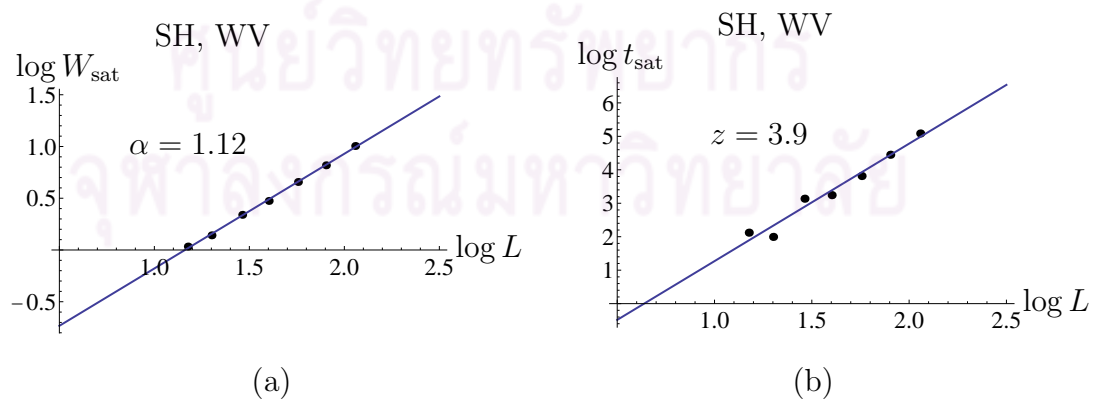


Figure A.40: The roughness and dynamical exponents α and z of SH structure of WV model.

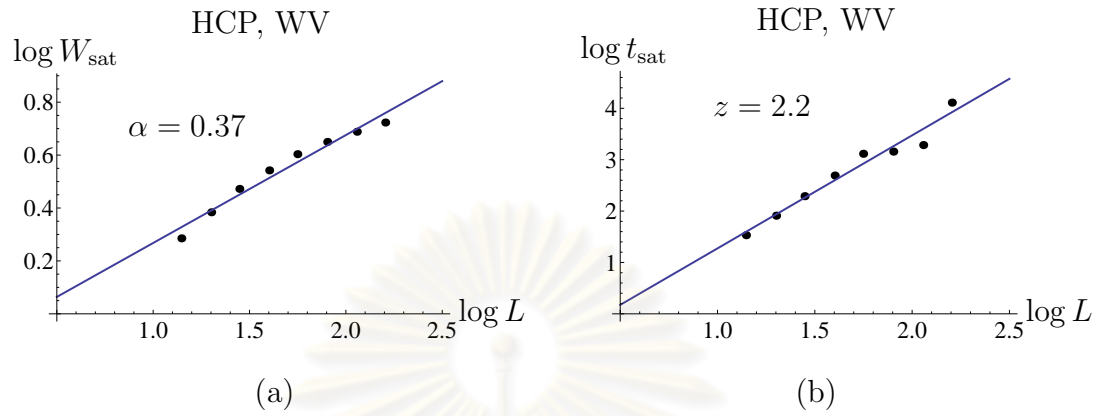


Figure A.41: The roughness and dynamical exponents α and z of HCP structure of WV model.

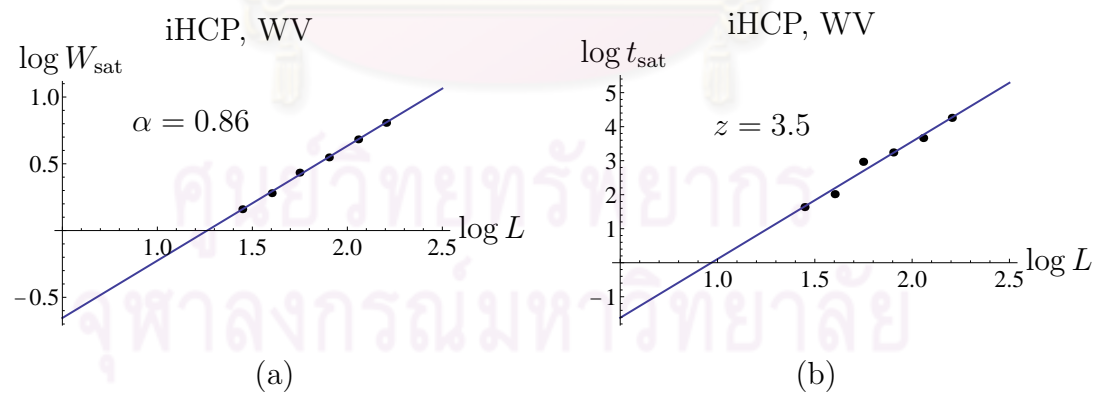


Figure A.42: The roughness and dynamical exponents α and z of iHCP structure of WV model.

Appendix B

The plots of surface morphologies and the correlation functions

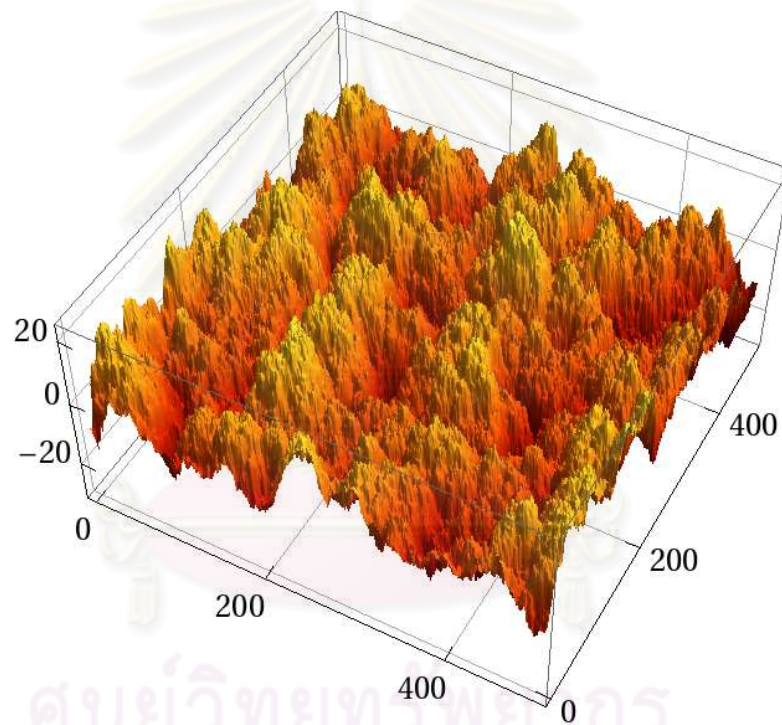


Figure B.1: Surface morphology of the SC structure of WV model at $t = 10^5$ UL.

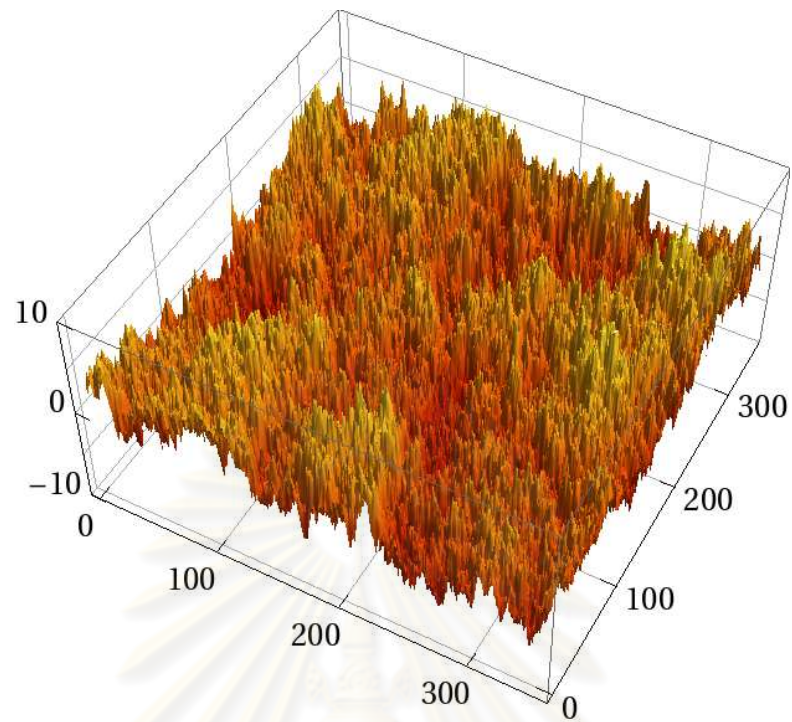


Figure B.2: Surface morphology of the BCC structure of WV model at $t = 10^5$ UL.

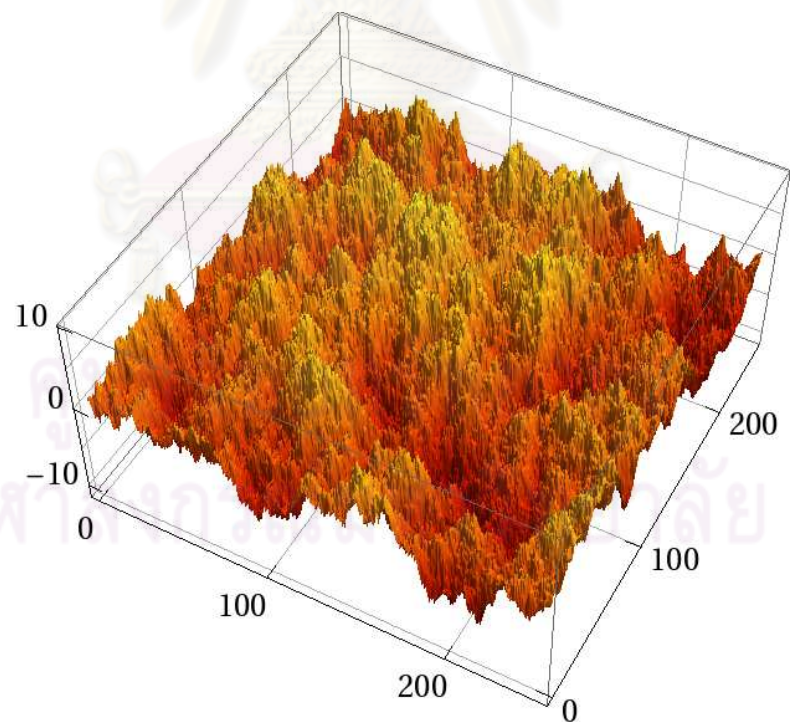


Figure B.3: Surface morphology of the FCC(001) structure of WV model at $t = 10^5$ UL.

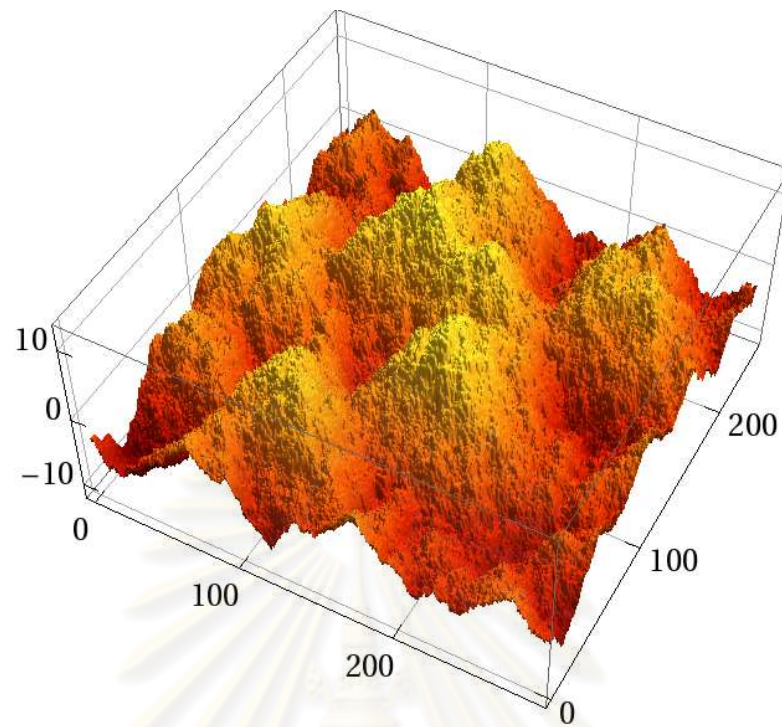


Figure B.4: Surface morphology of the FCC(111) structure of WV model at $t = 10^5$ UL.

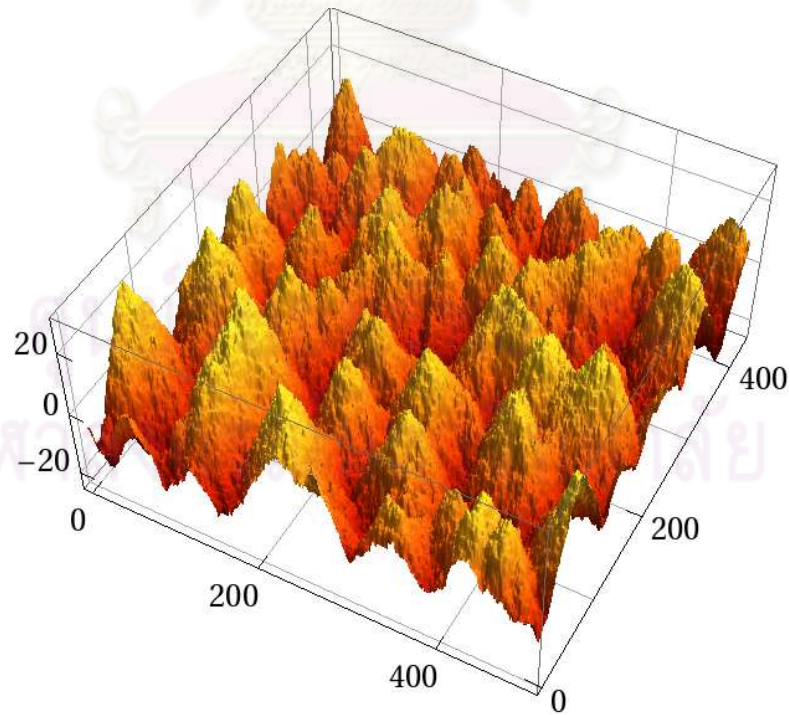


Figure B.5: Surface morphology of the SH structure of WV model at $t = 10^5$ UL.

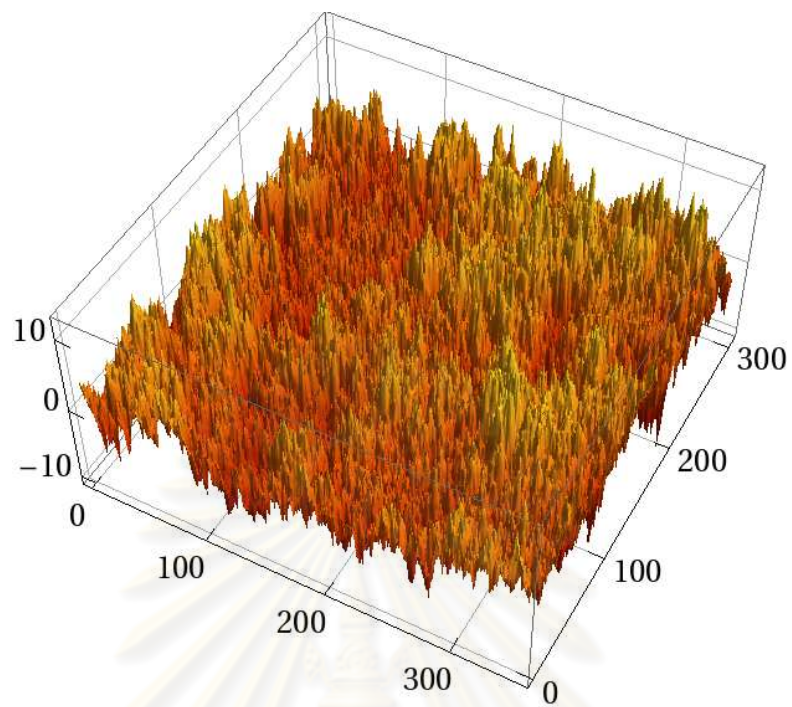


Figure B.6: Surface morphology of the HCP structure of WV model at $t = 10^5$ UL.

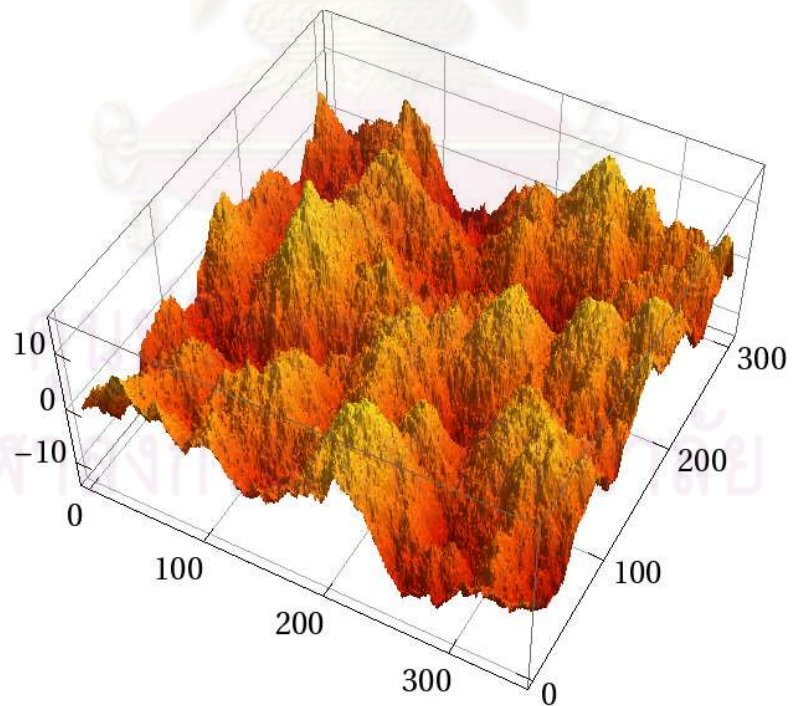


Figure B.7: Surface morphology of the iHCP structure of WV model at $t = 10^5$ UL.

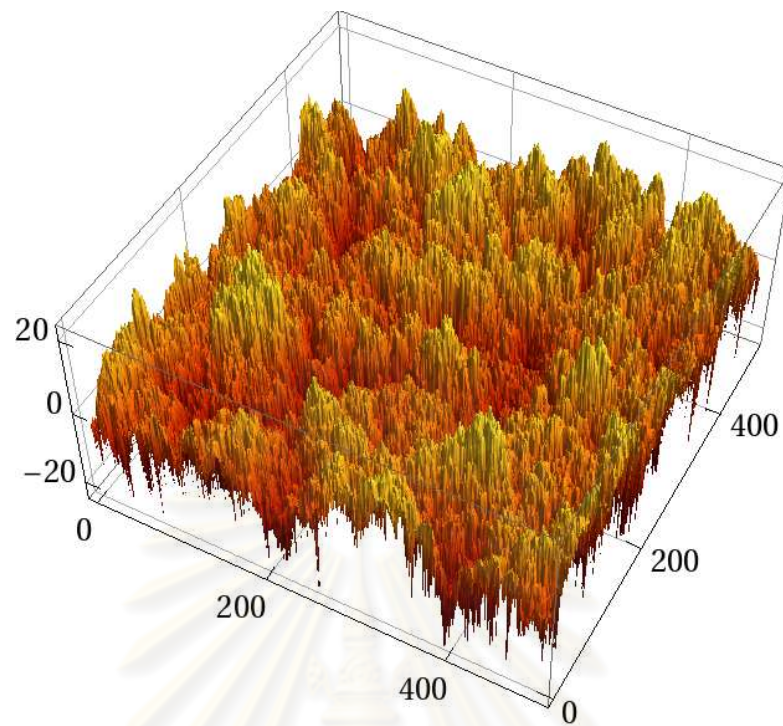


Figure B.8: Surface morphology of the SC structure of DT model at $t = 10^5$ UL.

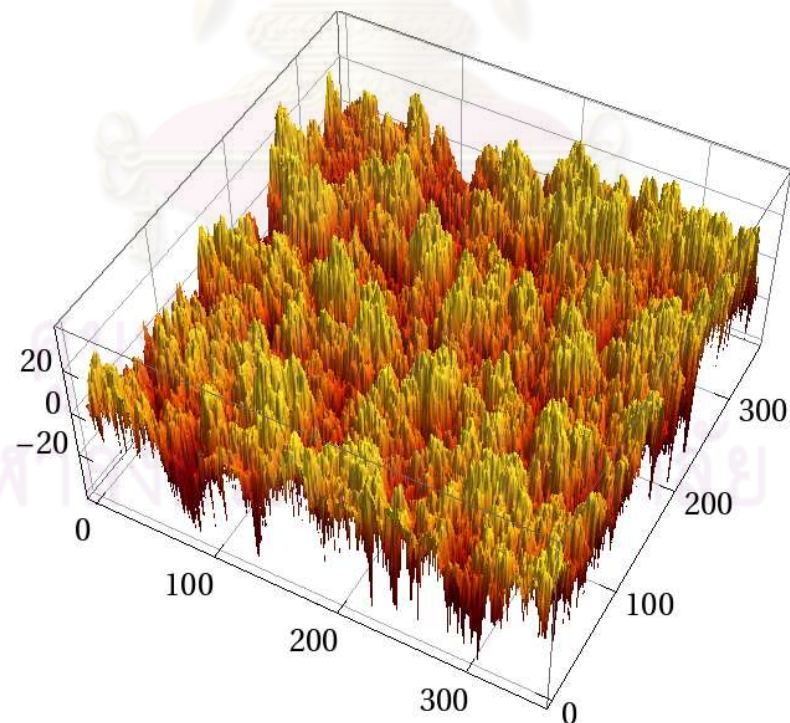


Figure B.9: Surface morphology of the BCC structure of DT model at $t = 10^5$ UL.

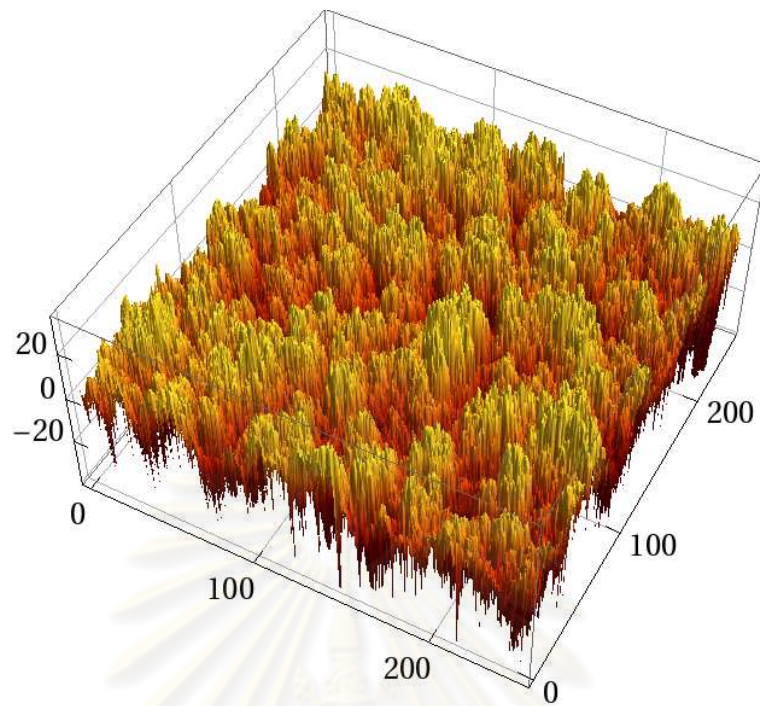


Figure B.10: Surface morphology of the FCC(001) structure of DT model at $t = 10^5$ UL.

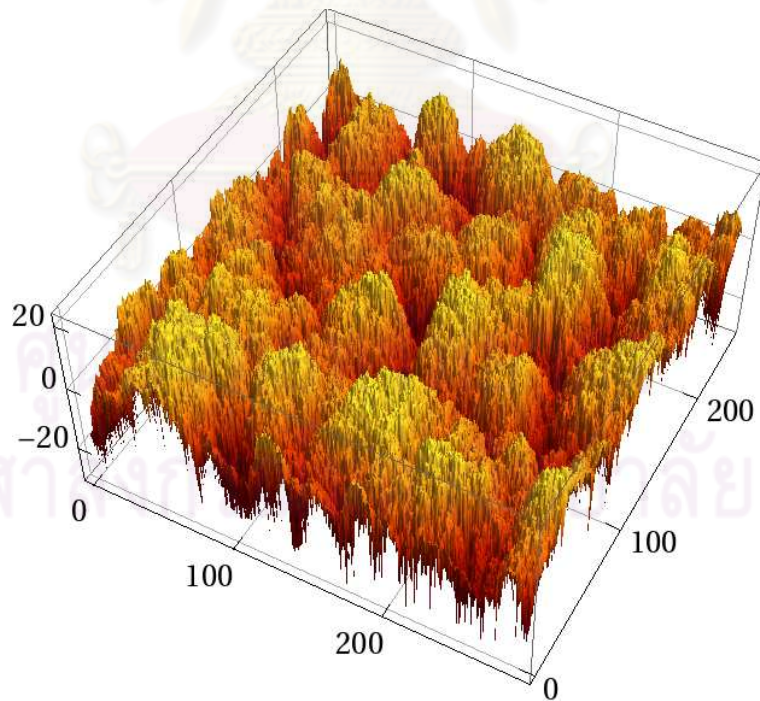


Figure B.11: Surface morphology of the FCC(111) structure of DT model at $t = 10^5$ UL.

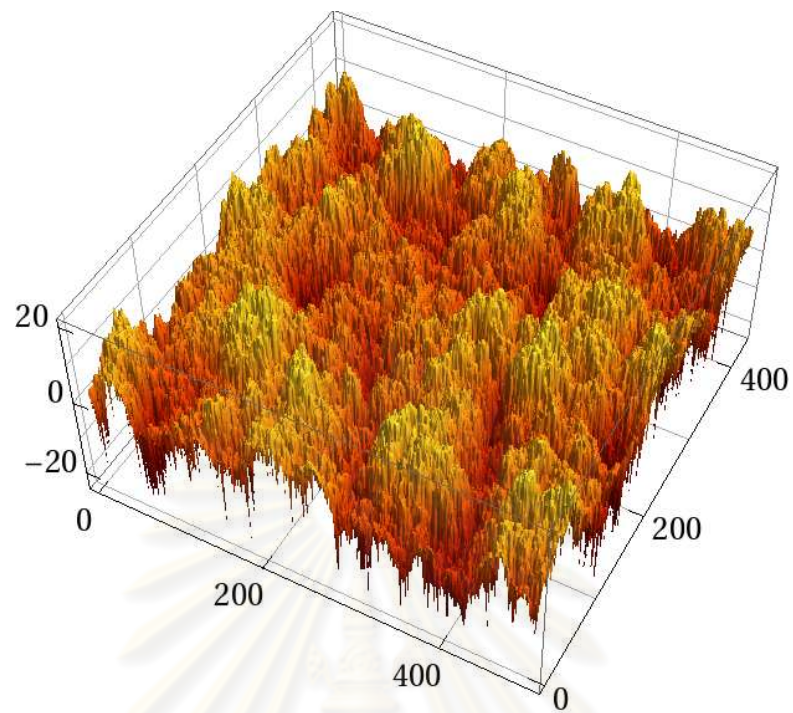


Figure B.12: Surface morphology of the SH structure of DT model at $t = 10^5$ UL.

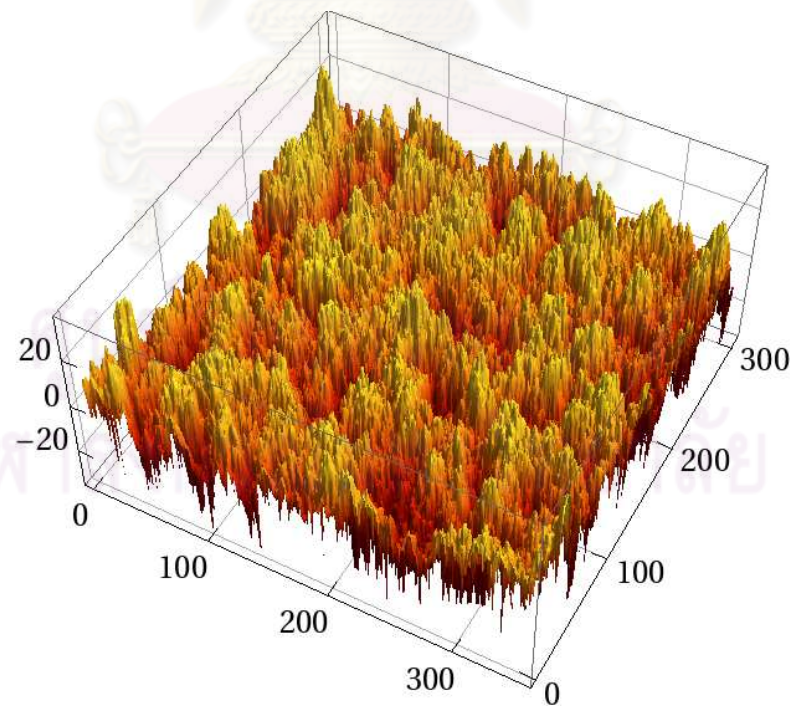


Figure B.13: Surface morphology of the HCP structure of DT model at $t = 10^5$ UL.

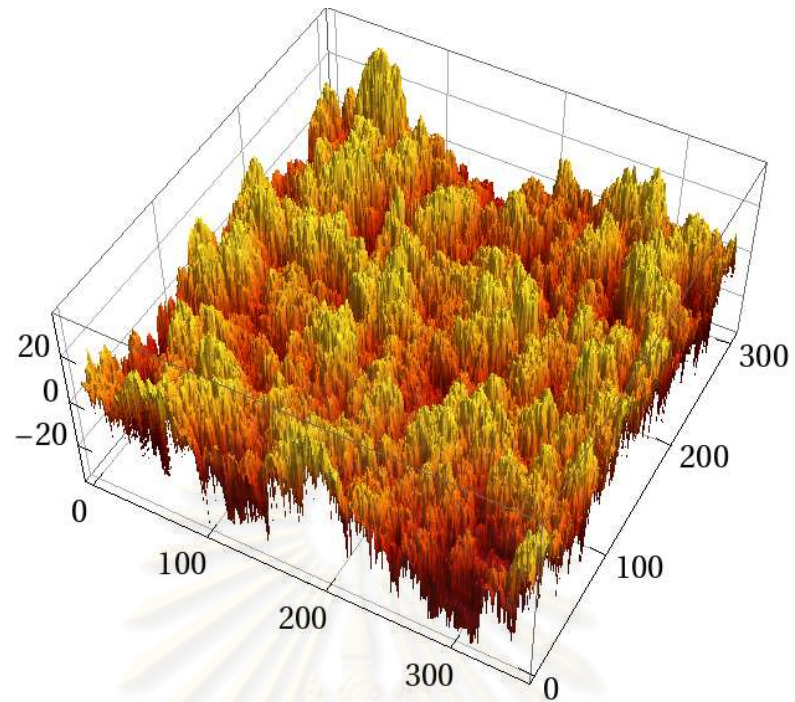


Figure B.14: Surface morphology of the iHCP structure of DT model at $t = 10^5$ UL.

ศูนย์วิทยทรัพยากร
จุฬาลงกรณ์มหาวิทยาลัย

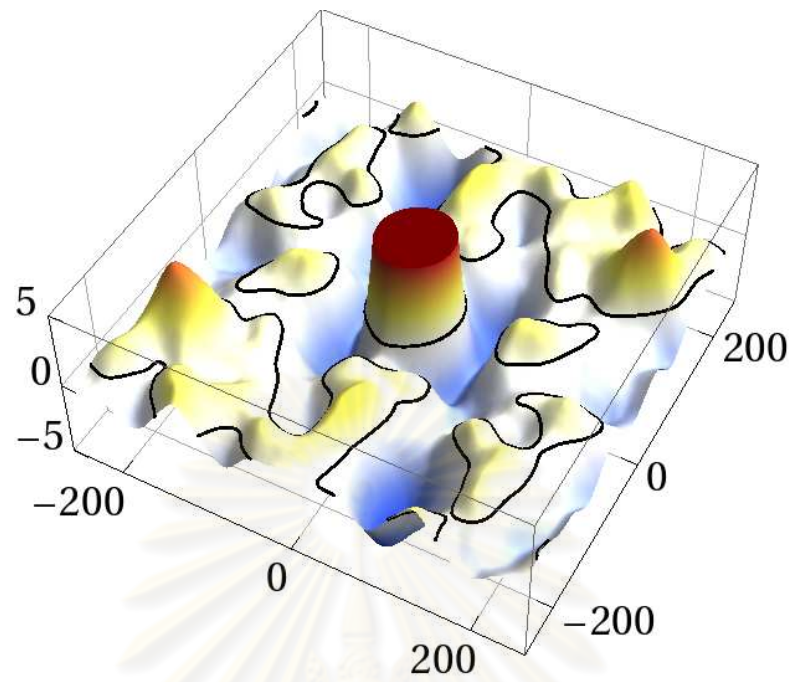


Figure B.15: The correlation function of the SC structure of WV model at $t = 10^5$ UL.

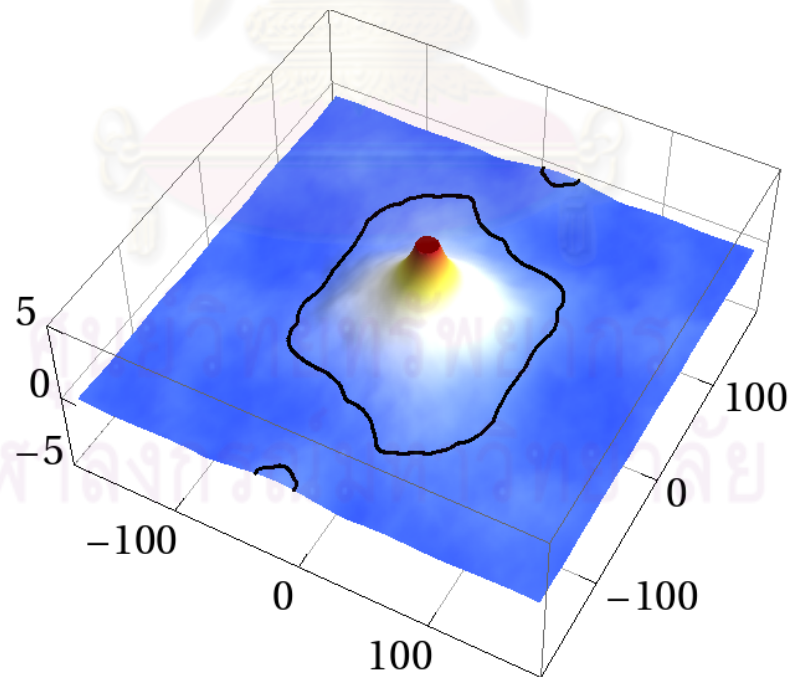


Figure B.16: The correlation function of the BCC structure of WV model at $t = 10^5$ UL.

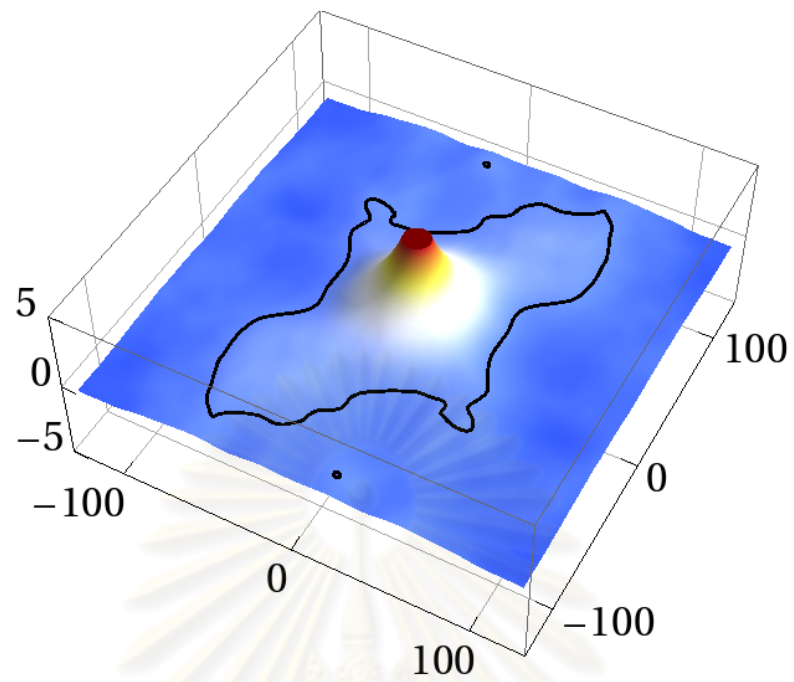


Figure B.17: The correlation function of the FCC(001) structure of WV model at $t = 10^5$ UL.

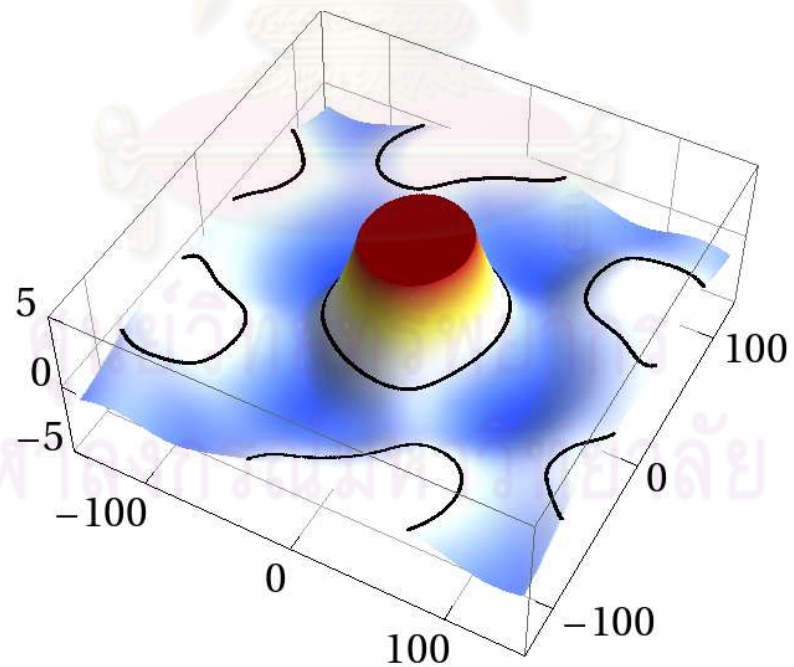


Figure B.18: The correlation function of the FCC(111) structure of WV model at $t = 10^5$ UL.

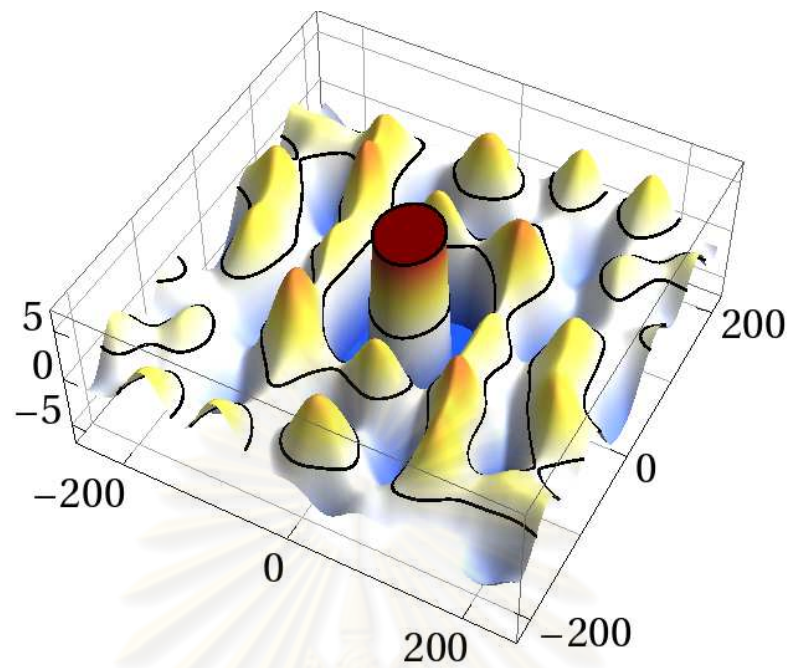


Figure B.19: The correlation function of the SH structure of WV model at $t = 10^5$ UL.

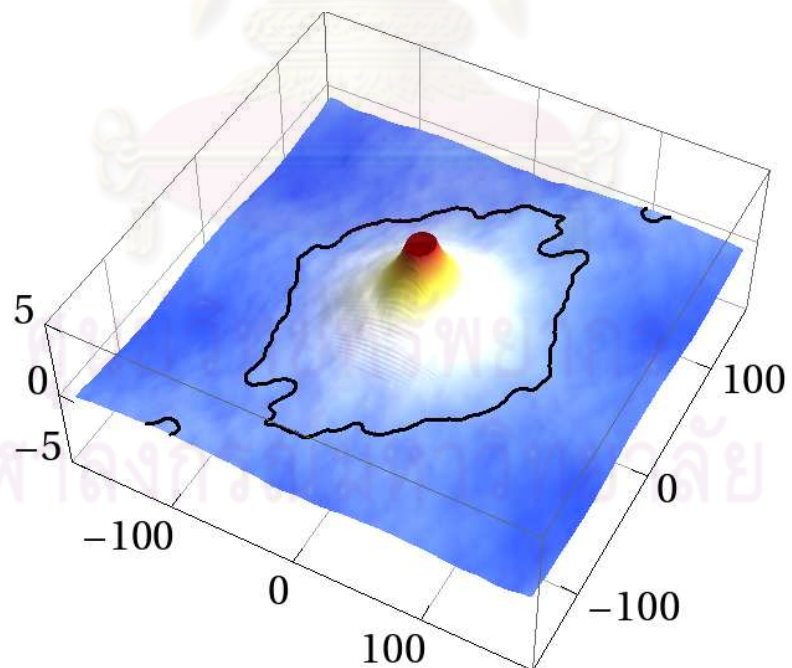


Figure B.20: The correlation function of the HCP structure of WV model at $t = 10^5$ UL.

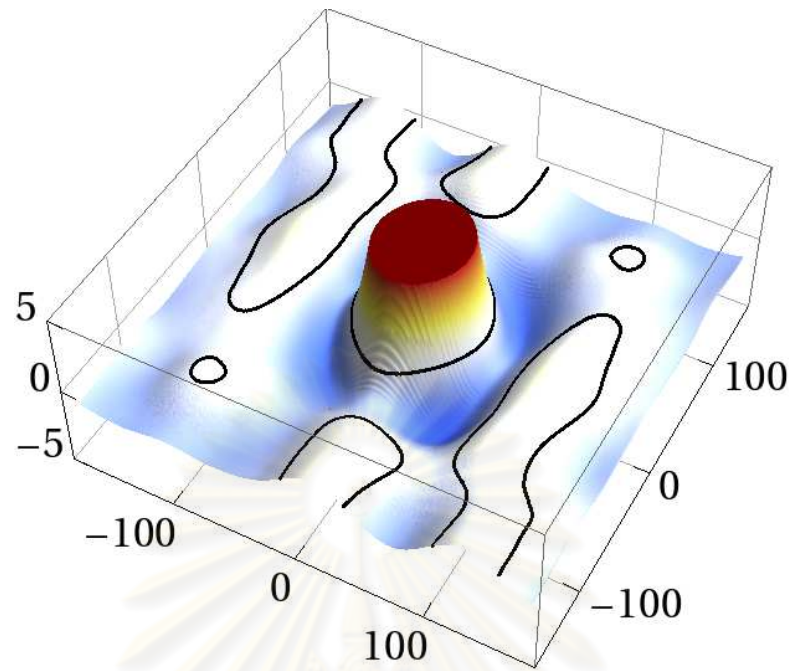


Figure B.21: The correlation function of the iHCP structure of WV model at $t = 10^5$ UL.

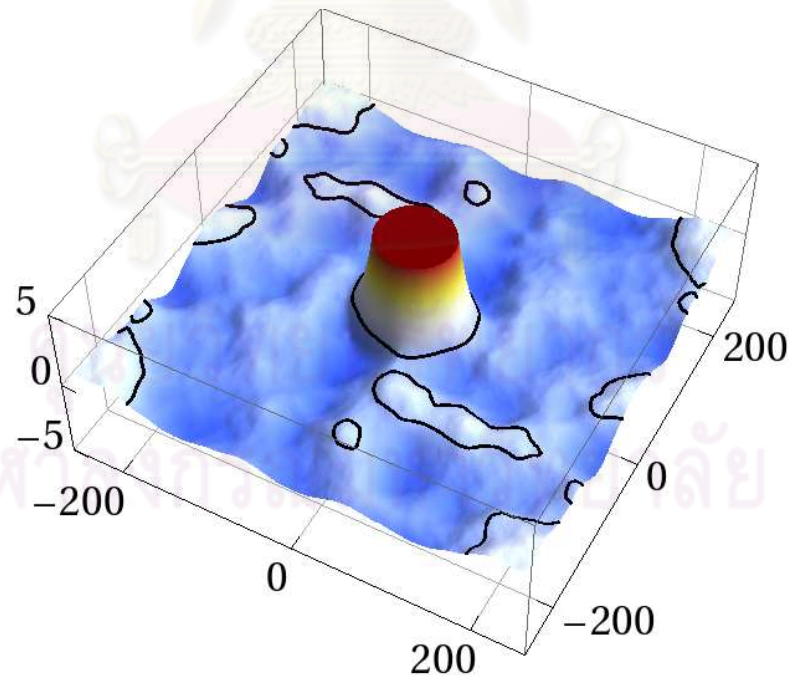


Figure B.22: The correlation function of the SC structure of DT model at $t = 10^5$ UL.

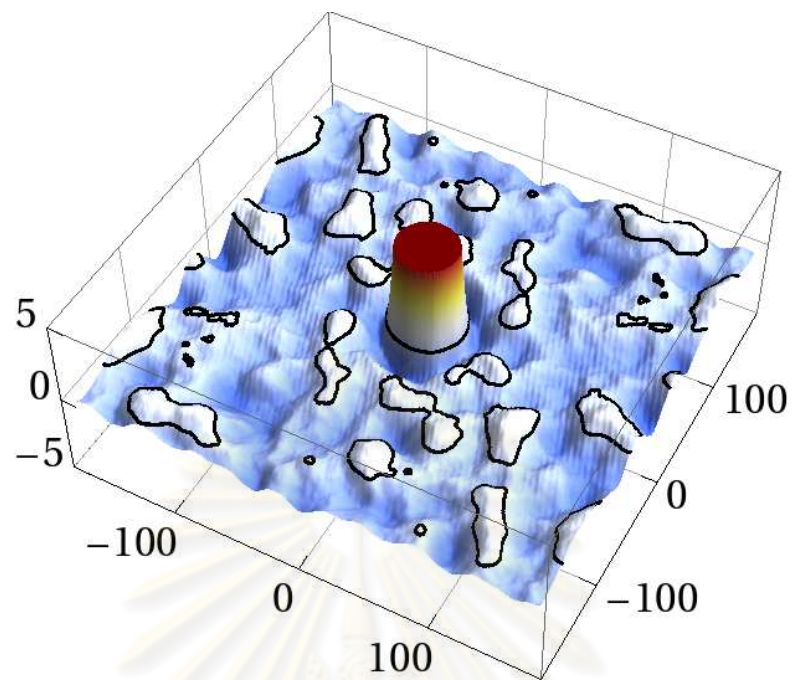


Figure B.23: The correlation function of the BCC structure of DT model at $t = 10^5$ UL.

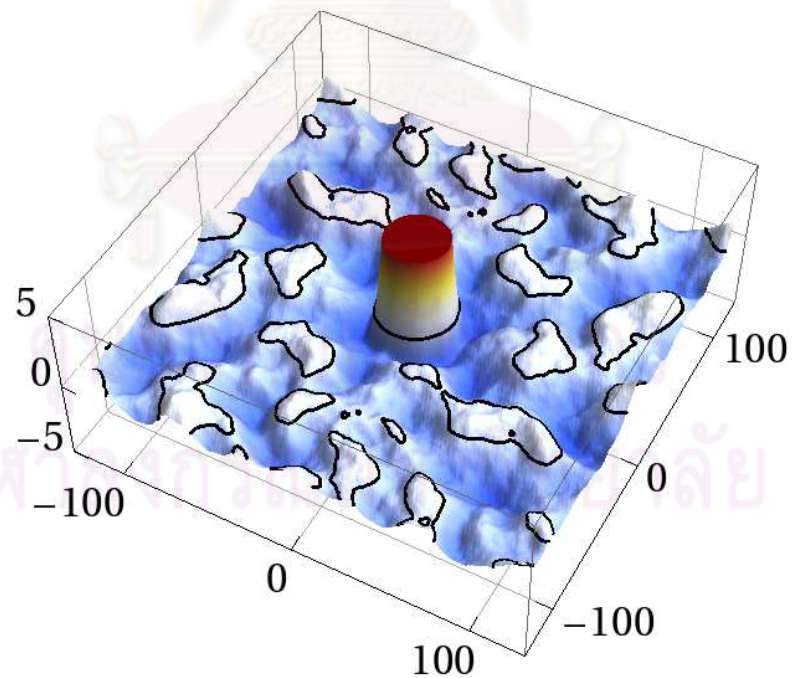


Figure B.24: The correlation function of the FCC(001) structure of DT model at $t = 10^5$ UL.

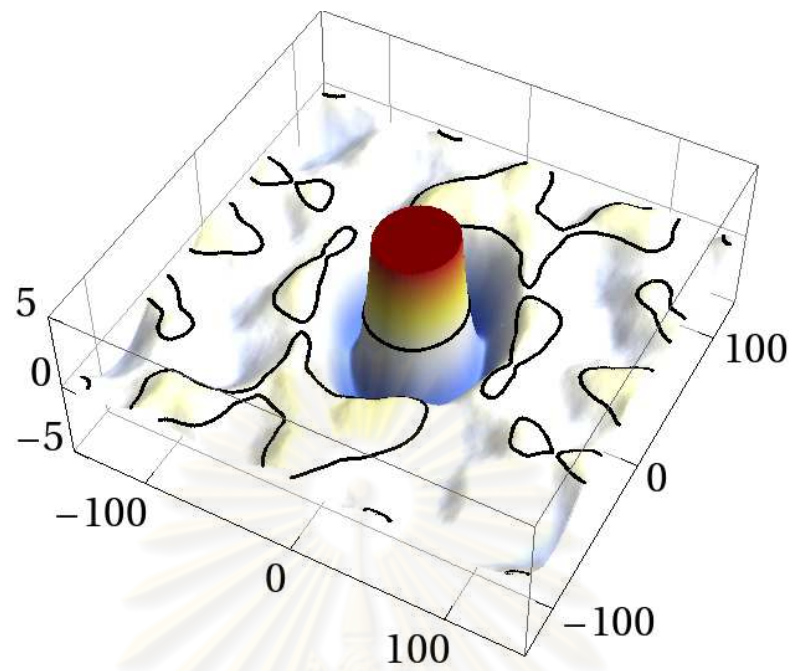


Figure B.25: The correlation function of the FCC(111) structure of DT model at $t = 10^5$ UL.

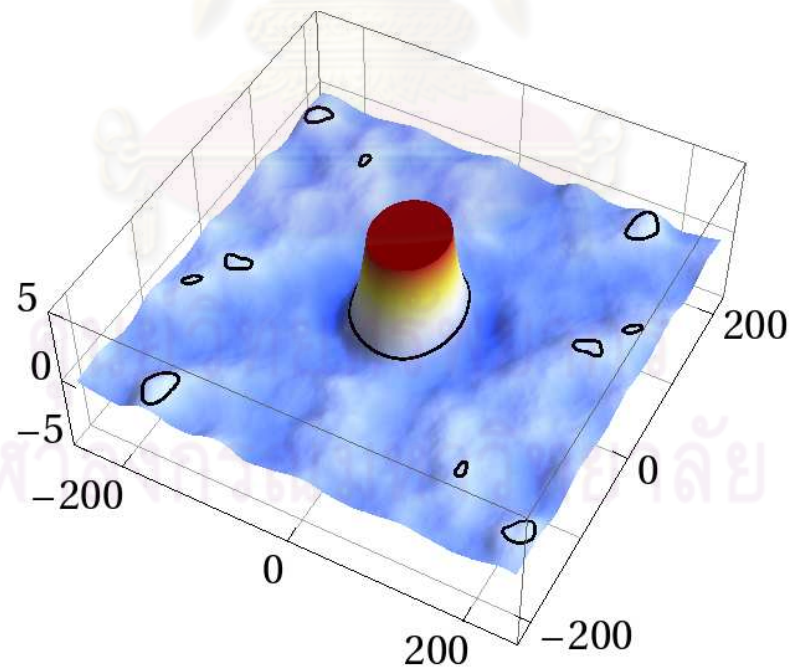


Figure B.26: The correlation function of the SH structure of DT model at $t = 10^5$ UL.

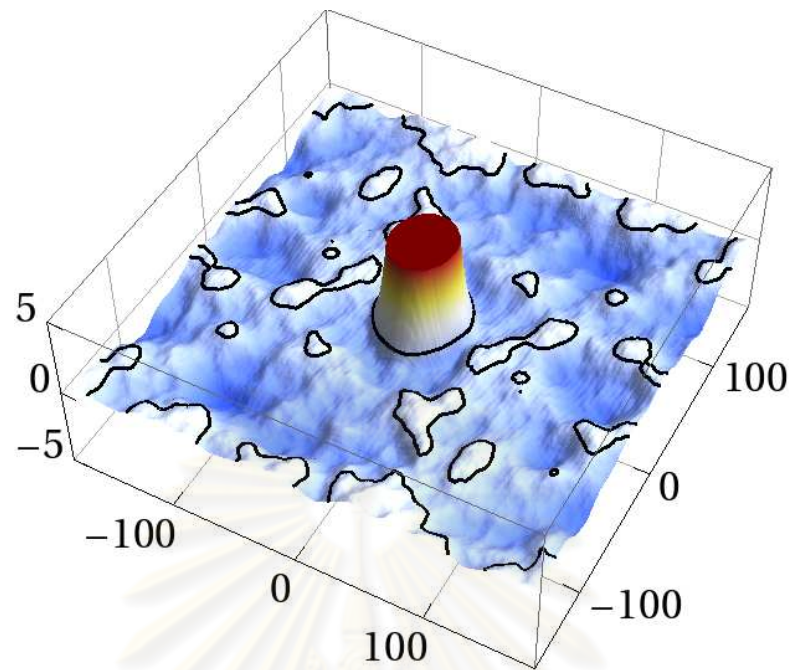


Figure B.27: The correlation function of the HCP structure of DT model at $t = 10^5$ UL.

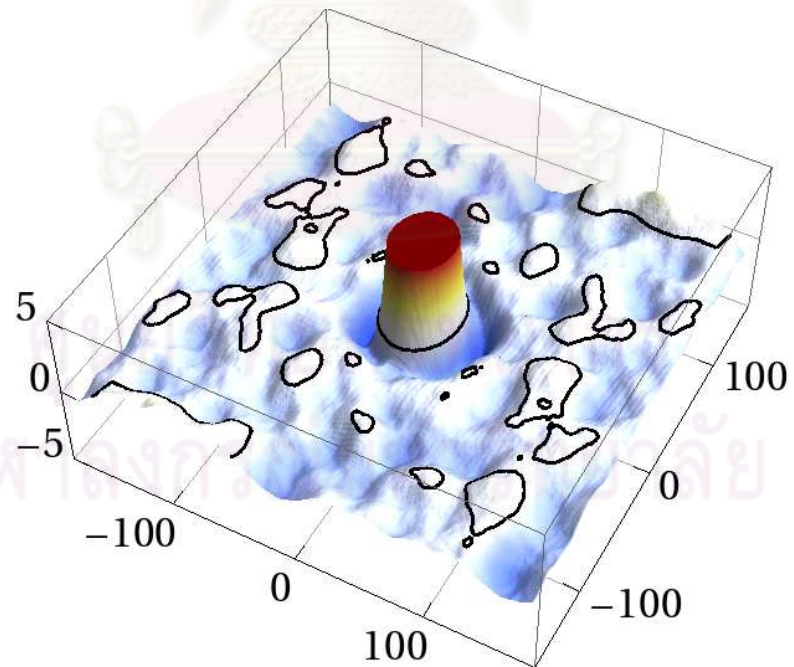


Figure B.28: The correlation function of the iHCP structure of DT model at $t = 10^5$ UL.

Vitae

Mr. Wittawat Kanjanaput was born on the 6th June 1984 in Prachuapkhirikhan, Thailand. He received his Bachelor of Science degree in Physics from Silpakorn University in 2006. During his study, from 2002 to 2009, he was supported by the fund from the Development and Promotion of Science and Technology Talent Project (DPST).

CONFERENCE PRESENTATIONS:

- 2009 W. Kanjanaput, S. Limkumnerd and P. Chatraphorn. Implementation of Crystal Structure into the Das Sarma–Tamborenea Molecular Beam Epitaxy Growth Model. Siam Physics Congress 2009, Petchburi, Thailand (19-21 March; 2009)
- 2010 W. Kanjanaput, S. Limkumnerd and P. Chatraphorn. Implementation of Crystal Structure into the Wolf-Villain Molecular Beam epitaxy Growth Model. Siam Physics Congress 2010, Kanchanaburi, Thailand (25-27 March; 2010)

PUBLICATIONS:

- 2009 W. Kanjanaput, S. Limkumnerd and P. Chatraphorn. Implementation of Crystal Structure into the Das Sarma–Tamborenea Molecular Beam Epitaxy Growth Model. (submitted to Siam Physics Congress 2009)
- 2010 Wittawat Kanjanaput, Surachate Limkumnerd and Patcha Chatraphorn. Growth instability due to lattice-induced topological currents in limited mobility epitaxial growth models. (to be submitted to Physical Review B)